CIRCUMSTELLAR SHELLS OF LATE-TYPE STARS - A STUDY AT MILLIMETER AND INFRARED WAVELENGTHS

Thesis by

Raghvendra Sahai

In Partial Fulfillment of the Requirements
for the Degree of
Doctor of Philososphy

California Institute of Technology
Pasadena, California

1985

(Submitted September 25, 1984)

To Amma and Papa

ACKNOWLEDGMENTS

Now that the moment I have been anticipating with so much pleasure has finally arrived, I don't know where to begin. So many people have helped me during the course of this thesis, in so many different ways; it is impossible to mention all of them here.

I would first like to express my gratitude to the members of my family, who happily made many sacrifices so that I could come to Caltech. Without their love and constant support during my stay here, this thesis would not have been possible.

Peter Wannier introduced me to circumstellar shells; his contagious enthusiasm helped me to weather, with more pleasure than pain, many strenuous nights and days while observing them. I learnt from him the very important lesson that there is always a simple way of looking at nature. I will always be grateful to him for guiding me when I first arrived at Caltech, and subsequently taking on the responsibility of being my advisor for many years. We have done a lot of research together, including the infrared investigation of circumstellar shells, and I hope we will continue to collaborate on future projects.

Nick Scoville, my present advisor, undertook the difficult task of seeing me through the final and most demanding part of my thesis career, and it is hard to thank him enough for this. His constant encouragement and advice, not to mention his meticulous scrutiny of many, many bits and pieces of my thesis has made it possible for me to put them all together into an almost coherent piece of research.

Al Wootten deserves special mention, not only for being instrumental in starting us on the SiS paper, and keeping it going till it was finished, but also for being a very good friend. I have learnt something new and useful every time I have talked to him.

I would like to thank Tom Phillips for allowing me time on the OVRO telescopes even though (I suspect) he didn't quite approve of my attempts to observe many lines in many molecules from many sources, and providing valuable comments on a preliminary draft of the SiS paper. Mark Morris started me on the rough road to understanding radiative transfer, by lending me his program, and was very generous in answering all my queries about this subject.

I want to thank Steve Ridgway for encouraging me wholeheartedly when I first started thinking about the infrared project. Ken Hinkle's fine help during the FTS observations did much towards ensuring the success of this project. Tom Geballe and I tried to detect infrared emission from circumstellar shells in the 2 micron CO lines, and though we didn't succeed, I remember with pleasure our observing runs on the Mount Wilson 100". A few short, but invaluable discussions with Peter Goldreich proved to be of great help in the formulation of the infrared model described in Chapter 6. Saleh Tanveer graciously provided much needed mathematical expertise on numerous occasions.

I have enjoyed working with Mark Claussen on several projects, and am looking forward to observing with him on the FCRAO dish sometime. I would like to thank Steve Lichten and Russell Redman, my most frequent comrades at OVRO, for their help and company during observing. I value my association with many other (past and present) members of the Caltech millimeter group, including Colin Masson, Steve Scott, Ed Sutton, Al Moffet, Anneila Sargent, Jill Knapp, Jocelyn Keene, Fred Lo, Bob Leighton and Dave Woody. I am also in debt to the OVRO staff for the help they so willingly provided whenever I needed it.

Thanks are also due to -- Keith Horne for lending me some of his programs, Rick Edelson, who rescued me from being stranded on the highway while returning from OVRO, the 'Great Zar' who ungrudgingly answered many of my FORTRAN questions, Pawan Kumar, Dave Hough, Alex Fillipenko, Matt Malkan, John Biretta, Tom Lockhart, Roger Linfield, Abhijit Saha and other inhabitants of Robinson who made my life there liveable in some way or other. From amongst those who provided friendship, support and a shoulder to lean on occasionally, I would like to mention Sudhir, Vijaya and Tim, Lisa, Protim (Dada), Molly, Aneesh, Jaywant and Ram.

And last, but not least, I would like to say 'danke' to Andi, my wife and comrade in many adventures, for unselfishly giving up many pleasures in order that I could work on my thesis. Even though she feels (and perhaps rightly so) that astronomy is unnecessary in a world where a lot of people go hungry each day of their lives, she gave me love and put together many of the figures in this thesis.

The financial support provided to me at Caltech, in the form of teaching and research assistantships, and fellowships is sincerely appreciated.

ABSTRACT

This thesis describes an investigation of the physical conditions and molecular abundances in mass-loss envelopes around late-type stars based on millimeter and near infrared spectroscopy, concentrating on the high mass loss, carbon-rich star IRC +10216.

The first part of this thesis is a multi-transition study of the rotational spectrum of SiS from the IRC +10216 envelope. The observational results are described in Chapter 2. A general numerical model to calculate the excitation and radiative transfer for rotation and vibration-rotation lines in circumstellar envelopes is developed in Chapter 3.

Applying this model to fit the observed SiS lines from IRC +10216 (Chapter 4), we find that the undissociated abundance [SiS]/[H_2] in the shielded inner regions of the circumstellar shell is ~ 2.4×10^{-7}, roughly a factor of 100 smaller than that predicted previously by chemical models. The SiS density falls steeply with radius, reaching one-half the undissociated abundance at $r = 9 \times 10^{16}$ cms. We show that a) Si, not S depletion is responsible for the low SiS abundance, and b) most of the available Si has probably been used up in forming SiC grains in the cool IRC +10216 atmosphere.

Variations in the 13 μm infrared flux over the 644 day light-cycle of IRC +10216 produce observable changes in some of the SiS lines. Sharp cusps in the J = 5-4 line wings, observed with the Onsala 20 m antenna, are explained in terms of weak maser emission at maximum light. The model predicts a different shape for this line at minimum light, in excellent agreement with a recent Onsala observation. Line coincidences, involving 13 μm transitions of HCN and C_2H_2 (not considered in the model), may be responsible for poor fits to some of the SiS rotational spectrum.

A sensitive search for SiS J = 7-6 and J = 6-5 lines in other carbon-rich, oxygen-rich, and S-type circumstellar shells was also conducted (Chapter 2). Three new SiS sources, CIT 6, CRL 2688 and IRC +20370, all of which are carbon-rich were detected, in agreement with the chemical equilibrium models predicting SiS to be significantly more abundant in a carbon-rich environment than in an oxygen-rich environment.

The second part of the thesis (Chapters 5 and 6) deals with the investigation of physical conditions in the inner (r ~ 2″) envelope of IRC +10216 -- a scale size that has never been observed previously. We have devised a new observational technique, employing an annular aperture (size 2 - 3.45″) to measure extended emission from resonant-scattered photons in the 4.6 μm CO vibration-rotation band from IRC +10216. In addition to the expected emission up to the expansion velocity of the envelope, both CO and ^{13}CO show evidence of high velocity features in

the blue wing of the line, beyond the 15 km s^{-1} expansion velocity (Chapter 5).

In order to derive physical quantities from the many P and R branch lines present in the infrared spectra, we develop an analytical model to calculate the excitation of these lines due to radiative pumping by thermal emission from circumstellar dust (Chapter 6). The lines are optically thick, and trapping of line radiation has been included. The model emission intensity is found to vary in a simple manner with radius, velocity, J value of the lower state, and the kinetic temperature (which we expect characterises the populations of the V = 0 rotational levels). Our model shows the V = 1 rotational level populations to be in equilibrium with the kinetic temperature despite being excited by infrared radiation.

We derive the following results for the IRC +10216 inner envelope:

i) The kinetic temperature at radius r = 2" is ~ 244 K, roughly twice the extrapolation of the Kwan and Hill (1977) thermodynamic model. This measurement forces revision of analyses of infrared absorption lines in which the radial information was derived assuming a temperature profile (known a priori).

ii) The gas density in the inner regions of the envelope is characterised by a minimum mass loss rate of

$$6 \times 10^{-5} \left\{ \frac{3 \times 10^{-4}}{[CO]/[H_2]} \right\} M_{\odot}\ yr^{-1}.$$

TABLE OF CONTENTS

CHAPTER 1

OVERVIEW AND SUMMARY

The understanding of the late stages of stellar evolution underwent a radical change in 1956, when Deutsch first discovered rapid mass loss from late-type giants and supergiants based on the presence of optical absorption lines in the spectrum of α Her, blue-shifted from the stellar velocity. Since then extensive observations in the optical, infrared and millimeter-wave domains have been used to study the expanding circumstellar envelopes around red giant stars. On large scales ($\gtrsim$ few x 10^{16} cm) the envelope is roughly spherical (Wannier et al. 1979), though some departure from spherical symmetry may occur closer to the star, as revealed by infrared interferometry of a few objects (McCarthy and Low 1975, McCarthy et al. 1980).

Though a definitive answer to the question of what physical mechanism drives mass loss is still lacking, it is widely believed that mass loss is initiated when dust grains condense in the cool (1500-2000 K) atmosphere of the late-type giant star. The grains experience significant radiation pressure because of their high opacity and accelerate radially outward, dragging the gas molecules along. The wind reaches a terminal velocity of 10 - 30 km s^{-1} at typically ten stellar radii ($\lesssim 10^{15}$ cm) from the star (Goldreich and Scoville 1976). This wind is rich in molecular species formed in the photosphere and inner envelope. Due to the rapidly falling density and temperature, the outflow remains chemically frozen from a distance of a few stellar radii (~ few x 10^{14}) to approximately 10^{16} cm, beyond which the interstellar ultraviolet radiation starts to significantly photodissociate the molecules. The CO molecule survives farther out than most other molecules due to self-shielding. The dust grains stream out to merge with the interstellar medium without being significantly affected by the ultraviolet.

The best estimates of mass loss rates come from studies of microwave emission lines from circumstellar envelopes, and are typically 10^{-5} $M_{\odot}$ yr^{-1} (Morris 1980, Knapp et al. 1982, Knapp and Morris 1984). Observations of the near infrared continuum (Gehrz and Woolf 1971) and blue shifted optical absorption lines (Bernat 1977, Hagen 1978) yield slightly smaller rates. Over the late lifetime of a star, the mass lost can be a significant fraction of the original stellar mass and it is now recognized that such mass loss can strongly influence the stellar structure and composition. Mass loss from evolved stars is also a major source of processed material in the interstellar medium ($\sim 6 \times 10^{-10}$ $M_{\odot}$ $yr^{-1}pc^{-2}$, Osterbrock 1974), possibly controlling the chemical evolution of the galaxy (Kwok 1980). The view that most interstellar grains originated from stellar mass loss (Woolf 1973) is now gaining increasing acceptance.

Determination of accurate mass-loss rates, crucial to understanding late stellar evolution, has been one of the major objectives of millimeter-wave CO observations in circumstellar shells. The excitation of these lines is usually due to collisions with H_2; hence these data may provide indirect estimates of the gas density and mass-loss rates.

Models of chemistry in the cool stellar atmospheres have been carried out to relate the circumstellar molecular abundances to photospheric elemental abundances. Most of these studies (Tsuji 1973, 1964, McCabe et al. 1979, Lambert and Clegg 1980) assume that the outflow is chemically inactive [i.e., chemical abundances get frozen at a value determined by thermodynamic equilibrium conditions near the stellar photosphere ($r \sim 10^{14}$)], because the steep decline in density and temperature with radius in the envelope makes the time-scale for chemical reactions (mostly neutral-neutral) much longer than the expansion time-scale.

Two studies (see Goldreich and Scoville 1976, Scalo and Slavsky 1980) of non-equilibrium chemistry in oxygen-rich envelopes reveal interesting departures from the 'freeze-out' models. Processes such as photodissociation and reaction with grains (Lafont, Lucas and Omont 1982) can dominate the chemistry of some molecules in the outer envelope. Measurements of molecular abundances via millimeter-wave observations can be used to test these chemical models in several ways - for example, comparison of the observed abundances (relative to H_2) from stars with different photospheric oxygen to carbon ratios. These measurements are also important for determining the chemical mix of heavy elements such as C, N, O, S, Si (and isotopes) being returned to the interstellar medium from late-type stars.

In 1969, Woolf and Ney (1969) discovered a 10 μm emission feature in a number of cool stars, which they attributed to silicate grains. This identification was supported by Gilman's (1969) calculations showing that silicate grains should be the first solid particles to condense in oxygen-rich stars and later studies by Gehrz and Woolf (1971) revealed this feature to be common to many late-type giants and supergiants. For carbon-rich stars, the first condensates should be carbon (graphite) and silicon carbide; Treffers and Cohen (1974) have detected an 11.2 μm feature in several carbon stars, attributable to the silicon carbide. Since the abundances of silicon-bearing molecules are closely linked to the formation of such grains, a determination of these molecular abundances can aid in understanding the formation and composition of dust.

Photodissociation of molecular species by interstellar ultraviolet radiation in the outer regions of the envelope is also sensitive to the optical/UV properties of the dust. This process produces a radial gradient in the abundance in the outer envelope which can be probed by the pure rotational lines. Observations of CN J = 2-1 emission from the IRC +10216 envelope by Wootten et al. (1982) clearly show that the CN is being produced by the photodissociation of HCN; Huggins, Glassgold, and Morris (1984), in a more detailed analysis of the CN lines find that the circumstellar dust extinction in the ultraviolet must be increased a factor of 2 over the 'standard' value, appropriate for interstellar dust/gas and UV/optical opacity ratios.

In this thesis, I present a program of millimeter and near infrared molecular spectroscopy designed to probe the chemical and physical conditions in mass-loss envelopes.

In Chapters 2, 3 and 4, I describe observations and analysis of SiS millimeter lines from circumstellar shells. Nine SiS transitions from J = 1-0 to J = 16-15 in the carbon-rich shell of IRC +10216 have been observed and used to derive the $[SiS]/[H_2]$ ratio and its dependence on radius. Analysis of the line profiles requires a model of radiative transfer and excitation of the rotational levels in the envelope. I have developed such a model in Chapter 3 with several features refined over existing models in the literature. A preliminary version of this model was used in the CN study by Wootten et al. (1982) to demonstrate that infrared excitation of the CN molecule could not produce the observed extended emission, if its radial abundance was assumed to be constant. The large number of lines from the SiS molecule has provided a sensitive test of this model.

The low abundance for SiS in IRC +10216 suggests that most of the Si has been used up in forming grains, and its radial dependence indicates that SiS either has a very large rate for photodissociation, or is depleted by another process such as adsorption on grains. We also require the circumstellar dust-shielding to be larger than the 'standard' value, which is in accord with the CN study mentioned earlier.

We have also made a survey of SiS in a sample of stars containing all three abundance types: carbon-rich ($C/O > 1$), oxygen-rich ($C/O < 1$), and S type ($C/O \sim 1$) stars (Chapter 2). The results of the survey, presented in Chapter 4, confirm the expectation of chemical models that SiS should be much more abundant in carbon-rich atmospheres than oxygen-rich and S type atmospheres.

The millimeter-wave observations described above do not reveal details about the mass-loss mechanism because most of the interesting phenomena occur too close to the central star. To probe this region, near infrared spectroscopy in molecular vibration-rotation bands holds the best promise. Several such investigations (Keady, Hall, and Ridgway 1984, Hinkle 1978, Hinkle and Barnes 1979, Bernat 1981) have revealed a complex velocity structure suggesting non-uniform outflow. However, in order to determine the radius where the different velocity features are formed, one requires a radial kinetic temperature profile.

There has been no direct way of determining the kinetic temperature in the inner circumstellar shell until now. The only available method has been to model the thermodynamics of the expanding shell. The run of temperature with radius in IRC +10216 as determined from such a model (Kwan and Hill 1977, Kwan and Linke 1982) is reliable only for the outer envelope, where the bulk of the observed millimeter CO line emission, used to constrain the model, is produced. Thus the temperature profile determined from such a model would have to be extrapolated to the inner regions of the envelope, where the vibration-rotation lines are formed.

We use a new observational technique, employing a series of annular apertures, to measure CO vibration-rotation line emission at 4.6 μm, in order to examine the envelope structure at distances corresponding to a few arc-seconds. Our investigation probes a hitherto unobserved region of the envelope, which, at present, is not amenable to other techniques. This is because i) infrared absorption line studies, due to the r^{-1} dependence of radial column density, are most sensitive to material typically a few-tenths of an arcsecond away from the center; ii) the best resolution available from millimeter-wave interferometers is not expected to significantly exceed 5″.

The observations of emission lines through an annulus of inner and outer radii of 2″ and 3.45″ centered on IRC +10216 are presented in Chapter 5. An analytical model has been developed to compute the shapes and intensities of the observed lines (Chapter 6). The relative intensities of the many P and R branch lines are fitted with this model in order to determine the gas temperature and density a few arc-seconds away from the star.

Taking an $r^{-0.7}$ variation with radius (Kwok 1980), we find a kinetic temperature of 244 K at 2″ in the IRC +10216 envelope which is significantly larger than the extrapolation (~ 125 K) of the model of Kwan and Linke (1982). We set a firm lower limit of 6×10^{-5} $M_\odot$ yr^{-1} on the mass loss rate (for an adopted $[CO]/[H_2]$

abundance ratio of 3×10^{-4}).

CHAPTER 2

OBSERVATIONS OF ROTATIONAL SIS LINES - THE CHEMISTRY OF THE OUTER ENVELOPE

Note: - - Chapter 2 is included in a paper entitled 'SiS in Circumstellar Shells' (Sahai, R., Wootten, A., and Clegg, R. E. S. 1984, The Astrophysical Journal, Vol. 284).

2.1. INTRODUCTION

Chemical equilibrium calculations predict that in oxygen-rich stellar photospheres Si atoms are bound in SiO (Tsuji 1973), whereas in carbon-rich photospheres (e.g. Lambert and Clegg 1980) SiS may be fully associated so that much of the Si and most of the sulfur is in SiS molecules. The next most abundant sulfur-bearing species, CS, should be about a factor of 100 less in abundance than SiS (Lafont, Lucas, and Omont 1982). The high mass loss rates determined for a number of carbon stars from their carbon monoxide emission (Knapp et al. 1982) suggest that SiS should be easily detectable.

The J = 6-5 and J = 5-4 lines of the SiS molecule were first detected in IRC +10216 by Morris et al. (1975). The J = 2-1 and J = 1-0 lines were subsequently detected by Grasshoff, Tiemann and Henkel (1981). Henkel, Matthews and Morris (1983, hereafter HMM) identified the J = 1-0 line as the first case of maser emission occurring in a carbon star. A survey of other sources in the J = 6-5 line by Dickinson and Rodriguez-Kuiper (1981) produced weak detections in star-forming clouds. In these studies upper limits have been reported for several O-rich and a few C-rich circumstellar envelopes.

The intensities of the lines in IRC +10216 and the low rotational constant (9 GHz) of SiS allow us to observe emission in the rotational ladder to relatively high J values and thus rigorously test theories of molecular excitation in circumstellar shells (Morris 1975). In particular, a significant population in the very high rotational levels cannot be sustained without infrared excitation. In this chapter we present a survey of SiS line profiles for nine transitions from J = 1-0 up to J = 16-15 in the molecular shell of IRC +10216.

Since the abundance of SiS is closely tied to that of Si, which is very likely to be an important constituent of grains, measurements of the SiS abundance also provide an estimate for the fraction of Si removed from the gas by grains. The low SiS abundance observed in IRC +10216 suggests grain removal of Si has in fact been substantial. Olofsson et al. (1982) note that the velocity extent of SiS and SiO emission in IRC +10216 is smaller than that of other molecules and suggest that this may be understood if the lines arise from the region of grain removal which occurs before the flow has become fully accelerated. Though this is unlikely because it requires grains to be accelerated at large radii in the envelope, if it is correct, SiS emission is expected to provide a sensitive and specific probe of chemistry in the inner circumstellar shell. Non-equilibrium kinetic calculations (Scalo and Slavsky 1980) suggest that SiS can be formed in the outer regions of oxygen-rich circumstellar shells. For these reasons we have made a sensitive survey of both oxygen-rich and carbon-rich circumstellar shells at the frequencies of the J = 7-6 and J = 6-5 lines, and we report several new sources of emission.

2.2. OBSERVATIONS

Observations of the J = 7-6 line of SiS (127.07611 GHz) were obtained with the Number Two 10.4m telescope of the Owens Valley Radio Observatory (OVRO) at Big Pine, California, during 1981 January 18-21. The half-power beamwidth of 0'.8 was measured by scanning across 3C 84 and 3C 273. An acousto-optical spectrometer (Masson 1980) provided 512 channels at 200 kHz (0.47 km s^{-1}) resolution. The observations were obtained with a cooled Superconductor-Insulator-Superconductor (SIS) receiver (Phillips et al. 1981) yielding a measured single sideband system temperature of 350 K.

The telescope was operated position switching between the on-source position and a reference position 5 - 10 arc-minutes away. Calibration of the data was accomplished by observation of hot and cold loads and a noise tube. The atmospheric opacity was frequently monitored; flux calibration was checked by measurements of Jupiter, 3C 84, 3C 273 and 1413+135. The beam efficiency of the 10.4 m telescope is taken to be $\eta_{fss} = 0.75$ for extended sources, based on measurements of the Moon. For sources the size of Jupiter and IRC +10216, $\eta_c\eta_{fss} = 0.60$, where η_{fss} and $\eta_c\eta_{fss}$ are defined by Kutner and Ulich (1981). The observed antenna temperature, in addition to being corrected for rearward beam spillover, is divided by $\eta_c\eta_{fss}$ in order to account for the power in the forward beam not falling inside the main lobe of the beam diffraction pattern.

The J = 6-5 (108.92426 GHz) line was observed at OVRO at two epochs - 1982 January 23-29 and 1983 June 19-20. The earlier observations were obtained with the same equipment as used for the J = 7-6 line. For the later observations, a refrigerated version of the SIS receiver was used, together with an acousto-optical spectrometer which has 512 channels of 1.03 MHz (2.8 km s^{-1}) resolution. Single sideband receiver temperatures were about 450 K. For the January observations, the zenith optical depth was 0.13, and the small-source beam efficiency 0.50. For the June observations, these numbers were 0.19 and 0.65. The improvement in the beam efficiency was due to a change in the optics. The frequency range of the 500 MHz spectrometer also included the C_3N J = 12-11 doublet(108.84, 108.86 GHz) and the HC_3N J = 12-11 line at 109.17397 GHz. These lines are not discussed further here.

The J = 5-4 (99.77155 GHz) line was observed on 1983 December 4, with the 14 m telescope of the Five College Radio Astronomy Observatory (FCRAO), Amherst, Massachusetts. The half-power beamwidth at 89.6 GHz was 59". The aperture efficiency of the telescope at this frequency was 0.54, the beam efficiency measured on the moon (η_{fss}) was 0.70, and the beam efficiency for sources the size of Jupiter, $\eta_c\eta_{fss}$, was measured to be 0.64. The single sideband system temperature was approximately 370 K during the observations.

Several higher rotational transitions of SiS were observed with the 4.9 m telescope of the Millimeter Wave Observatory (MWO), Fort Davis, Texas, during early 1982, when IRC +10216 was at maximum light, and in 1983 April. The J = 16-15 line (290.380320 GHz), J = 15-14 line (272.242442 GHz), J = 14-13 line (254.102716 GHz) J = 13-12 line (235.960972 GHz), and J = 12-11 line (217.817347 GHz) were observed with a cooled version of the receiver described by Erickson (1981) in conjunction with a bank of 256 1 MHz filters. The measured single sideband system temperature varied from 1600 K at the lowest frequency to 3500 K at the highest frequency. The data were obtained in a position switched mode in which reference positions were azimuthally displaced by 5′. The atmospheric opacity was estimated from measurement of the sky emission (a typical optical depth was 0.3). Calibration was done by synchronous detection of an absorber at ambient temperature. The main beam efficiency for sources the size of Jupiter, and appropriate for IRC +10216, ranges from $\eta_c \eta_{fss} = 0.56$ at 211 GHz to 0.40 at 270 GHz. The half-power beamwidth decreases from 1′.3 at the lower end of the frequency range to 1′.1 at the upper end.

2.3. RESULTS

The observational results for the several transitions we have observed in IRC +10216 are presented in Table 2.1, along with parameters of other transitions observed at other observatories. All intensities are given as corrected antenna temperature T_R (Kutner and Ulich 1981) corrected for atmospheric absorption and assuming the source has a size comparable to that of Jupiter.

The line widths are all consistent with a uniform expansion velocity of $V = 14 \pm 1$ km s^{-1}, agreeing with the measurement of 14.1 ± 0.3 km s^{-1} reported by Olofsson et al. (1982). In Chapter 4 we show that the line profiles are sensitive to the infrared flux at the frequency of the SiS vibration-rotation lines. For that reason we have also listed in Table 2.1 approximate phases computed from the IRC +10216 light curve illustrated by Witteborn et al. (1980).

The results of our survey in other carbon-rich and oxygen-rich stars are listed in Table 2.2a for the $J = 7-6$ line, and in Table 2.2b for the $J = 6-5$ line. Column (1) gives the source name, followed in columns (2) and (3) by the coordinates of the location we observed. In column (4) is the local standard of rest (LSR) velocity of the source, normally that determined from observations of other molecules in it. Column (5) gives the corrected antenna temperature, T_R. For most sources, only upper limits were obtained; the 3 σ limits are given in parentheses.

The observed line profiles for IRC +10216 are shown in Figures 2.1a and 2.1b. In Figure 2.2 we show the J = 6-5 line profiles observed for the other detected sources in our survey.

2.4. DISCUSSION

With the exception of the masing J = 1-0 line, the line shapes in Figure 2.1a are all rounded and show no double cusps at the extreme velocities of the profiles. However, the J = 5-4 line profile obtained with the 1′ beam of the 14 m FCRAO telescope, shown separately in Figure 2.1b, has sharp cusps in the line wings. Using a slightly smaller (0′.73) beam, Olofsson et al. (1982) observed the J = 5-4 transition to be even more sharply cusped, which they interpreted as signifying partial resolution of an optically thin source. On the other hand, Grasshoff, Tiemann and Henkel (1981) reported a profile of the J = 2-1 line obtained with a 0′.45 beam that was flat-topped, and Johansson et al. (1983) reported profiles of the J = 4-3 line observed at Onsala which were also flat-topped. As the source size is expected to become larger in the lower transitions, one would naively expect the lines below the 5-4 transition to be even more concave, since the emission region should be more resolved. A reconciliation of all line profiles with a simple model for the SiS emission from IRC +10216, such as the one described by Olofsson et al. (1982), is therefore difficult to achieve.

Olofsson et al. (1982) remark upon several peculiar features of their SiS observations. The measured extent of the SiS envelope (0'.38) and velocity extent of the line profile are both among the smallest of the molecules they observed. To explain the observed size of the emission region and the shape of the line profile, they were forced to assume a very high excitation temperature for the line and a very low optical depth. They speculated that certain assumptions of their model, such as the form of the density law, may be invalid or that maser amplification of the line might occur.

Given the significant profile differences between the various transitions observed by us and others, the sensitivity of SiS excitation to infrared excitation (Morris et al. 1975; Morris 1975), and also spurred by detection of maser emission in the J = 1-0 line by HMM, we have modeled all observed SiS line profiles in IRC +10216 using a modification of the numerical scheme described by Morris and Alcock (1977) and Morris (1980). The formal model is presented in the next chapter (Chapter 3), and its application to our observations of IRC +10216 follows in Chapter 4. Detailed models have not been constructed for the survey sources, but we have used models constrained by the available data to estimate the abundance of SiS in their shells.

Table 2.1. The SiS Spectrum of IRC +10216.

Line (1)	Frequency (GHz) (2)	Telescope (3)	Beamwidth (Arcmin) (4)	Efficiency $\eta_c\eta_{fss}$ (5)	T_R (K) (6)	Phase (7)	a
1-0	18.15	OVRO	1.6		0.27(.007)	0.2	b
2-1	36.31	MPI	0.45		0.7	0.4	c
5-4	90.77	FCRAO	0.97	0.64	0.90(.026)	0.1	
		OSO	0.70	0.55	1.7	0.0	d
6-5	108.92	OVRO	1.06	0.60	0.76(.06)	0.03	e
				0.63	0.75(.05)	0.83	f
7-6	127.08	OVRO	0.78	0.60	0.80(.04)	0.45	
12-11	217.82	MWO	1.3	0.56	0.66(.08)	0.12	
13-12	235.96	MWO	1.3	0.50	0.78(.40)	0.13	
14-13	254.10	MWO	1.3	0.45	0.85(.12)	0.72	
15-14	272.24	MWO	1.3	0.40	1.20(.17)	0.72	
16-15	290.38	MWO	1.2	0.40	0.55(.10)	0.04	

Note. Error limits are 1 σ

a. Assuming a period of 644 days and epoch 1982 January 2.

b. From Sahai and Claussen 1984.

c. From Grasshoff, Tiemann and Henkel 1981.

d. From Olofsson et al. (1982).

e. 1982 January observations.

f. 1983 June observations. Refer to Figure 2.2d.

Table 2.2a. SiS J = 7-6 Survey Results.

Object (1)	Coordinates R.A.(1950) (2)	 Decl.(1950) (3)	V_{LSR} (km s^{-1}) (4)	T_R (mK) (5)	
CRL618	$04^h39^m33^s.8$	+36°01'15.	-35.0	(117)	
CRL 865	06 01 17.5	+07 26 03.	43.0	(111)	
IRC+10216	09 45 14.8	+13 30 40.	-26.0	800 (123)	a
CIT 6	10 13 12.0	+30 49 24.	-1.5	(066)	
V Hydra	10 49 11.3	-20 59 05.	2.0	(144)	
RX Boo	14 21 56.7	+25 55 49.	0.0	(066)	
V CrB	15 47 44.1	+39 43 23.	15.0	(096)	
Sgr B2	17 44 10.0	-28 21 16.	52.0	(195)	
Chi Cyg	19 48 38.5	+32 47 12.	10.7	(243)	
CRL 2688	21 00 20.0	+36 29 44.	-34.5	(201)	
NGC 7027	21 05 09.5	+42 02 03.	24.2	(156)	
CRL 3068	23 16 42.4	+16 55 10.	-28.0	(174)	
IRC+40540	23 32 00.4	+43 16 17.	-18.0	(201)	

Note. Limits are 3 σ over a 2 MHz range.

a. Noise is 3 σ over a 0.2 MHz range.

Table 2.2b. SiS J = 6-5 Survey Results.

Object	Coordinates		V_{LSR}	T_R	
	R.A.(1950)	Decl.(1950)	(km s^{-1})	(mK)	
(1)	(2)	(3)	(4)	(5)	
IK Tau	$03^h50^m43^s.7$	$+15^\circ30'34.$	34.0	(084)	
IRC+10216	09 45 52.2	+13 30 40.	-26.0	760 (180)	a
				750 (140)	b
CIT 6	10 13 12.	+30 49 24.	- 1.5	57 (033)	c
Y Cvn	12 42 46.	+45 42 48.	3.4	(141)	
RT Vir	13 00 05.	+05 27 06.	18.4	(147)	
RX Boo	14 21 56.7	+25 55 49.	- 2.0	(087)	
IRC+20370	18 39 41.7	+17 38 16.	2.0	50 (036)	d
IRC+00382	18 47 58.	+04 32 30.	13.0	(264)	
Chi Cyg	19 48 38.5	+32 47 12.	10.7	(180)	
V Cyg	20 39 41.3	+47 57 45.	10.0	(204)	
CRL 2688	21 00 20.0	+36 29 44.	-34.5	70 (060)	d

Note. Limits are 3 σ over a 2 MHz range.

a. Noise is 3 σ over a 0.2 MHz range.

b. 1983 June observations. The noise is over a 2.06 MHz range. The spectrum in Figure 2.2d is with 2.06 MHz filters.

c. The spectrum in Figure 2.2a is with 0.8 MHz filters, Hanning smoothed.

d. The spectrum in Figures 2.2b and 2.2c is with 2.06 MHz filters, Hanning smoothed.

FIGURE CAPTIONS

Figure 2.1a. The SiS spectra of IRC +10216, excluding the J = 5-4 line. See Table 2.1 for a summary of these and other observations of SiS. The J = 1-0 line has been provided by Sahai and Claussen (1984).

Figure 2.1b. The J = 5-4 line of IRC +10216 obtained with the FCRAO 14 m dish.

Figure 2.2. Detections of the J = 6-5 line of SiS in other objects. On the vertical axis is plotted T_R. a). CIT 6 (0.8 MHz filters); b). CRL 2688 and c) IRC +20370 (2.06 MHz filters). Hanning smoothing has been applied to these spectra. The J = 12-11 lines of C_3N are also detected in several of these sources, lying on the right as marked. (d) SiS and C_3N lines in IRC +10216 (2.06 MHz filters).

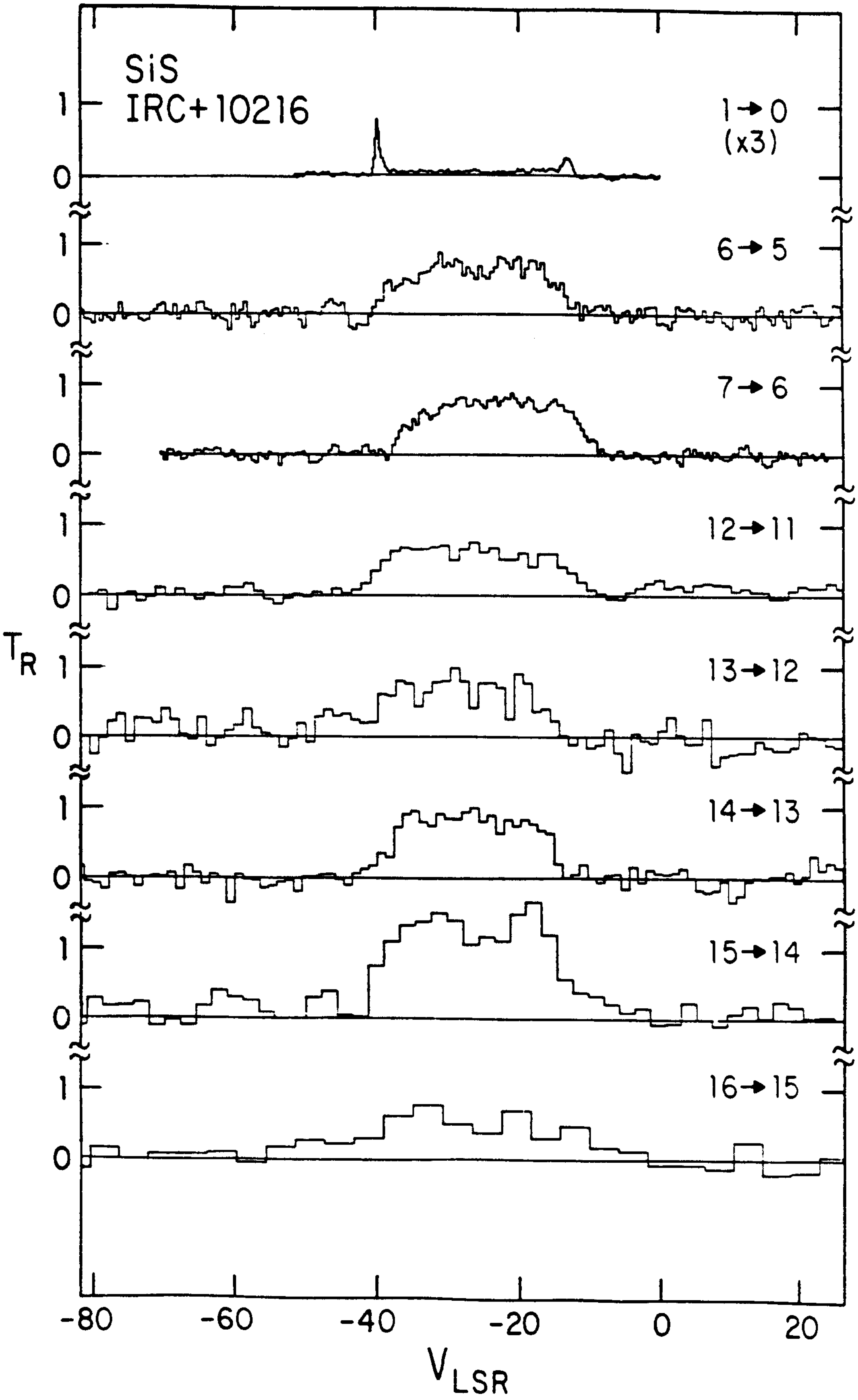
SiS
IRC+10216
1→0
(x3)
6→5
7→6
12→11
13→12
14→13
15→14
16→15
T_R
1
0
-80
-60
-40
-20
0
20
V_LSR

FIGURE 2.1a

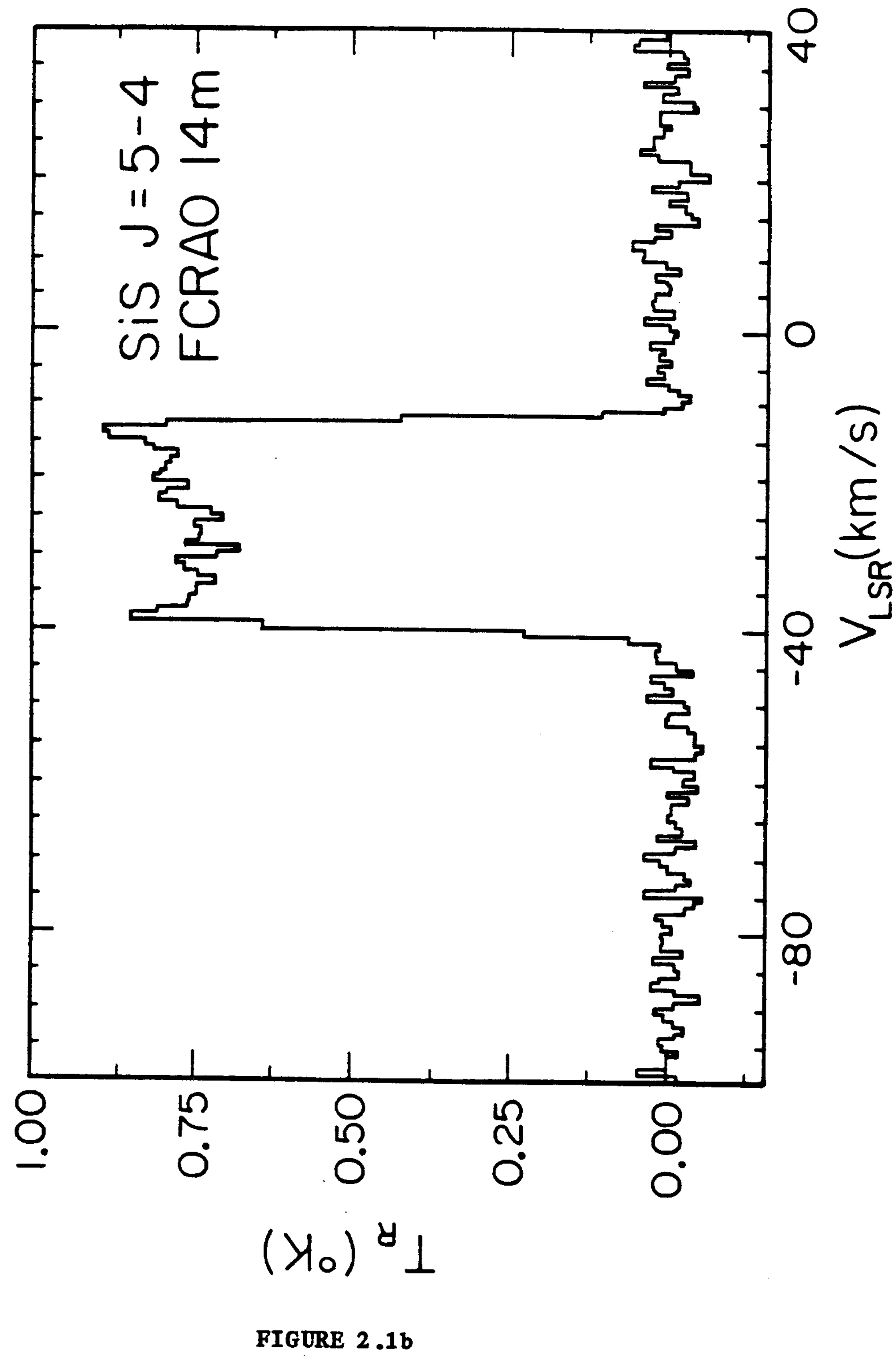

FIGURE 2.1b

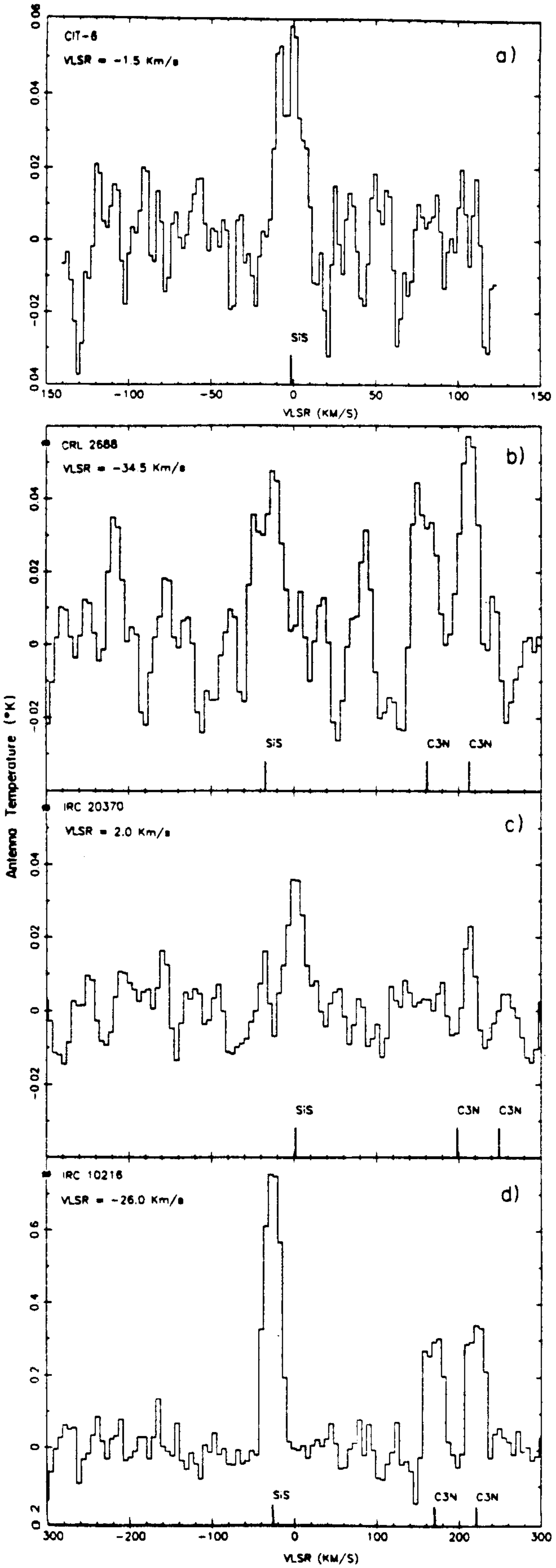
CIT-6
VLSR = -1.5 Km/s
a)
SiS
VLSR (KM/S)
CRL 2688
VLSR = -34.5 Km/s
b)
SiS
C3N
C3N
IRC 20370
VLSR = 2.0 Km/s
c)
SiS
C3N
C3N
IRC 10216
VLSR = -26.0 Km/s
d)
SiS
C3N
C3N
VLSR (KM/S)
Antenna Temperature (°K)
0.06
0.04
0.02
0
-0.02
0.04
150
-100
-50
0
50
100
150
0.6
0.4
0.2
0.2
300
-200
-100
0
100
200
300

FIGURE 2.2

CHAPTER 3

A MODEL FOR INTERPRETING ROTATIONAL LINES FROM CIRCUMSTELLAR ENVELOPES

3.1. INTRODUCTION

In this chapter we describe a simple numerical method for treating the excitation of, and radiative transfer between, the rotation and vibration-rotation levels of molecules in expanding circumstellar envelopes. The model has been used in the following chapter to interpret the SiS rotational lines, whose observations were described in the previous chapter. This work is based on a similar model (hereafter referred to as the MA model) described in Morris (1975), Morris and Alcock(1977), and Morris (1980). The code for the numerical scheme was an extensive modification of that used in the papers mentioned above. For the sake of continuity, we will describe our model completely, with increased emphasis on the sections which represent major improvements and new additions to the MA model.

3.2. THE ENVELOPE MODEL

In order to determine the molecular excitation as a function of radius, the circumstellar envelope is divided into a large number (up to a maximum of 75) of thin spherical shells or zones, with the width, Δr, being smaller for the inner zones as compared to the outer zones. This allows for the more rapid radial variation of physical conditions closer to the star.

We calculate the level populations at any given radius by solving the equations of statistical equilibrium at that point. This requires a knowledge of the mean angle-integrated, velocity-integrated intensity J of the radiation field at the frequencies of the rotation and vibration-rotation lines. We idealize the physical processes and conditions relevant to the molecular excitation in circumstellar shells in the following manner:

1) The circumstellar gas cloud is assumed to be spherically symmetric, and expanding with a constant velocity in all but the innermost regions ($r \lesssim 10^{15}$ cm). For radii smaller than 10^{15} cm the expansion velocity increases with radius in a manner similar to that described by Goldreich and Scoville (1976) in their model of an OH/IR envelope.

2) The mass loss rate from the central star is assumed to be constant; this produces an r^{-2} fall-off of gas density for radii where the expansion velocity has reached its terminal value. The mass-loss rate (dM/dt), velocity V(r), and gas density ρ(r), are related through the equation of continuity

$$dM/dt = 4\pi r^2 \rho(r) V(r) \quad . \tag{3.1}$$

3) The variation of gas temperature with radius is taken from the model by Kwan and Linke (1982) for the molecular envelope of IRC +10216. Since the various heating and cooling mechanisms depend on the mass-loss rate and abundances of the major coolants,

we have included a scale factor in the temperature function.

The temperature and the gas density together determine the collisional excitation of the rotation and vibration-rotation levels through collisions with H_2 molecules (collisons with electrons can be neglected because the gas in the envelope is mostly neutral). Cross sections for transitions through collisions with H_2 for some molecules are available in the literature (e.g., CO -- Green and Thaddeus 1976 and CS -- Green and Chapman 1978) and have been used accordingly. For molecules for which no information is available, the CO cross sections have been used. Since most molecules, except CO, are excited by the infrared field present in the envelope, collisional excitation is unimportant, and the lack of good cross sections is not a serious handicap.

4) The infrared field at λλ 2 - 20 μm, produced by thermal reemission from circumstellar grains is responsible for exciting the millimeter and infrared lines of many molecules via transfer of population from the ground vibrational state (V = 0) to the first excited state (V = 1) and subsequent cascade down to the V = 0 state. As a first approximation, we have simulated this effect by taking the infrared source to be a blackbody, of a temperature determined from the near infrared color, and of an angular size determined by the measured infrared fluxes. The inner radius of the circumstellar shell in our model corresponds to the radius of this blackbody. This assumption is not a good one when the observed lines, e.g., the vibration-rotation lines of CO at 4.6

μm, are produced in the region where the dust and gas are coextensive.

5) The radial variation of abundance of the molecule under consideration is treated as a variable. Photodissociation by the interstellar ultraviolet radiation is probably one of the major physical processes affecting the molecular abundances; therefore we calculate the radial abundance using the photodissociation analysis described by Huggins and Glassgold (1982).

3.3. RADIATIVE TRANSFER AND STATISTICAL EQUILIBRIUM

When lines are optically thick, one must include in the mean intensity J the contribution of transferred line radiation from other parts of the envelope. Sobolev (1958, 1960) showed that, when a large scale velocity gradient is present, this contribution is a function of physical properties only in the neighborhood of the point of interest (hereafter referred to as P) because the line radiation from points farther away is doppler shifted out of the local absorption profile. For a constant expansion velocity, this is true for rays in tangential directions (perpendicular to the shell radius), but along radial directions, there is no gradient. Therefore, the Sobolev approximation cannot be used to calculate the contribution to the mean intensity from transferred radiation along radial and near radial directions.

a) Zone of Radiative Contact

Morris and Alcock (1977) first realized that the zone of radiative contact of a molecule at any radial point was still limited to a narrow radial geometrical region. Their calculation of the geometry of the radiative contact zone was based on the assumption that two molecules are in radiative contact if their relative velocity is smaller than the local linewidth. However, it is actually the relative velocity, projected onto the line of sight joining the two molecules, that determines the zone of radiative contact.

The geometrical shape of the radiative contact zones in the MA model is conical with the opening angle equal to $\sin^{-1}(\Delta V/V)$, and is quite different from the one calculated in our model, as displayed in Figure 3.1. In this figure the area from the X-axis to any of the curves represents the region of contact for a molecule placed at a radial distance of 0.3 units on the X axis. The X and Y axis originate at the center of the envelope, and rotating the boundaries of the contact zones around the X-axis generates the three-dimensional shape of the radiative contact volume. The shape of the radiative contact zone is a function of velocity offset (as a fraction of the expansion velocity V) from line-center; therefore we have displayed the shape at two offset velocities, $\Delta V/V = 0.05$ and 0.017.

b) The Mean Intensity J

The calculation of J requires an integration over the intrinsic line profile, assumed to be rectangular of width ΔV (Morris 1975, Morris and Alcock 1977). We take ΔV to be constant with radius for each particular model.

To determine J we sum various contributions to the mean intensity. In Figure 3.2 we show the division of the envelope into different spatial regions (described in the following text) for calculating J. The boundary of the radiative contact zone is shown for a $\Delta V/V = 0.05$. The elliptical curves in the figure represent the boundaries of the spherical thin shells into which the envelope is divided.

i) Non-local Contribution

The first contribution comes from line radiation produced in the radiative contact zone internal and external to P. The contribution to the mean intensity from each thin shell, is given by

$$\delta J = B(T_{ex}) \{1-\exp(-\Delta\tau_z)\} \exp(-\Delta\tau) \Delta\Omega/4\pi \qquad (3.2)$$

where $B(T_{ex})$ is the Planck function at T_{ex}, the excitation temperature in the thin shell, $\Delta\tau_z$ is the optical depth correponding to the shell-width, $\Delta\tau$ is the optical depth due to material between thin shell and P, and $\Delta\Omega$ is the solid angle subtended by the thin shell at P. In replacing the integration over solid angle by a simple multiplication by $\Delta\Omega$ we assume that the excitation temperature and optical depth terms do not change significantly over the range of integration. Since the geometry of the radiative contact zone is a function of velocity offset from line-center, $\Delta\Omega$ changes with velocity. To account for this, we calculate $\Delta\Omega$ at a number of velocity points within the intrinsic line width and find a mean value, which is used in Eqn. 3.2. For the assumed rectangular profile, all velocities are weighted equally. The sum of δJ's from all thin shells internal and external to P then gives the first contribution.

ii) Local Contribution

For the second contribution, which comes from the thin shell containing P ('Local Zone' in Figure 3.2), the 4π solid angle at P is divided into three regions. The first covers the angle from the radial direction towards the star to the crossing point (C_1) between the radiative zone boundary and the inner side of the thin shell. A second region covers a similar angle from the radial direction away from the star to the crossing point (C_2) with the outer side of the thin shell, and a third region covers the remaining angular region (Sobolev Region). In the last region, hereafter referred to as the Sobolev region, since it includes tangential directions along which the velocity gradient is large, the Sobolev approximation should be valid. The contribution to the mean intensity from this region, calculated using the escape probability given by Castor (1970), suitably modified to restrict the range of integration over angle ($\angle C_1PC_2$), is given by

$$\Delta J = S\ (1-\beta_S) \qquad (3.4)$$

where S is the source function, $\beta_S = \int d\mu\ \beta_\mu$, and β_μ is the escape probability per unit solid angle. The latter quantity is defined by

$$\beta_\mu = [1 + \exp\{-\tau(r,\mu)\}]/\tau(r,\mu) \qquad (3.5)$$

where $\tau(r,\mu) = \tau^0_{ij}\ /\ (1 + \mu^2\sigma)$ is the optical depth in the direction at an angle $\phi = \cos^{-1}\mu$ with the radius vector, and $\sigma = \left[d(\ln V)/d(\ln r) - 1\right]$, where V is the radial expansion velocity. The tangential optical depth $\tau^0_{ij} = (hcr/4\pi V)B\ g_i(n_j-n_i)$, with n_j and n_i being the sublevel molecular densities in the j and i levels, where B is the Einstein absorption coefficient.

The contributions from the other regions are calculated by integration of the escape probability over solid angle and velocity:

$$\Delta J = S(1-\beta_M) \qquad (3.6)$$

where

$$\beta_M = \int d\Omega/4\pi \int d\tau \int dV/\Delta V\ \exp(-\tau_v)\ . \qquad (3.7)$$

The rays along which the optical depth is evaluated are restricted to extend from P to the boundary of the thin shell, because the transferred line radiation from gas outside the thin shell has been accounted for in the previously considered contribution from the internal and external zones. This is equivalent to saying that a photon generated at point P, is considered to have escaped from the local region if it crosses over the zone boundary into an external or internal zone.

iii) 3 K Background Contribution

The third (and last for the rotational lines) contribution comes from the cosmic 3 K background. The 4π solid angle at point P is again divided into the three angular regions described above, and the contribution from the 3 K continuum is calculated for each region by replacing the line source function S with the Planck function at 3 K in equations 3.4 and 3.6. However, the rays along which the optical depth is calculated (Eqn. 3.7) extend from point P to the outer boundary of the circumstellar shell.

iv) Central Infrared Source Contribution

For the vibration-rotation lines, an additional contribution is the thermal emission from heated dust comprising the central infrared source. A simple but approximate way of calculating this is to ignore the radial structure of the infrared source and to assume that the continuum is produced by a central blackbody. Since the absorption due to molecules between the infrared source and P has to be taken into account when evaluating the mean continuum intensity, the assumption of a single, central source is good only if the radial optical depth in the vibration-rotation lines is small. In such a case, the excitation in the outer regions of the shell is not severely affected by the model assumptions in the inner regions. Such is probably the case for molecules like SiS and SiO. However, for a more abundant molecule like CO the opacity in the vibration-rotation lines is extremely large in the inner regions. There, the continuum producing region is coextensive with the gas, and the assumption of a central blackbody source is invalid. In this case a more sophisticated calculation of the mean infrared intensity is required. We describe the details of such a calculation in Chapter 6.

Starting with a trial set of level populations in each thin shell, the mean intensity J is determined in each shell, for all the rotation and rotation-vibration lines, by summing the contributions described above. The statistical equilibrium equations are then solved in each shell, generating a new set of level populations for the next iteration. This cycle is continued till the level populations in each shell, from successive iterations, differ by less than a specified amount.

3.4. MODEL LINE PROFILES

In order to determine the model velocity profile of a specified rotational line, for a given observing beam-size, we first calculate $T_b(p,V_p)$, the excess brightness temperature in the line at an offset velocity V_p from the center, received by an observer from a direction intersecting the envelope at a projected distance p from the center of the envelope. This can be expressed as

$$T_b(p,V_p) = \int_{\tau_2}^{\tau_1} I(r)\ d\tau(p,V_p) \tag{3.8}$$

where

$$I(r) = (c^2/2k\nu_0^2)\{B_{\nu_0}[T_{ex}(r)] - B_{\nu_0}[T_{BB}]\} \tag{3.9}$$

is the intensity expressed in temperature units. The quantity $B_\nu(T)$ is the Planck function at frequency ν and temperature T; T_{ex} and T_{BB} are, respectively, the excitation temperature of the observed transition and the temperature of the background continuum, and ν_0 is the rest frequency of the observed transition. The radius r, the impact parameter p, and the offset velocity V_p are related by the equation

$$r^2 = p^2 \ /\ [\ 1 - (V_p/V)^2\ ]. \tag{3.10}$$

The integration limits τ_1 and τ_2, respectively, are the optical depths from infinity into the points r_1 and r_2, defined by equation (3.10), with V_p replaced by $V_p - \Delta V/2$ and $V_p + \Delta V/2$. (For the assumed rectangular shape of the intrinsic line profile, emission at velocity V_p arises only from molecules lying along the line of sight between r_1 and r_2.)

The brightness distribution of the envelope in the line, at velocity V_p, is then convolved with a Gaussian beam response having a full width at half-maximum equal to the beam-size of the observing antenna. We thus obtain the model antenna temperature in the specified line as a function of velocity, for comparison with the observed line profile.

We have tested our numerical scheme by comparing the model predictions with analytical results for several limiting cases. For an envelope unresolved by the beam, the model profiles for optically thin lines are flat-topped, whereas those for optically thick lines are parabolic, in agreement with the analytical expressions given by Morris (1975, Appendix). For an envelope with high gas density, where the collision rates dominate the radiative rates, the model excitation temperatures for all lines are close to the adopted kinetic temperature, as expected. For an envelope with very low gas density, such that the radiative rates dominate the collisional ones, with both the central infrared source and background continuum having the same temperature T_{IR}, the excitation temperatures of all lines in the model have the same value T_{IR}.

In the next chapter, we use our numerical scheme to model our observations of SiS lines from the IRC +10216 envelope, which were described in the previous chapter.

FIGURE CAPTIONS

Figure 3.1. The radiative contact zone for a molecule (located at P) in a spherical envelope expanding with constant velocity V, at two different velocity offsets (Δ) from line center. The unbroken traces display the correct zone shape (as described in this chapter), whereas the broken traces display the zone shape described by Morris and Alcock (1977).

Figure 3.2. The division of the circumstellar envelope for calculating the mean angle-averaged, velocity-averaged intensity J in a given line for a molecule located at P. The elliptical curves represent the boundaries of the spherical thin shells into which the envelope is divided. The contribution to the mean intensity (at P) at a fractional velocity offset $\Delta V/V = 0.05$, comes from the volume enclosed by the radiative contact zone boundary (heavy trace) rotated around the X-axis.

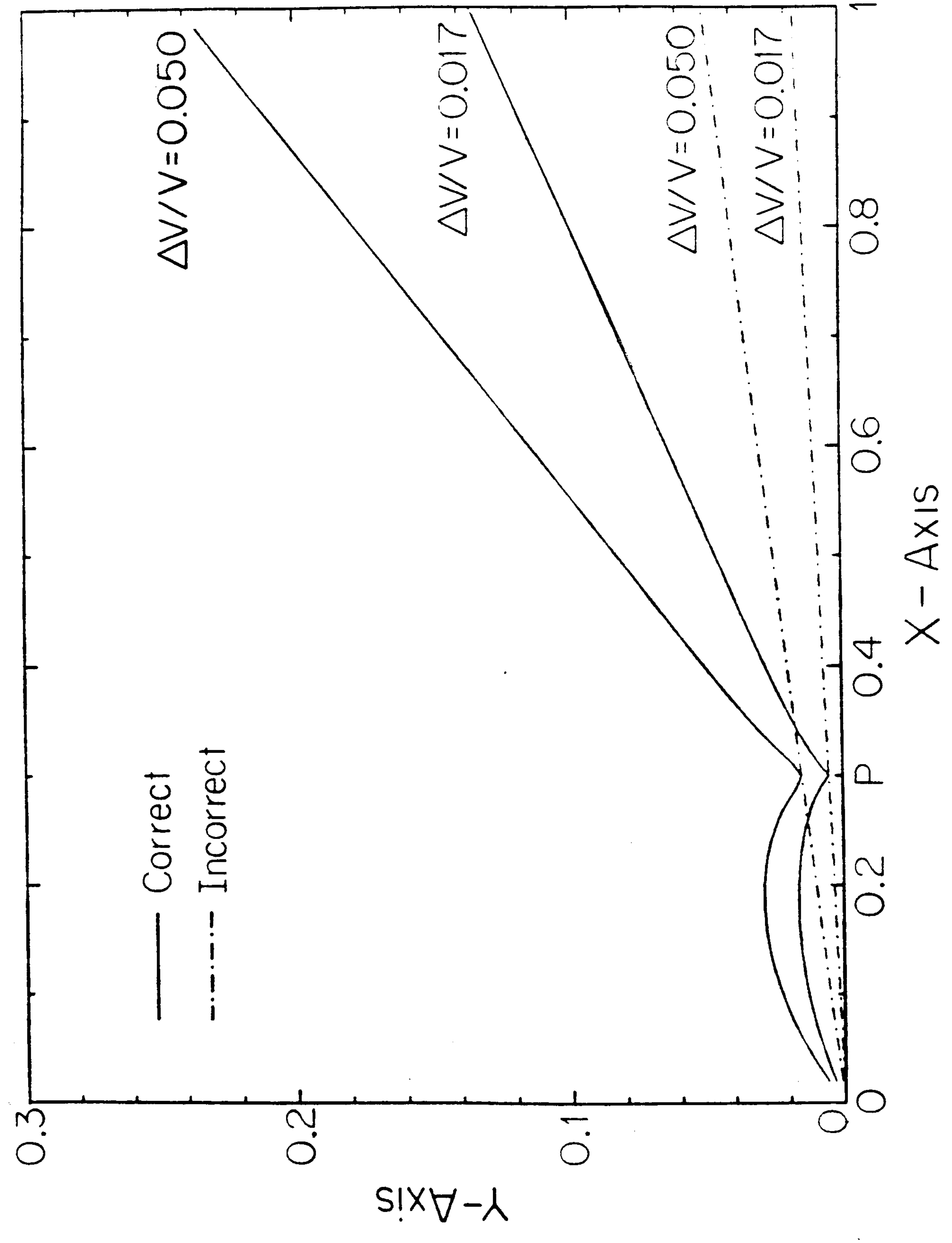
ΔV/V=0.050
ΔV/V=0.017
ΔV/V=0.050
ΔV/V=0.017
Correct
Incorrect
X - Axis
Y - Axis
0
0.2
0.4
P
0.6
0.8
1
0
0.1
0.2
0.3

FIGURE 3.1

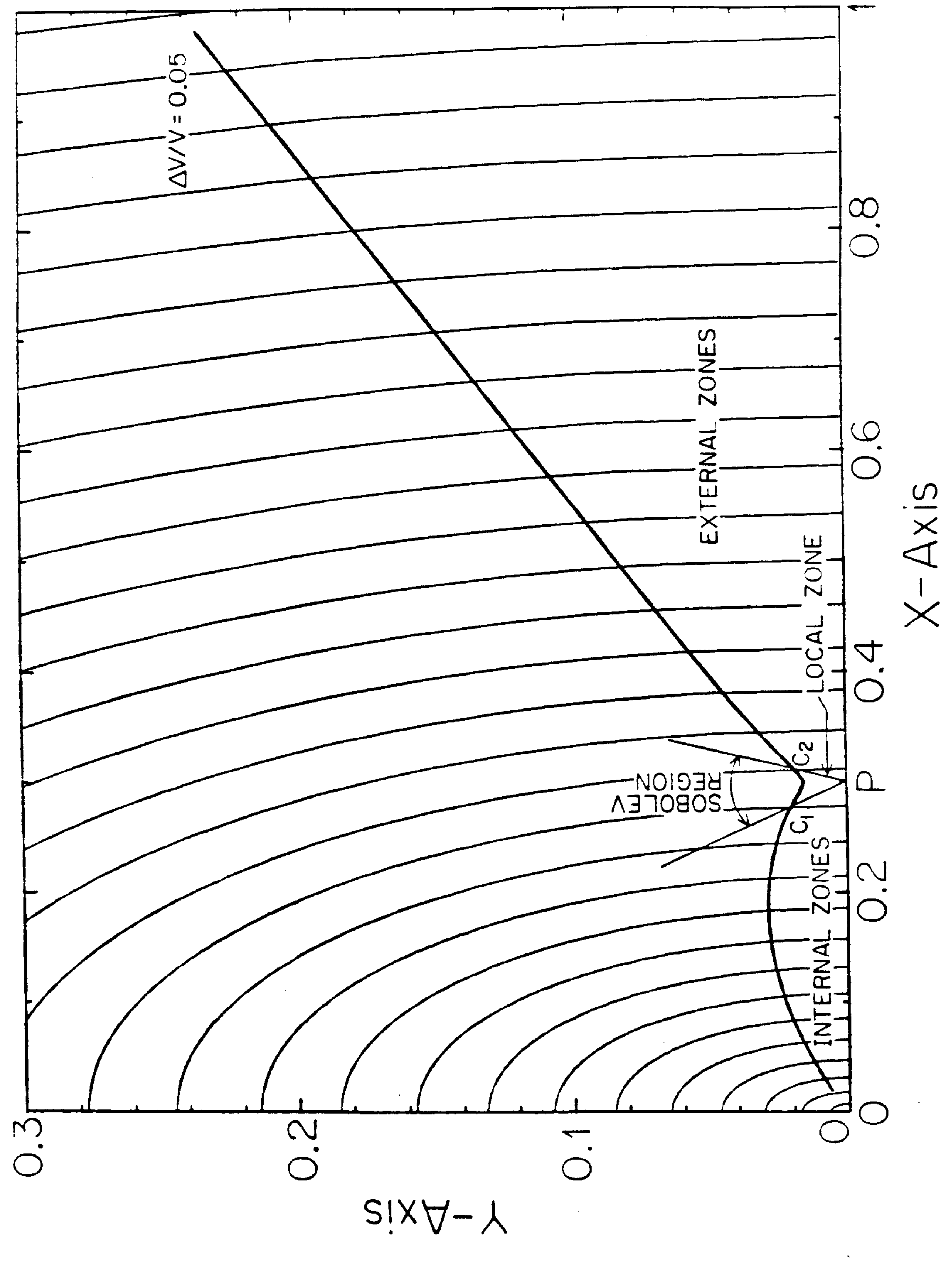
ΔV/V = 0.05
EXTERNAL ZONES
LOCAL ZONE
SOBOLEV REGION
INTERNAL ZONES
C_1
C_2
P
X-Axis
Y-Axis
0
0.2
0.4
0.6
0.8
0
0.1
0.2
0.3

FIGURE 3.2

CHAPTER 4

MODELS OF SiS LINES FROM IRC +10216 AND OTHER STARS

Note: - - Chapter 4 is included in a paper entitled 'SiS in Circumstellar Shells' (Sahai, R., Wootten, A., and Clegg, R. E. S. 1984, The Astrophysical Journal, Vol. 284).

4.1. THE IRC +10216 OUTER ENVELOPE

a) Physical features

The structure of the circumstellar shell of IRC +10216 has been discussed in detail by numerous authors. In our model the variation of gas density with radius has been taken to be a power law of the form $n(r) = k\ r^{-\alpha}$. A constant loss rate of SiS molecules has been assumed. This corresponds to $\alpha = 2$ in the region of the shell where the expansion velocity has reached its terminal value. The expansion velocity has been modeled after Goldreich and Scoville (1976) to approach 15 km s^{-1} asymptotically. The numerical constant k is derived from the mass loss rate M, assumed to be $9 \times 10^{-5}\ M_{\odot}\ yr^{-1}$ (Kwan and Linke 1982) for our adopted distance of 300 pc. In the inner regions of the shell, where the outflow is in a state of acceleration, the parameter k is allowed to vary with radius, while α is kept equal to 2. A local microturbulence of 0.67 km s^{-1} (discussed later) has been superposed.

b) SiS Excitation

Radiative processes dominate the excitation of SiS in IRC +10216, as first noted by Morris (1975). The molecule is excited from the ground to the first vibrational state by absorption of photons at 13.34 µm. The flux at 13 µm is emitted by dust grains which have been heated by stellar radiation.

In our model, the infrared radiation field has been approximated by a 600 K blackbody approximately 2 x 10^{15} cm in radius, which matches the 10 μm source observed by Toombs et al. (1972). The radius is allowed to vary in the calculations to match the observed variation of the infrared flux from the envelope at 12 μm, which amounts roughly to a factor of 3 from maximum to minimum (Merrill 1983). At phase 0.0 of the infrared light cycle, which we will refer to as "maximum light," the 13 μm continuum flux is taken to be 1.2 x 10^{-13} Watts cm^{-2} μm^{-1}, and at phase 0.5, or "minimum light," the flux is one-third this value. The cosmic background radiation and trapped SiS line radiation have been included in the calculation of the radiative excitation of the V = 0 rotational levels.

Radiative rates in the rotational levels have been calculated using a dipole moment of 1.73 Debyes. The absorption strength of the fundamental vibrational band of SiS in the gas phase is unknown. Atkins and Timms (1977) have observed this band by trapping SiS in a krypton matrix at 12 K. Timms (1982) finds an absorption strength 0.2 times the strength of the SiO fundamental band, for which a measured value is available. From this we estimate that the infrared matrix element might be μ_{IR} = 0.06 Debyes, which is much smaller than the μ_{IR} = 0.7 Debyes required by HMM in their model of the J = 1-0 maser emission. We have also found that the smaller value does not adequately reproduce the observations and have adopted an intermediate value of μ_{IR} = 0.15

Debyes.

Collisional excitation has also been included using CO-H_2 cross sections (Green and Thaddeus 1976) for transitions in the ground vibrational state of SiS. The gas kinetic temperature, required for the above, is assumed to vary with radius as given by Kwan and Hill (1977). Collisional excitation of SiS lines is not important in the IRC +10216 envelope, so the particular choice of cross sections and kinetic temperature only weakly affects our results.

c) Photodissociation and Radial Abundance

Since so many transitions of SiS have been observed, each of which has a different sensitivity to various regions of the shell, we have included a radial variation of the SiS abundance as a parameter in our model. The abundance of SiS is expected to decrease as the molecules are photodissociated in the outer envelope (Huggins and Glassgold 1982). As the extent of SiS emission in the shell appears to be quite limited (Olofsson et al. 1982), we have used an upper limit to the photodissociation rate to judge the importance of this process in the shell.

Physical parameters for the SiS molecule are lacking in the literature, and we could uncover no data on its photodissociation. For a dissociation energy of 6.42 eV, the threshold must lie below 1930 Å, and electronic transitions have been observed only down to

2386 Å at present. We write the photodissociation rate as $R = R_0 \exp(-\beta A_V)$, where R_0 is the rate for the unattenuated interstellar ultraviolet radiation field, and β is a scaling factor. Prasad and Huntress (1980) estimate β to be 2.3 and R_0 to be 10^{-10} s^{-1}. HMM estimate R_0 to be 10^{-11}. An upper limit may be calculated from the f-value sum rule, and we can write

$$R_0 = (\pi e^2/mc)\phi f < 4.5 \times 10^{-9} \ s^{-1},$$

where ϕ, the intensity of the unattenuated ultraviolet field in photons $cm^{-2} s^{-1} Hz^{-1}$ is taken from the expression in van Dishoeck and Black (1982), evaluated at 1900 Å. We have adopted for our calculations $R_0 = 1.6 \times 10^{-9}$ s^{-1} and $\beta = 3.9$. Figure 4.1 shows the adopted variation of SiS, and the photodissociation byproducts S and S^+ with radius, generated using the analysis given by Huggins and Glassgold (1982). Specifically, we used equation (B7) in Appendix B of their paper, where the parameter M is related to β through the relation $M = 1.05 \times 10^{21} \beta^{-1}$.

The adopted photodissociation rate, R_0, in the absence of dust extinction, is anomalously large when compared with that of other diatomic molecules such as CO (5×10^{-12}) and CS(1×10^{-11}). However, we require such a large photodissociation rate to limit the extent of the SiS shell to a fractional abundance at 9×10^{16} cm, of one-half the 'undissociated' value in the shielded inner envelope ($r < 5 \times 10^{16}$ cm), in order to produce the rounded shapes of the observed J = 7-6 and J = 6-5 lines at OVRO, and the intensities, relative to the on-source intensity, of the J = 5-4 line observed with the Onsala beam at offsets of 22" and 44" (Olofsson et al. 1982). We discuss later how unique our particular choice of β is.

Amalgamation onto grains provides a possible sink for SiS molecules which might operate at smaller radii than photodissociation. Because of the large uncertainties in grain surface processes, prudence dictates that the extent of SiS emission is best treated as a variable in our model. The outer radius of the circumstellar shell is taken to be 1.5×10^{17} cm. At this radius, the SiS abundance has fallen to less than 0.2 % of the undissociated abundance, and the contribution to the line emission from larger radii can be ignored. The best fit to the observed lineshapes occurs for the model with an undissociated abundance ratio of $[SiS]/[H_2] = 2.4 \times 10^{-7}$.

d) Intrinsic Line Width

A value of 0.67 km s^{-1} was adopted for the intrinsic line width ΔV, but models were also tried with $\Delta V = 0.22$ and 0.31 km s^{-1} since HMM suggested a value of 0.3 km s^{-1}, based on their observations of the masing blue wing of the J = 1-0 line. The effect of decreasing ΔV, as demonstrated in the SiO models of Morris and Alcock (1977), is to increase the radial optical depth and thus reduce the IR flux reaching a given radius. This results in a significant decrease in the intensities of the high-J lines.

In our models, the antenna temperatures of the J = 12-11 line were 0.33, 0.26 and 0.20 K at ΔV values of 0.67, 0.31 and 0.22 km s^{-1}, whereas the observed intensity is 0.66 ± .24 K (3σ). A second constraint on ΔV is provided by the sharp cusps observed in the line wings of the J = 5-4 line at 13 km s^{-1}. For ΔV = 0.67, the cusps in the model profile occur at 13 km s^{-1}; however, for ΔV = 0.22 and 0.31 km s^{-1}, they occur at 14.5 km s^{-1}. Thus, the observed values for the T_R of the J = 12-11 and other high J lines and the velocities of the cusps of the Onsala 5-4 line are best fitted with a intrinsic line-width ΔV = 0.67 km s^{-1}.

The difference between our value of ΔV and the value suggested from the 1-0 observations (HMM) could be understood if the local microturbulent line width were not constant throughout the envelope and if the 1-0 line were produced in a different spatial region of the envelope from the J = 5-4 and higher J lines. Support for this contention is given below. It is also possible that the widths of the masing features have been reduced below the Doppler linewidth because of gain narrowing (Goldreich and Kwan, 1974). In fact, HMM say that the actual microturbulent linewidth could be 0.5 km s^{-1} if line narrowing in an unsaturated maser was accounted for.

4.2. MODEL CALCULATIONS

a) Excitation Temperatures and Optical Depths

The modeling program computes the populations of the twenty lowest rotational levels in the ground and first excited vibrational states of SiS as a function of radius. These are then used to calculate line profiles of the observed transitions as seen by the various telescopes.

Curves of excitation temperature and tangential optical depth as a function of radius are shown for a number of representative transitions in Figure 4.2. For transitions from J = 1-0 to J = 5-4, a population inversion occurs in the inner regions of the envelope. This inversion occurs because the process of infrared excitation and decay results in a net upward shift in the populations of the ground and lowest few rotational states (Morris and Alcock 1977). This shift is sensitive to the infrared flux and the inversion reaches higher transitions as the infrared flux from the hot dust increases.

The excitation temperature of the 1-0 transition (Figure 4.2a) remains negative over the radial extent of the envelope which we have considered. At maximum light, the excitation temperature is even more negative, as the population shifts to higher levels. The optical depth for this transition is small, however, because of the low populations. For a model tailored to match the lower luminosity star CIT 6, with an apparently less massive envelope, the region of inversion is still present, but with more limited radial extent because the 13 μm flux is smaller. The optical depths in this case are even smaller due to the lower mass loss rate. In the CIT 6 model, no population inversion occurs in transitions higher than the J = 1-0 line.

The negative excitation temperature for the J = 5-4 line occurs over a more limited radial extent than for J = 1-0, since it is higher up the rotational ladder (Fig. 4.2a). The radius of the region with inverted populations nearly doubles in size as the luminosity of IRC +10216 increases from minimum to maximum light. Although the J = 5-4 optical depths remain low, they are higher than the J = 1-0 line optical depths (at maximum light) and very weak maser emission could be detectable. The behavior of two higher transitions in IRC +10216 is displayed in Figure 4.2b. The J = 7-6 and J = 12-11 lines require sufficiently high excitation so that population inversions do not occur in the region of the envelope which we have studied, though the curves for the J = 7-6 line excitation temperature and optical depth at maximum light show evidence that an inversion of these levels is incipient. The optical depth for these transitions is considerably higher at minimum light, when they contain relatively larger fractions of the total SiS population. The radius at which highest τ occurs moves outward only slightly as the star brightens.

A detailed examination of the model line profiles indicates that weak maser emission is expected to be a characteristic of lines lower than the J = 5-4 line, and that this emission has its largest observable effect at maximum light. These profiles demonstrate how the dilemma posed by the observed differing line shapes might be resolved: the discordant Onsala J = 5-4 profile was obtained closest to maximum light, and it was observed with the smallest beam, which should focus on the inner region with population inversion. The cusps on that profile almost certainly originate in weak maser emission such as we have described. Interferometric measurements of this line with approximately 8″ resolution, corresponding to the theoretical size of the masing region, would provide a definitive test of our model.

b) Time-Variability

We have not endeavored to solve the level populations in their full time varying detail. However, the SiS excitation in IRC +10216 is predominantly radiative, and the radiative rates are fast compared with the stellar period. Therefore, the time variability of SiS emission should be described well by a sequence of steady-state models.

Aside from the maser emission, intensity variations might be observable in the other low-lying SiS lines as the star varies. Our models suggest that this effect would be most observable in the lowest transitions since the variations above the J = 6-5 line occur within a small fractional area of a 1′ beam. Interestingly, the lowest lying levels should vary in a sense opposite to the stellar variation due to population shifting upward as the star brightens. For lines at $\lambda \sim 1$ mm, the variation should occur in the same sense as the stellar variation, but it will be of smaller magnitude as the SiS populations are diluted by being spread over many levels. In our models, the variation is least apparent in the $J = 6\text{-}5$ line. Careful monitoring of the variability of the lower transitions and a measurement of any phase lag between one of these and the stellar variability could yield valuable information on the radial location of the emitting regions.

In Figures 4.3a and 4.3b we show computed profiles at maximum and minimum light for the $J = 5\text{-}4$(Onsala), $J = 6\text{-}5$(OVRO), $J = 7\text{-}6$(OVRO), $J = 12\text{-}11$(MWO), and $J = 13\text{-}12$(MWO) lines appropriate for the observations of IRC +10216 (Figure 4.3c shows the predictions for a model of the less luminous, lower mass-loss star CIT 6). The pronounced double peaked shape of the $J = 5\text{-}4$ line results from the weak maser emission we have described in the inner regions of the shell. The highest optical depths in all the lines occur at the extreme velocities, so it is there that the effects of the infrared excitation are most pronounced. The cusped feature is very sensitive to the stellar 13 μm flux, as can be seen from the maximum and minimum light profiles shown in Figures 4.3a and 4.3b, respectively. In fact, as Table 2.1 shows, the $J = 2\text{-}1$ and $J = 7\text{-}6$ profiles were obtained at minimum light, while the rest were obtained nearer to maximum light, and the discordant Onsala J = 5-4 profile was obtained closest to maximum light of all those in Table 2.1. It is significant that the flat-topped profile of the J = 5-4 line published by Morris et al. (1975) was taken near minimum light (phase = 0.4) with the 1'.25 NRAO beam.

A recent (1984 May 5) measurement (Olofsson 1984) of the J = 5-4 line at Onsala near minimum light provides excellent support for our model. The line profile has a slightly concave shape and shows no evidence for the sharp cusps seen in the maximum light profile, in good agreement with the model profile for the 5-4 line shown in Figure 4.3b.

We also computed the J = 5-4 line profile for the Onsala beam offset from the center of IRC +10216. The intensities in the center of the line are 0.67 K and 0.12 K at offsets of 22 and 44 arc-seconds, which are 57 and 10 % of the on-source line intensity, in good agreement with Olofsson et al. (1982) who obtain 60 and 10 %. Unfortunately, they do not present spectra at the offset map points with sufficient velocity resolution to enable us to compare our model profiles with the observed ones. At 22" offset, the line wings in our model are strongly suppressed and the line appears almost flat-topped, whereas at 44" the line looks rounded. This is in agreement with their qualitative description of the offset spectra.

To test the uniqueness of our choice of β (the ratio between the the extinction at the photodissociation frequency and the visual extinction) models were also computed with $\beta = 2.3$ (as given by Prasad and Huntress 1980). This resulted in J = 5-4 relative line intensities of 50 and 6 % at 22" and 44", in disagreement with the observations. However, the poorer signal-to-noise ratio in the offset spectra as compared with the on-source spectrum does not completely rule out such a value of β.

Our model profile of the J = 5-4 line as would be observed in the FCRAO beam at maximum light is doubly peaked with cusps 1.1 times stronger than the line center. This is in reasonable accord with the observed cusp-to-center ratio of 1.2. Our predicted absolute line-center intensity is 0.68, as compared with the observed value of 0.73 (Fig. 1b).

We have also modelled the J = 4-3 line, observed at Onsala (Nguyen-Q-Rieu et al. 1984, Johansson et al. 1983) in 1982 November, close to phase 0.5 of the infrared light cycle. The predicted profile from our minimum light model has an intensity of 0.85 K at the line-centre, as compared with 0.8 K from the observations. However, the fit is not perfect, because the model profile shows a slight increase in intensity towards the edges, reaching a maximum intensity of 0.94 K at 13 km s^{-1}, whereas the observed line profile is mostly flat-topped with slightly rounded edges.

c) Infrared Line Overlaps

Though the model described above produces line profiles in reasonable agreement with observations, there are some differences which require discussion. In particular, for the Onsala J = 5-4 line, the observed ratio of the antenna temperature in the line wings to that in the center is 1.4, whereas our model gives a ratio of 1.25. Also, whereas our model predicts roughly comparable intensities for the high J lines from J = 12-11 to J = 16-15, our observations show that, although this is the case for the J = 12-11, 13-12, 14-13, and 16-15 lines, the J = 15-14 line is anomalously strong. The J = 1-0 line, whose masing line wings are also not well produced by our model, will be discussed later. It seems, therefore, that there exists some physical process, not considered in our model, that selectively overexcites the J = 5-4 and J = 15-14 lines.

The overlap of infrared lines in the 13.4 μm region from some other molecule with selected vibration-rotation lines of SiS is a likely candidate to explain the two anomalies. Assuming that a single molecule is responsible, we narrowed our search by noting that (1) it should be an abundant molecule in the carbon-rich atmosphere of IRC +10216, with a strong infrared band in the 13.5 μm region, and (2) succesive infrared lines in the band should be separated by an integer fraction of separation between the vibration-rotation lines R(4) and R(14) of SiS, in order that the overlap occur. Since the separation between succesive infrared vibration-rotation lines is directly proportional to the rotational constant B_0, it was clear that the interfering molecule must have a rotation constant either 10 times or 5 times that of SiS. A value of 5 would imply that the R(9) SiS line would also overlap, resulting in an anomalous J = 10-9 line intensity (unobservable from the ground due to an atmospheric water line at 180 GHz). Since we could not find an obvious molecule with a rotation constant 10 times that of SiS, we tried 5 and found an immediate answer - HCN! Its J = 1-0 line at 90 GHz is 5 times the frequency of the J = 1-0 line of SiS at 18 GHz and it has its lowest excited vibrational state 14 μm above the ground state.

To verify that the proposed overlap does exist, we have compared the SiS vibration-rotation line frequencies, calculated using the molecular constants given by Huber and Herzberg (1979), with those of HCN given by Yin and Rao (1972) for the ν_2 vibrational mode. And indeed, we find the following overlaps (in order of increasing wavenumber) :

SiS	HCN
P(14)=735.74 cm^{-1}	R(7) =735.616 cm^{-1}
P(5) =741.43 cm^{-1}	R(9) =741.508 cm^{-1}
R(4) =747.47 cm^{-1}	R(11)=747.406 cm^{-1}
R(9) =750.38 cm^{-1}	R(12)=750.347 cm^{-1}
R(14)=753.22 cm^{-1}	R(13)=753.293 cm^{-1}

A search for other molecules with strong infrared bands in this region reveals that acetylene (C_2H_2) also has an intense infrared band in the 14 μm region. The frequencies of the C_2H_2 lines have been taken from the high resolution measurements of Palmer, Mickelson, and Rao (1972). The overlapping lines are listed below :

SiS	C_2H_2
P(17)=733.80 cm^{-1}	R(1) =733.860 cm^{-1}
P(13)=736.39 cm^{-1}	R(2) =736.222 cm^{-1}
P(6) =740.81 cm^{-1}	R(4) =740.919 cm^{-1}
P(2) =743.27 cm^{-1}	R(5) =743.267 cm^{-1}
R(1) =745.69 cm^{-1}	R(6) =745.619 cm^{-1}
R(5) =748.06 cm^{-1}	R(7) =747.968 cm^{-1}
R(9) =750.38 cm^{-1}	R(8) =750.300 cm^{-1}
R(13)=752.65 cm^{-1}	R(9) =752.668 cm^{-1}
R(17)=754.88 cm^{-1}	R(9) =755.003 cm^{-1}

The molecular constants used for calculating the SiS frequencies are not very well determined. The most uncertain is ω_e, for which the 1 σ error limit is 0.16 cm^{-1} (as quoted in Table VIII of Harris et al. 1982), with smaller uncertainties in the other constants. These uncertainties have been kept in mind while making our list of overlaps.

Intense absorption lines of the ν_1 band of C_2H_2 at 3300 cm^{-1}, and the ν_3 band of HCN at 3312 cm^{-1} have already been observed by Ridgway, Carbon, and Hall (1978) in the circumstellar shell around IRC +10216. P Cygni emission can be seen redwards of the absorption features in their spectrum. Therefore, there can be no doubt that the ν_5 band of C_2H_2 and the ν_2 band of HCN will produce deep absorption at the expansion velocity, and substantial emission redwards of the absorption feature, because these bands are as strong (in C_2H_2) or stronger (in HCN) than the observed ones. In fact, a spectrum of IRC +10216 in the 12 μm region shows P Cygni profiles for lines identified to be from the C_2H_2 ν_5 band (Ridgway 1984).

d) The J = 1-0 Line

The observed J = 1-0 profile differs from all others in its very strong line wing emission, as Figure 2.1 shows. Our model has been tailored to reproduce the spectra observed in the higher rotational lines and does not reproduce the wing features of the J = 1-0 spectrum. HMM proposed a model which matched the J = 1-0 line fairly well, but they did not give any predictions for the higher transitions. It differs from ours in several respects. First, it requires an SiS abundance twice as large as that which best fits all the high rotational lines we have modeled, but is probably within reasonable estimates of the abundance uncertainty. Second, HMM treat μ_{IR} as a free parameter, choosing a value of 0.7

Debyes, which is rather large for similar molecules [e.g., $\mu_{IR}(SiO) = 0.093$, $\mu_{IR}(CO) = 0.096$], and much larger than the only laboratory estimate (Timms 1982). Third, HMM account for the red/blue asymmetry of the J = 1-0 line by assuming a $\lambda = 1.6$ cm flux density of 15 mJy from IRC +10216, three times the value measured at 1.5 cm by Sahai and Claussen (1984).

We believe it is likely that the J = 1-0 maser arises near the central star, a region which is particularly difficult to model correctly. As HMM note, the unusual asymmetry of the J = 1-0 line can be explained by occultation effects if the maser is fairly strong and occurs near the central star. Our model cannot properly treat this region, where the dust creating the infrared flux permeates the SiS emitting region and the infrared radiation field does not vary as r^{-2}, although the density still may. A complete model should treat transfer of the infrared continuum radiation and include the non-spherical infrared structure of the central region (McCarthy, Howell, and Low 1980). It should also treat excitation of the rotational lines by the central radio continuum source, whose strength is now measured. Last, the model we have used incorporates too coarse a zoning of the flow in the interior regions, and probably cannot succesfully treat them.

The overlap of the R(1) SiS line with the R(6) C_2H_2 line, corresponding to the C_2H_2 line being redward of the SiS line, could substantially decrease the infrared continuum if the overlapping lines were closer in frequency, and this possibility is not ruled out in view of the uncertainties in the SiS frequencies. In such a case, there would be an increase in the population in the $J = 1$, $V = 0$ state, producing a larger optical depth in the 1-0 transition, thus enhancing the emission in the masing features.

4.3. THE SiS ABUNDANCE IN OTHER SHELLS

Detailed models cannot be tailored to the other circumstellar shells from which we have sought or detected SiS emission, as the available data are too scanty to provide adequate constraints. Accordingly, we have used luminosities, distances, and mass loss rates from the literature to choose the more representative of the three models described in Table 4.1. The run of T_{ex} with radius is taken from the appropriate model.

We assume that, for small differences in abundance, scaling the emergent profiles is an adequate procedure for estimating the abundances of SiS in these other shells. For each star a profile is calculated using the treatment described by Kuiper et al. (1976). From this scaling process, the relative SiS abundances and limits have been obtained for the other objects and listed in Tables 4.2a and 4.2b.

We find no evidence that any of the detected sources has a relative SiS abundance which is appreciably different from IRC +10216, and in most of the undetected sources it is clear that our sensitivity was not sufficiently high to yield a detection.

For the detected sources, which are all carbon stars, that abundance is far below the cosmic Si or S abundance, which we take as evidence that at least one of the two elements is severely depleted onto grains in carbon stars as a class.

The limit on the O-rich circumstellar envelopes is also of interest. In the O-rich photospheres, Si is expected to be fully associated in SiO. However, around stars with chromospheres the degree of molecular association may be severely reduced by UV radiation (Clegg, van IJzendoorn, and Allamandola 1983). Scalo and Slavsky (1980) showed that SiS would form from ion-molecule reactions in an expanding shell in which Si was in atomic form initially. We have compared their prediction with the upper limit from one of our best spectra, that of RX Boo. For a star with the mass loss rate and distance given in Table 4.2a for RX Boo, we find from Figure 2 of Scalo and Slavsky that the expected SiS abundance, as observed with our sensitivity, would be undetectable. Since this is our best upper limit, it is clear that the actual detection of SiS from O-rich shells may be impossible at the sensitivity of the current survey. More sensitive limits than the present one could be made by observing O-rich stars with the highest mass loss rates ($dM/dt = 10^{-4}\ M_{\odot}\ yr^{-1}$). Knapp et al. (1982) suggest that IRC +10011 is such an object, although its dust shell may be sufficiently optically thick that a detailed radiative transfer model is necessary to predict the photo-induced reactions which produce SiS.

4.4. DEPLETION OF Si OR S?

Around cool carbon stars thermodynamic equilibrium calculations suggest that most S atoms are in SiS if condensation of solid particles is not allowed. Since the cosmic sulfur abundance is approximately 1.5 x 10^{-5}, and our observations indicate typical SiS abundances relative to H_2 of 3 x 10^{-7} (Tables 4.2a, 4.2b), it is clear that this is not realized, and by large (10^{-2}) factors. The next most abundant sulfur compound, CS, is expected to deplete only a small fraction of the available sulfur, because chemical models predict the CS abundance to be at least 10–100 times smaller than the predicted SiS abundance, the exact number depending on the temperature at which the equilibrium is calculated (Lafont, Lucas, and Omont 1982; Lambert and Clegg 1980, McCabe, Smith, and Clegg 1979).

We have used the observational evidence from the rotational lines of CS seen in IRC +10216 (J = 5-4 from Wootten 1983, J = 2-1 from Johansson et al. 1983; J = 3-2, 2-1 from Wannier and Linke 1978; and J = 2-1, 1-0 from Turner et al. 1973) to estimate its abundance. Our preliminary model of the CS excitation includes the effect of photodissociation by interstellar ultraviolet in limiting the extent of the CS shell (see Lafont, Lucas and Omont 1982 for CS photodissociation parameters, R_0 and β). The infrared continuum at the λ = 8 μm fundamental band of CS which is responsible for the excitation of the V = 0 rotational levels (Morris 1975), is assumed to be produced by thermal reemission from dust (cf. 1b). The effect of absorption due to the vibration-rotation lines of the SiO fundamental and the combination C_2H_2 band $\nu_4+\nu_5$ on the continuum (Sahai 1984), many of which overlap the CS vibration-rotation lines, has been ignored.

The relative CS abundance needed to reproduce the observed line profiles is 1.1×10^{-7}, implying thereby that the CS to SiS abundance ratio is 0.46. This is in rough agreement with the simple modelling of Johansson et al. (1983), who get 3.0×10^{-7} for the CS abundance and 0.5 for the CS/SiS abundance ratio. According to Figures 1 and 2 of Lafont et al. (1982), the relative CS abundance expected from chemical equilibrium should be about 10^{-7}; therefore the abundance of CS from observations is comparable to that from chemical equilibrium calculations. McCabe et al. (1979), who have modelled the abundances of a large number of molecules observed in IRC +10216, conclude that the CS abundance, inferred from observations, is 4 times the theoretical value. These results indicate that S is not depleted - the underabundance of SiS is a result of Si depletion. The low abundance of SiO in IRC +10216 calculated by Morris (1975) strengthens this conclusion.

The depletion of Si could occur as a result of condensation of SiC or silicate grains. The condensation temperature of SiC is 1300 K, while that of a typical silicate, Mg_2SiO_4 is 800 K (Gilman 1969; Lattimer and Grossman 1978). This implies that SiC will form before silicates, depleting the gaseous Si. The presence of an 11 μm feature attributed by Treffers and Cohen (1974) to SiC particles, and the absence of 10 μm emission, which rules out the presence of significant amounts of silicate grains, provides additional evidence that Si is locked up in SiC grains. We can estimate the amount of Si in these grains by referring to the dust model for IRC +10216 of Mitchell and Robinson (1980), in which the 11 μm feature is reproduced with a dust mixture containing 98-99 % amorphous carbon and 1-2 % (by number) of SiC particles. Therefore, the Si to C abundance ratio in the dust is approximately 0.015. The calculations of Donn et al. (1968) show that for temperatures less than 1600K (appropriate for IRC +10216), approximately 75-80 % of the total carbon should condense, regardless of the total gas pressure or the assumed C/O ratio. Assuming that the rest of the carbon is in CO and C_2H_2 in the ratio 3:1 (Lafont et al. 1982, McCabe et al. 1979), and taking the CO/H_2 ratio to be 6×10^{-4} (Kwan and Linke 1982), we obtain the result that the relative abundance (to H_2) of Si in SiC grains is 3.6-4.8×10^{-5}.

Assuming the Si abundance in IRC +10216 to be not significantly different from its cosmic value of 3.2×10^{-5}, it appears that almost all of the Si in the IRC +10216 atmosphere condenses into SiC grains. This depletion pattern for Si and S appears to be similar to that observed in planetary nebulae. Recent results for nebular S abundances (Dinerstein 1982) indicate that S is little depleted (< 50 %) from the gas phase, as judged by nebular S/O ratios. However, Si is found to be depleted by a factor 10 in several nebulae (Harrington and Marionni 1981). More accurate depletion data may strengthen the links between the planetaries and the envelopes of carbon stars.

4.5. CONCLUSIONS

A large number of SiS rotational lines have been observed from the circumstellar shell of IRC +10216. These observations, together with those already reported in the literature, were used here to construct a detailed model of the SiS vibration-rotation excitation in IRC +10216, and the following results were derived :

i) The undissociated abundance $[SiS]/[H_2]$ in the shielded inner regions of the circumstellar shell is ~ 2.4×10^{-7}.

ii) The SiS density falls steeply with increasing radius, reaching one-half the undissociated abundance at a radius of 9×10^{16} cms. If photodissociation of SiS by interstellar ultraviolet radiation is solely responsible for the decrease in density, then a large photodissociation rate of 1.6×10^{-9} s^{-1} is required, after shielding by circumstellar dust is accounted for. This suggests that some other mechanism, such as adsorption by grains, may also be contributing to the decrease of SiS abundance.

iii) The observed abundance of SiS in IRC +10216 is much smaller than that predicted by chemical models, whereas the observed abundance of CS is comparable to predictions, from which it is inferred that Si, not S depletion, is responsible for the low SiS abundance. We have given a quantitative argument to show that most of the available Si has been probably been used up in forming SiC grains in the cool IRC +10216 atmosphere.

iv) Variations in the 13 µm infrared flux over the 644 day light-cycle of IRC +10216 produce observable changes in some of the SiS lines. The sharp cusps in the J = 5-4 line wings, observed with the Onsala 20m antenna, are explained in terms of weak maser emission at light maximum.

v) Overlaps in the 13 µm region of selected vibration-rotation lines of SiS with those of the abundant molecules HCN and C_2H_2, which have not been considered in the model, may be responsible for poorer fits to some lines. It is suggested that in future models of molecular lines which are dominantly excited by the infrared continuum, possible overlaps of vibration-rotation lines with those from other abundant molecules should be carefully investigated.

vi) A search for SiS J = 7-6 and J = 6-5 lines in other carbon-rich, oxygen rich, and S-type circumstellar shells, has produced three new sources, CIT 6, CRL 2688 and IRC +20370, all of which are carbon-rich. This is consistent with chemical equilibrium models which predict SiS to be significantly more abundant in a carbon-rich environment than in an oxygen-rich environment.

Table 4.1

Models of Circumstellar Shells

A. Circumstellar Cloud

Parameter	Value	Model
Mass Loss Rate ($M_\odot$ yr^{-1})......	0.90×10^{-4}	HH, HL
	0.32×10^{-5}	L
Initial molecular abundance...	0.24×10^{-6}	HH, HL
	0.37×10^{-6}	L
Gas Density Power Law Exponent	2	
Expansion Velocity (km s^{-1})...	15	HH, HL
	17	L
Velocity law ($V_{exp}(r)/V_{max}$)..	$\exp(-5.0 \times 10^{15}/r^{1.08})$	
Line Width (km s^{-1})..........	0.675	
Microwave background temperature (K)......	2.8	
Outer Radius (cm).............	0.156×10^{18}	
Distance to cloud (pc)........	300	HH, HL
	190	L

Table 4.1 (continued)

B. Infrared Source

Parameter	Value	Model
Size (arcsec)................	1.10	HH
	0.64	HL
	0.24	L
Radius (cm)..................	0.247×10^{16}	HH
	0.144×10^{16}	HL
	0.342×10^{15}	L
Temperature (K)..............	600	HH, HL
	700	L
Flux (W cm^{-2} μm^{-1})...........	0.123×10^{-12}	HH
	0.416×10^{-13}	HL
	0.802×10^{-14}	L

NOTE.- - HH: high mass loss and maximum light; HL: high mass loss and minimum light; L: low mass loss and low luminosity.

Table 4.1 (continued)

C. SiS Radial Abundance in Circumstellar Cloud

Radius (cm)	Fractional Abundance[a]
0.345×10^{16}	1.000
0.591×10^{16}	1.000
0.928×10^{16}	1.000
0.134×10^{17}	1.000
0.182×10^{17}	1.000
0.237×10^{17}	1.000
0.297×10^{17}	1.000
0.362×10^{17}	0.999
0.433×10^{17}	0.997
0.508×10^{17}	0.988
0.588×10^{17}	0.963
0.673×10^{17}	0.907
0.762×10^{17}	0.804
0.855×10^{17}	0.647
0.953×10^{17}	0.454
0.105×10^{18}	0.264
0.116×10^{18}	0.122
0.127×10^{18}	0.042
0.138×10^{18}	0.010
0.150×10^{18}	0.002

a) At any radius, the Fractional Abundance is equal to the [SiS]/[H_2] abundance ratio at that radius divided by the initial molecular abundance, as given in A.

Table 4.2a. Limits to SiS Abundances (J = 7-6 Survey).

Object (1)	Type (2)	V_{exp} (km s^{-1}) (3)	dM/dt ($M_\odot$ yr^{-1}) (4)	Dist (pc) (5)	[SiS]/[H_2] (6)	Model (7)
CRL 618	C	22.0	1.0(-4)	1700	<8.4(-7)	HL
CRL 865	C	16.0	1.5(-4)	1580	<7.9(-7)	HL
IRC+10216	C	17.0	9.0(-5)	290	2.4(-7)	HH, HL
CIT 6	C	18.0	3.2(-6)	190	3.7(-7)	L
V Hya	C	18.0	9.2(-6)	400	<3.1(-6)	L
CRL 2688	C	20.0	7.2(-5)	1000	<1.3(-6)	HL
CRL 3068	C	15.0	2.2(-5)	570	<8.7(-7)	HL
IRC+40540	C	15.0	8.0(-5)	960	<8.4(-7)	HL
RX Boo	O	12.0	4.5(-7)	225	<3.3(-6)	L
Chi Cyg	S	12.0	1.8(-7)	97	<5.4(-6)	L
NGC 7027	P	18.0	7.8(-5)	1000	<1.6(-6)	L

Table 4.2b. Limits to SiS Abundances from J = 6-5 survey.

Object	Type	V_{exp} (km s^{-1})	dM/dt ($M_{\odot}$ yr^{-1})	Dist (pc)	[SiS]/[H_2]	Model
(1)	(2)	(3)	(4)	(5)	(6)	(7)
IK Tau	O	22.0	4.2(-6)	510	<1.5(-6)	L
IRC+10216	C	17.0	9.0(-5)	290	2.4(-7)	HH, HL
CIT 6	C	17.0	3.2(-6)	190	3.7(-7)	L
RT Vir	O	10.9				
RX Boo	O	12.0	4.5(-7)	225	<3.0(-6)	L
IRC+20370	C	9.0	2.5(-5)	790	1.5(-7)	HL
Chi Cyg	S	12.0	1.8(-7)	97	<6.0(-6)	L
V Cyg	C	13.0	2.5(-5)	610	<7.5(-7)	HL
CRL 2688	C	20.0	7.2(-5)	1000	5.0(-7)	HL

NOTE.- - In column (2): C, carbon rich; S, S star; O, oxygen rich; P, planetary nebula. Expansion velocities in column (3) are taken from Knapp (1983). Mass loss rates (col. [4]) and distances are taken from Knapp et al. (1982), except mass loss rates taken from Jura (1983) where available. In column (7): HH, high mass loss rate, maximum light; HL, high mass loss rate and minimum light; L, low mass loss rate and low stellar luminosity.

FIGURE CAPTIONS

Figure 4.1. The radial variation of the abundance (relative to H_2) of SiS, S and S^+ in the shell of IRC +10216 produced as a result of photodissociation. The value of r_0 for the ordinate is 2.1 x 10^{15} cm.

Figure 4.2. The radial variation of T_{ex} and τ in our model of the shell of IRC +10216 are shown. The value of r_0 for the ordinate is 2.1 x 10^{15} cm. Lightly drawn lines trace T_{ex} or τ at minimum light and heavily drawn lines are for maximum light. a) Variation of excitation temperature of the J = 5-4 (solid lines) and J = 1-0 (dashed lines) transitions through the shell. Both transitions have negative excitation temperatures over significant portions of the circumstellar envelope. b) Variation of excitation temperature of the J = 7-6 (solid lines) and J = 12-11 (dashed lines) transitions. Neither of these transitions has negative excitation temperature over substantial portions of the envelope. c) Variation of optical depth with radius through the shell for J = 1-0 (dashed lines) and J = 5-4 transitions (solid lines). The curves in the region of negative optical depth are indistinguishable from the fiducial τ = 0 line for all cases except the J = 1-0 line at minimum light. d) Variation of optical depth with radius through the shell for J = 7-6 (solid lines) and J = 12-11 (dashed lines) transitions.

Figure 4.3. Calculated line profiles for SiS emission in IRC +10216 derived from the models described in the text. The J = 5-4 profile is calculated for the Onsala antenna, the J = 6-5 and 7-6 for the OVRO antenna, and the J = 12-11 and 13-12 for the MWO antenna. a). Profiles calculated for maximum 13 μm light, model HH in Table 4.1. b). Profiles for 13 μm minimum light, model HL in Table 4.1. c). Profiles for model L in Table 4.1.

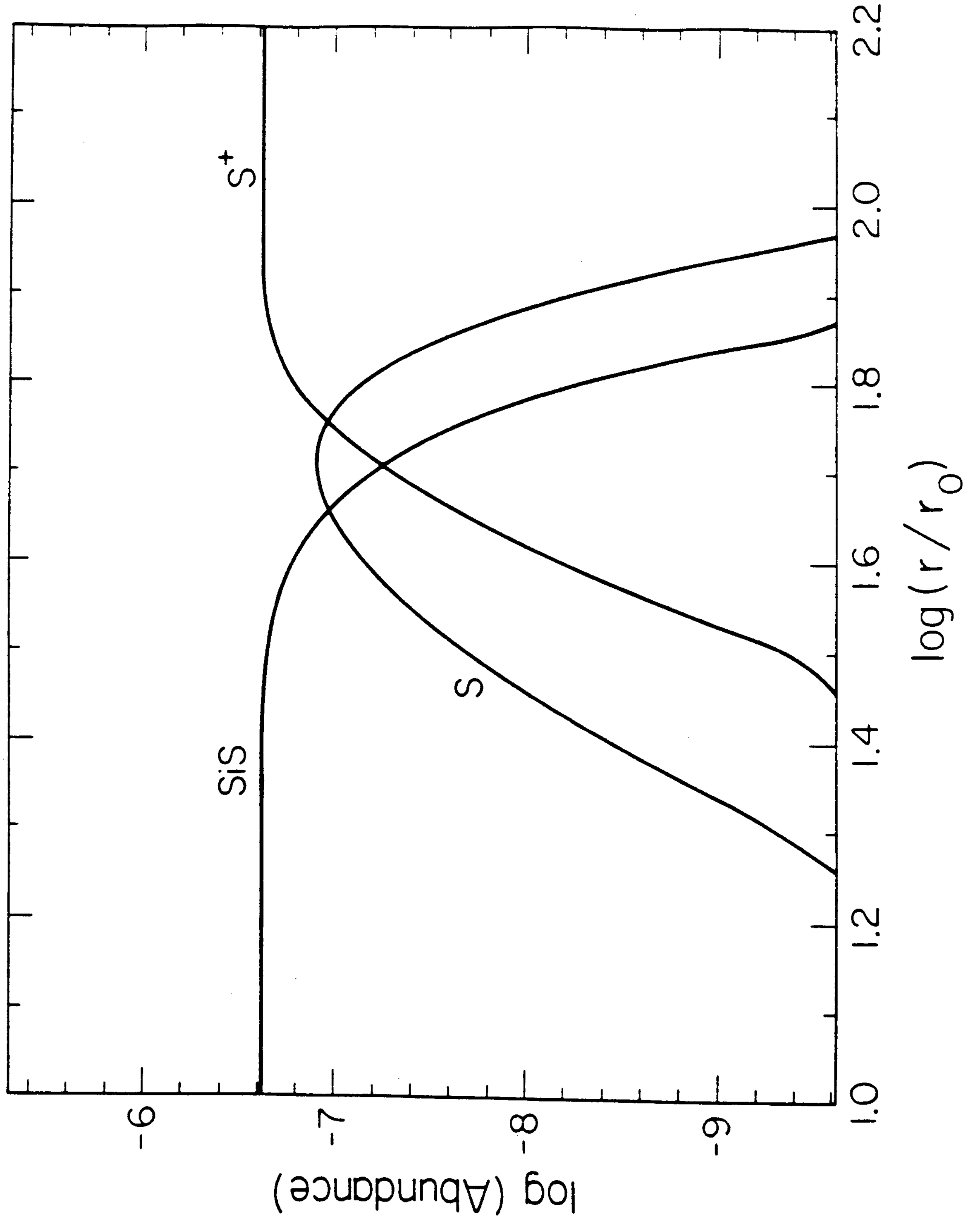

FIGURE 4.1

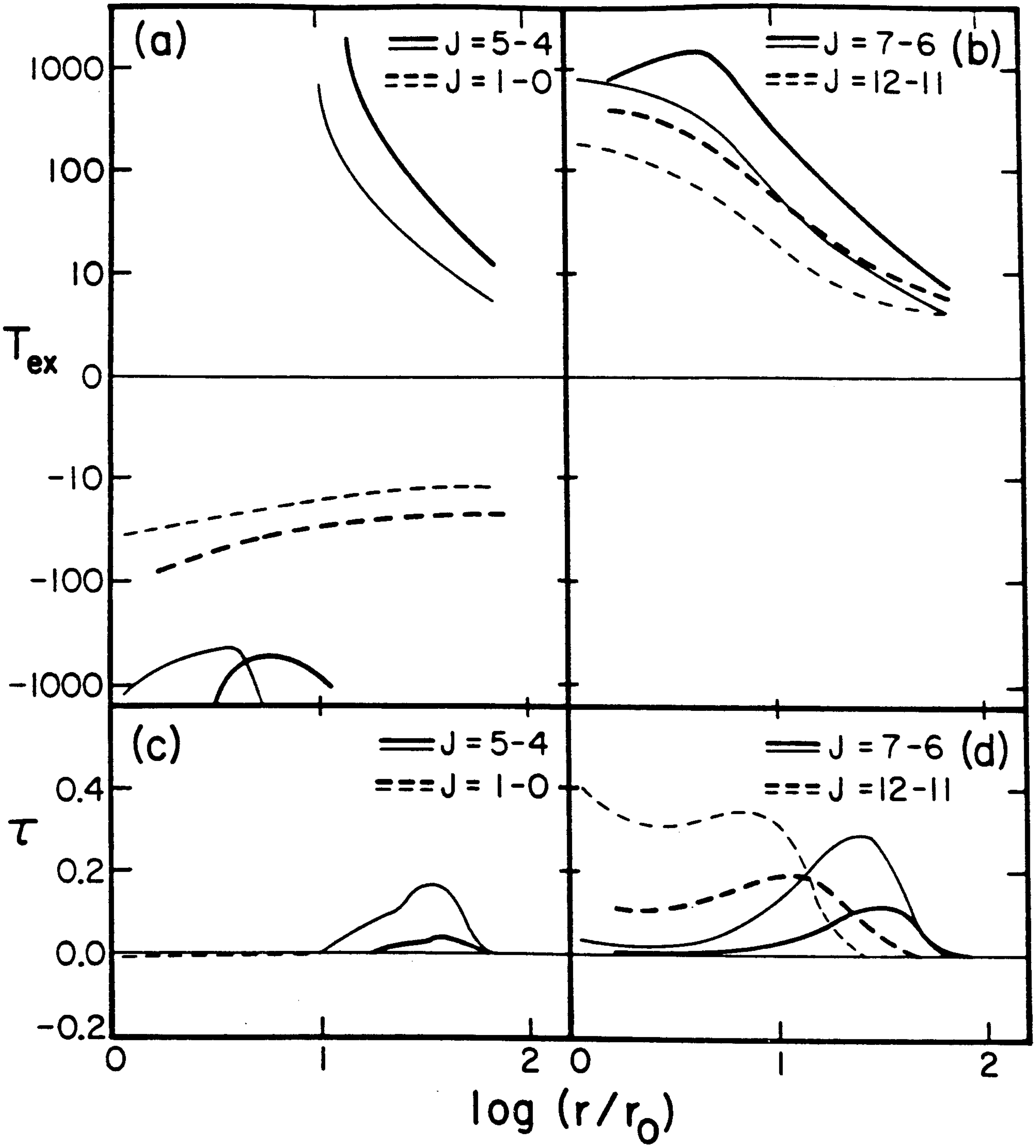
(a)
J = 5-4
J = 1-0
(b)
J = 7-6
J = 12-11
(c)
J = 5-4
J = 1-0
(d)
J = 7-6
J = 12-11
T_{ex}
1000
100
10
0
-10
-100
-1000
τ
0.4
0.2
0.0
-0.2
0
1
2
0
1
2
log (r/r$_0$)

FIGURE 4.2

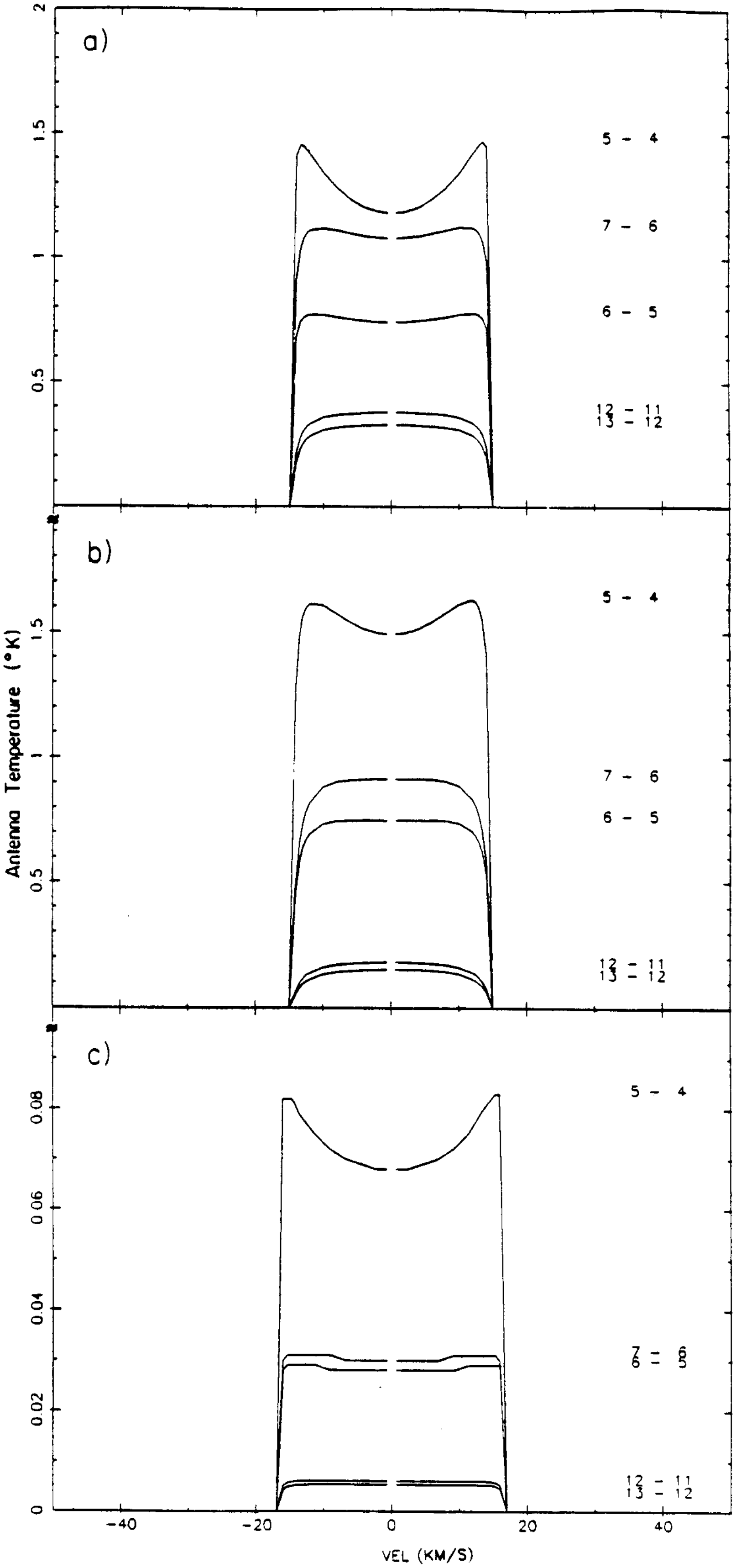
a)
5 - 4
7 - 6
6 - 5
12 - 11
13 - 12
b)
5 - 4
7 - 6
6 - 5
12 - 11
13 - 12
c)
5 - 4
7 - 6
6 - 5
12 - 11
13 - 12
Antenna Temperature (°K)
2
1.5
1
0.5
0.08
0.06
0.04
0.02
0
-40
-20
0
20
40
VEL (KM/S)

FIGURE 4.3

CHAPTER 5

4.6 MICRON CO EMISSION LINES FROM THE IRC +10216 INNER ENVELOPE

In this chapter we present observations of vibration-rotation lines of CO produced by resonance scattering of infrared radiation from the inner regions of the IRC +10216 envelope. A novel experimental technique, employing an annular aperture to mask the central infrared continuum source, was used to obtain emission line profiles at a mean angular offset of 2.7 ± 0.7" from the central infrared source. These observations overcome the inherent ambiguity in the shell radius of 'line-of-sight' measurements against the central infrared source.

5.1. OBSERVATIONS

The Fourier Transform Spectrometer (FTS) at the coude focus of the 4 m Kitt Peak Telescope was used to measure the spectrum of IRC +10216 in the 2100 to 2200 cm^{-1} range, at a frequency resolution of 0.025 cm^{-1} corresponding to 3.5 km s^{-1}. The observing dates, November 11 and 12, 1981, were selected, such that i) the source had a large velocity with respect to the telescope, thus ensuring that the deep telluric CO absorption lines were Doppler-shifted well away from the source lines, and ii) the moon was full phase during the observing period. The moon serves as an almost flat continuum source - its spectrum is therefore a spectrum of the telluric opacity.

Two types of spectra were recorded; the first (referred to as the 'circular spectrum'), through a circular aperture of diameter 2.7" , the second (referred to as the 'annular spectrum') through an annular aperture of inner and outer radii 2" and 3.45". Three pairs of detectors were used for the experiment. Two of the pairs were set up with a 100 cm^{-1} wide filter, covering the desired spectral range, with one pair having the circular aperture in front of the detector and the other with the annular aperture. The 'circular' spectra were needed to measure the continuum level, and to remove 'circular' spectral features contaminating the 'annular' spectrum. (The contamination occurs due to scattering in the earth's atmosphere, and guiding errors.)

A third pair of detectors were used to detect and guide on the 2 µm flux when the source was being observed through the annulus. The circular aperture used for the 2 µm guiding signal was optically aligned such that centering the source in this aperture would center it in the annular aperture. By maximizing the signal from this detector and minimising the signal from the 4.6 µm detector, we could ensure that the continuum source remained well-centered in the annulus. In the absence of scattering in the earths's atmosphere, the line emission, averaged over the bandpass, should contribute negligibly to the signal level in the 4.6 µm detectors, when the continuum source is well-centered in the annulus. In practice, continuum emission from the central source is spread out over several arc-seconds because of the seeing and we could always detect some continuum in the 4.6 µm detectors through the annulus. The size of the 4.6 μm seeing disc can, in principle, be estimated from a comparison of the continuum levels in the 'annular' and 'circular' spectra. (However, due to an error, the 'circular' spectra could not be calibrated -- the 4.6 μm seeing is estimated from the visual seeing).

The following table gives a description of the different scans of IRC +10216 (Scan Nos. 1,2,3,4, and 5) and the Moon (Scan No. 6), made with the annular (A) and circular (C) aperture:

Scan No.	Aperture	Visual Seeing (")	Integration Time (sec)	Airmass Range	Date
1.	A	1.5 -2.0	10024	1.52 - 1.06	11 Nov81
2.	A	1.5 -2.0	3433	1.66 - 1.33	12 Nov81
3.	A	1.5 -2.0	1607	1.16 - 1.11	12 Nov81
4.	C	1.5 -2.0	3806	1.10 - 1.25	12 Nov81
5.	C	1.5 -2.0	1877	1.25 - 1.38	12 Nov81
6.	A	1.5 -2.0	2580	1.13 - 1.23	11 Nov81

The Nov 12 scans have been co-added prior to analysis in order to improve the signal-to-noise. However, the Nov 11 and Nov 12 data have not been co-added because possible variations in the seeing from the Nov 11 observations to the Nov 12 observations, even though within the estimated 1.5 - 2.0" range, could affect the two data sets differently.

5.2. DATA REDUCTION

A specially written program was used for data reduction. First, each spectrum was divided by the instrumental frequency-response function, which depends on the geometry of the observing aperture. The instrumental response was determined by observing a tungsten lamp source illuminating the 5th mirror of the coude train on the 4 m telescope. This mirror focusses the source radiation into the FTS optics (Hall et al. 1979). Second, the spectra were corrected for telluric absorption at the airmass of the source observation. The atmospheric opacity was derived from the lunar spectrum, ratiod by a 395 K black-body curve. At 4.6 μm the contribution of reflected light from the sun is smaller than the lunar thermal emission by ~ 7 magnitudes (Hinkle, private communication 1984), and we expect negligible contamination from the solar spectrum. Figure 5.1a shows the computed opacity spectrum at one airmass.

Since the integration time for each IRC +10216 scan was typically one hour or more, during which the source traversed a significant range of airmass, the applied correction for telluric opacity was computed as a weighted average over the entire airmass range. The average correction was computed by dividing the airmass range into ten intervals, computing the attenuation at the average airmass for this interval, and weighting it with the time spent by the source in traversing this interval. The effectiveness of this correction method can be judged by comparing the spectra in Figures

5.1b and 5.1c, the latter being the corrected spectrum.

A weighting function for each spectrum is also generated, with the weight for each data point being equal to the expected signal-to-noise ratio squared. The weight is therefore taken to be equal to the integration time for the scan multiplied by the square of the atmospheric attenuation. The weight function is useful while i) determining peak intensities of the observed lines by fitting them with a theoretically computed velocity profile, and ii) fitting a model to these intensities.

5.3. MEASURING LINE INTENSITIES

The best way to measure the peak line intensities without discarding the information contained in the off-center channels is to fit a profile function (if known) to the data. In Chapter 6, we derive the following form for the velocity profile of the emission lines:

$$I(V_p) = \text{constant} \times (1 - \{V_p/V\}^2)^2 \quad .$$

Since the expansion velocity of IRC +10216 is about 15 km s^{-1} and adjacent channels in the FTS spectrum are separated by 2.5 km s^{-1}, six channels completely span the red part of the line profile - these are used in the line-fitting routine. The blue side of the line is asymmetric with respect to the red side, because superimposed on the blue emission is absorption scattered into the annulus as a result of the finite seeing. For this reason, the channels blueward of the stellar velocity were not used for line-fitting. In the least-squares fit to the red half of the line, the two parameters varied were the peak line intensity and the local continuum level.

The following tables list the measured line intensities, together with other parameters relevant to the line-fitting for the Nov 11 and Nov 12 scans. Column 1 gives the line identification, column 2 gives the number of continuum points available adjacent to the line, column 3 gives the line-intensity determined from the fit, column 4 gives the continuum level used in the fit, columns 5 and 6 give the weighted average of the residuals over the line (square-root of the average of the differences squared), and over the line and continuum points, and finally column 7 gives the sum of the weights over the line channels.

Nov 11 Scan

Line	Cont. Points	Line Intensity	Continuum Intensity	Line Residual	Total Residual	Line Weight
P 9	7	0.527	0.835	0.241(-1)	0.127(-1)	0.330
P 8	3	0.556	0.835	0.781(-2)	0.616(-2)	0.360
P 7	8	0.537	0.835	0.142(-1)	0.505(-2)	0.368
P 6	7	0.555	0.835	0.179(-1)	0.651(-2)	0.316
P 3	3	0.484	0.815	0.365(-2)	0.250(-2)	0.527
P 2	0	0.500	0.850	0.490(-2)	0.490(-2)	0.344
P 1	5	0.450	0.800	0.297(-2)	0.161(-2)	0.428
R 1	6	0.490	0.790	0.177(-2)	0.818(-3)	0.388
R 2	5	0.452	0.790	0.148(-2)	0.122(-2)	0.530
R 3	6	0.414	0.765	0.363(-2)	0.187(-2)	0.514
R 6	6	0.407	0.790	0.148(-2)	0.731(-3)	0.394
R 7	6	0.387	0.810	0.163(-2)	0.176(-2)	0.441
R 8	0	0.407	0.825	0.471(-2)	0.471(-2)	0.444
R10	3	0.439	0.815	0.507(-2)	0.552(-2)	0.134
R14	4	0.283	0.800	0.689(-2)	0.443(-2)	0.130

Nov 12 Scans

Line	Cont. Points	Line Intensity	Continuum Intensity	Line Residual	Total Residual	Line Weight
P 9	0	1.516	2.300	0.476(-1)	0.476(-1)	0.157
P 8	6	1.585	2.320	0.377(-1)	0.184(-1)	0.172
P 7	0	1.379	2.450	0.385(-1)	0.385(-1)	0.213
P 6	5	1.792	2.400	0.381(-1)	0.191(-1)	0.148
P 3	4	1.428	2.400	0.103(-1)	0.754(-2)	0.261
P 2	0	1.603	2.510	0.153(-1)	0.153(-1)	0.162
P 1	7	1.298	2.370	0.100(-1)	0.487(-2)	0.207
R 1	7	1.164	2.400	0.161(-1)	0.667(-2)	0.185
R 2	6	1.251	2.450	0.371(-2)	0.450(-2)	0.262
R 3	4	1.296	2.400	0.127(-1)	0.933(-2)	0.254
R 6	5	1.147	2.450	0.505(-2)	0.521(-2)	0.188
R 7	5	1.090	2.440	0.506(-2)	0.399(-2)	0.214
R 8	0	1.272	2.420	0.164(-1)	0.164(-1)	0.215

For many lines, such as R(6), P(3), P(2) etc., several channels beyond the edge of the red wing were also available for determining the local continuum. For the P(6), P(7), P(8) and P(9) lines, which are in wavelength regions with narrow under-resolved telluric absorption features, the opacity correction procedure does not adequately remove these features from the source spectrum. These lines lie near the edge of the 100 cm^{-1} bandpass filter where the noise level is larger than in the middle of the bandpass. For these lines, the continuum level is determined from nearby regions which have relatively fewer narrow telluric lines. Figure 5.2 displays the observed and fitted line profiles for the Nov 12 scan.

5.4. DISCUSSION

A cursory inspection of the 'circular' and 'annular' spectra reveals that, though both have P-Cygni type profiles, in the latter, the strength of the P-Cygni emission, relative to the depth of the absorption feature, is much larger. This is consistent with the 'annular' spectrum being a sum of pure resonant scattered emission, produced at a radius of 2 to 3 arcseconds, and a P-Cygni feature (having both absorption and emission) produced $< \sim 1.3''$ from the central source, scattered by atmospheric seeing into the annular aperture. Therefore, in order to obtain the true emission spectrum, we have subtracted a multiple of the 'circular' spectrum from the 'annular' spectrum, such that the result has no continuum.

In Figure 5.3 we display, for the R(2) line, a) the 'annular' spectrum, b) the 'circular' spectrum, and c) the 'emission' spectrum. The regions of high telluric opacity (redwards of the line) have been masked. The emission profile is centred at the source velocity (-26 km s^{-1}), and extends roughly 15 km s^{-1} on each side. This is consistent with the expansion velocity of the IRC +10216 envelope derived from millimeter lines. In Figure 5.3d we have plotted the CO J = 2-1, V = 0 line (observed with one of the Owen's Valley Radio Observatory 10.4 m Telescopes). Lastly, we note that Figure 5.3c shows possible evidence of high velocity emission on the blue side extending beyond the expansion velocity of the envelope. The R(2) emission profile provides clear evidence that we have detected emission originating in regions 2 to 3.5 arc-seconds from the center of the envelope. These emission line profiles, however, have not been used in the modelling, because it is computationally simpler to simulate the emission in the 'annular' spectrum by convolving the model brightness distribution for each line with a 'seeing' function.

The high velocity feature beyond the blue edge of the main profile is very interesting. In order to confirm the presence of this feature, we have added together 5 different lines [P(1), R(1), R(2), R(4), and R(6)], selected for being in regions of little or no telluric opacity; the resulting spectrum (Figure 5.4a) clearly shows the high velocity emission. The CO J = 2-1, V = 0 spectrum (dotted) is also plotted; there is no evidence in this line of emission at velocities beyond the expansion velocity. Figure 5.4b shows the sum of 4 lines of ^{13}CO R(12), R(13), R(16), and R(19). The high velocity emission is again present; however, this emission extends smoothly towards lower velocities, unlike the ^{12}CO emission which shows a dip at the expansion velocity. The peak of the ^{13}CO emission is blueshifted with respect to the peak of the J = 2-1 line.

Considered together, the ^{12}CO and ^{13}CO line profiles indicate that the high velocity emission is coming from gas which is closer to the star than that which produces the main emission. In such a scenario, the dip at the expansion velocity of the ^{12}CO profile results from absorption by the cooler 15 km s^{-1} gas. Such absorption is not seen in the ^{13}CO profile, presumably a result of the cool gas being optically thin in this transition. This also makes the ^{13}CO high velocity component quite substantial compared to the normal emission feature, resulting in the shift of the peak of the emission bluewards of the millimeter line. What is hard to understand is why the high velocity emission is not seen beyond the red wing of the normal emission, as would be expected if it was due to a hot expanding shell with a larger expansion velocity than 15 km s^{-1}.

FIGURE CAPTIONS

Figure 5.1. A portion of the observed IRC +10216 spectrum at 4.6 μm. a) the telluric opacity, computed from the lunar spectrum. b) the 'uncorrected' IRC +10216 spectrum observed through an annulus of size 2" - 3.45". c) the spectrum in (b) 'corrected' for telluric opacity.

Figure 5.2. The red half of the observed CO 4.6 μm emission lines, together with the model fits, are shown. (The blue half is contaminated by absorption scattered into the annulus by atmospheric seeing.)

Figure 5.3. The R(2) line from IRC +10216, observed through a) the 'annular' aperture, and b) the 'circular' aperture. In c) is shown the 'emission' profile, generated from the 'annular' and 'circular' profile. In d) the CO J = 2-1, V = 0 millimeter line profile is shown for comparison with the infrared line profile.

Figure 5.4. The average infrared 'emission' line profile (heavy trace) from IRC +10216, in a) CO and b) ^{13}CO. The CO J = 2-1, V = 0 line (light trace) is also shown. Both of the infrared line profile show evidence of unusual high velocity emission in their blue wings beyond the expansion velocity (15 km s^{-1}) of the extended IRC +10216 envelope.

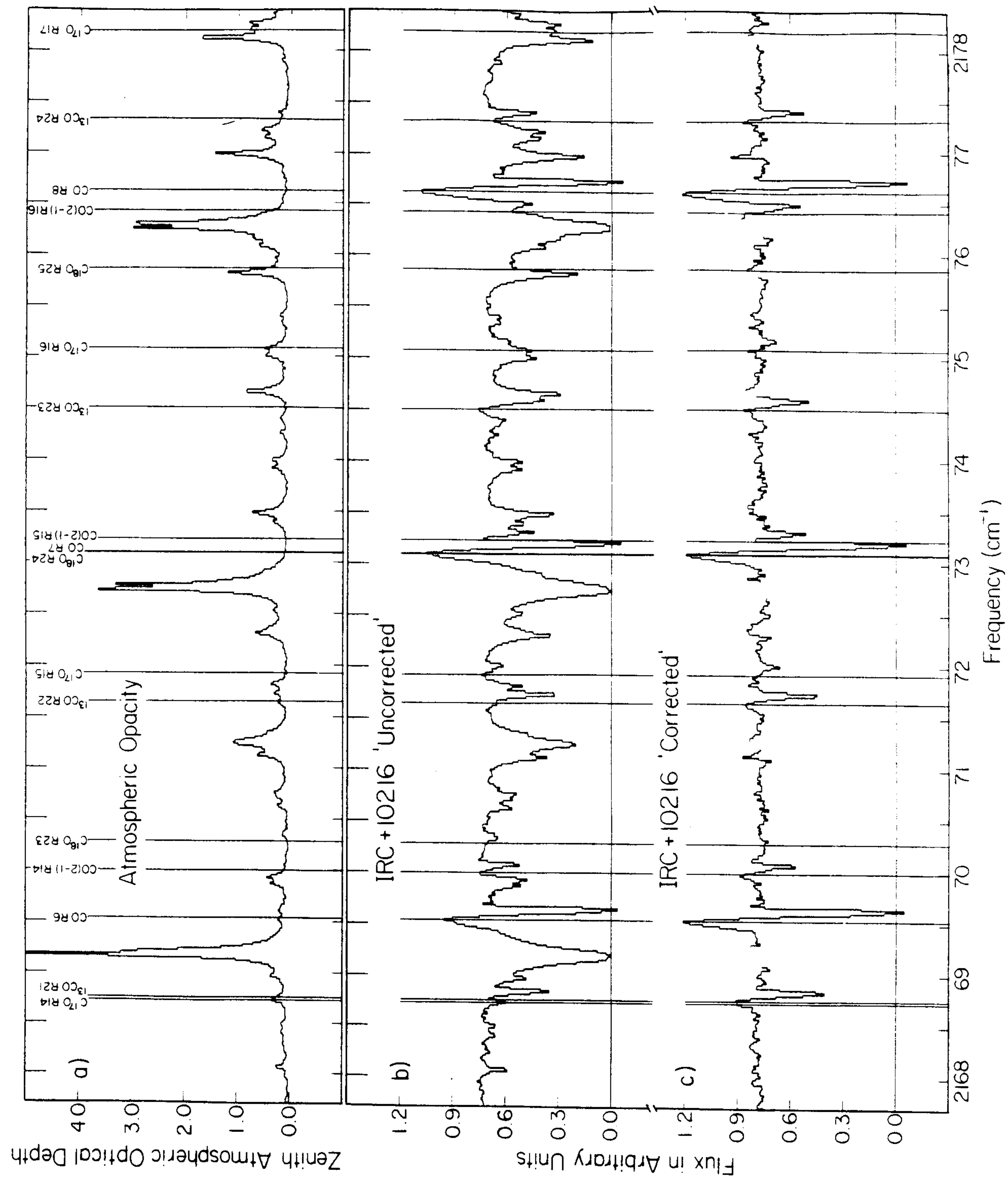
a) Atmospheric Opacity
b) IRC+10216 'Uncorrected'
c) IRC+10216 'Corrected'
Zenith Atmospheric Optical Depth
0.0
1.0
2.0
3.0
4.0
Flux in Arbitrary Units
0.0
0.3
0.6
0.9
1.2
0.0
0.3
0.6
0.9
1.2
2168
69
70
71
72
73
74
75
76
77
2178
Frequency (cm^{-1})
C^{17}O R14
^{13}CO R21
CO R6
CO(2-1) R14
C^{18}O R23
^{13}CO R22
C^{17}O R15
C^{18}O R24
CO R7
CO(2-1) R15
^{13}CO R23
C^{17}O R16
C^{18}O R25
CO(2-1) R16
CO R8
^{13}CO R24
C^{17}O R17

FIGURE 5.1

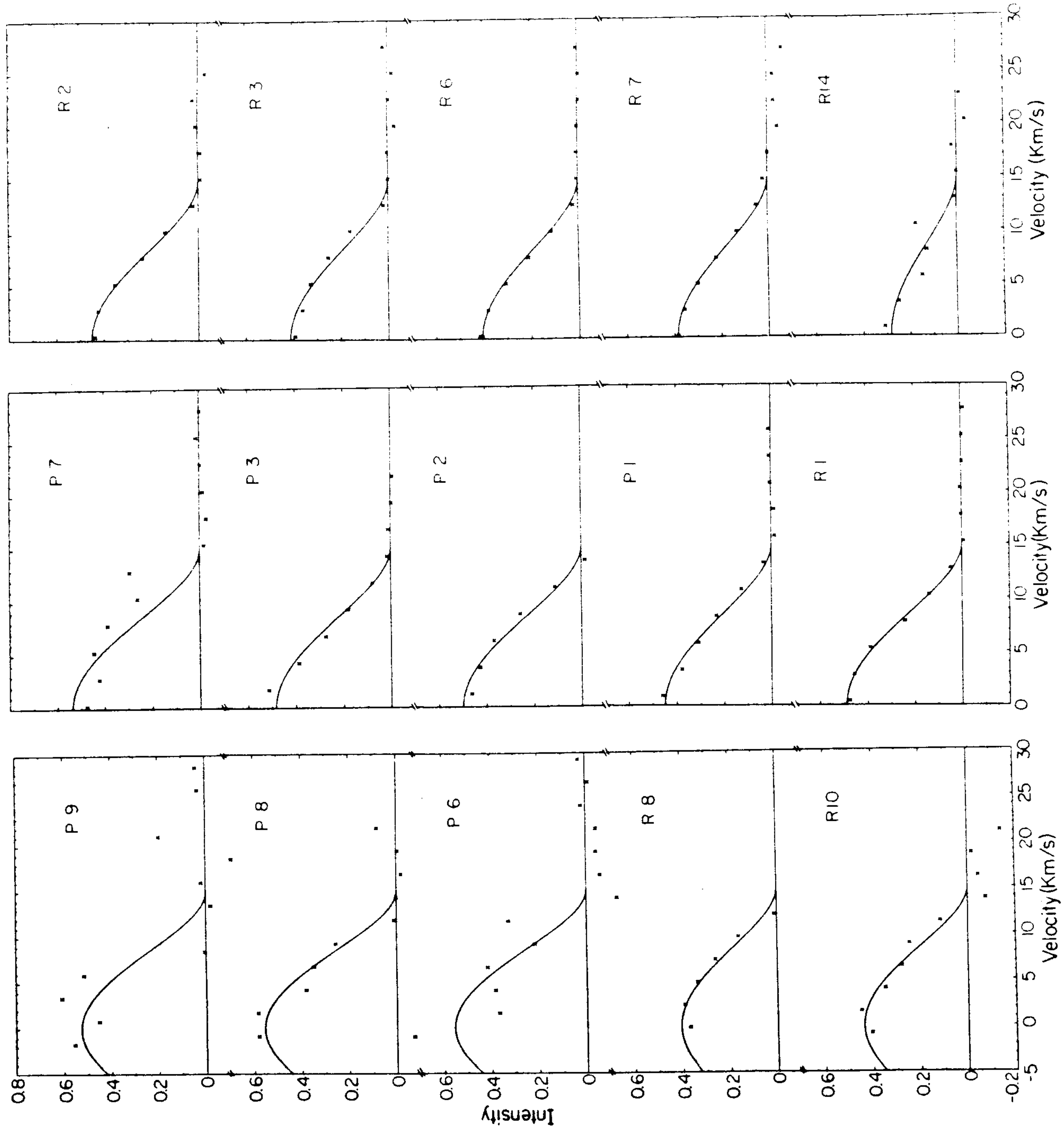
P 9
P 8
P 6
R 8
R10
P 7
P 3
P 2
P I
R I
R 2
R 3
R 6
R 7
R14
Intensity
0.8
0.6
0.4
0.2
0
-0.2
Velocity (Km/s)
-5
0
5
10
15
20
25
30

FIGURE 5.2

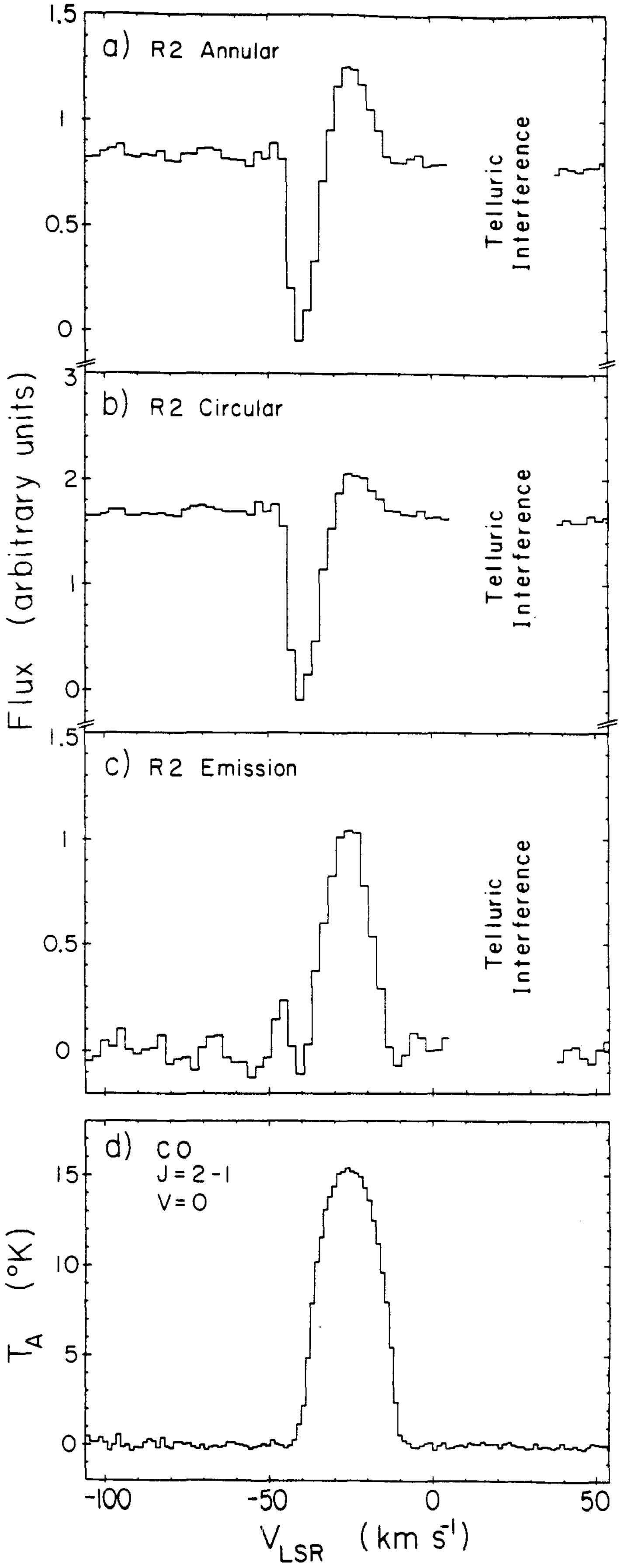
a) R2 Annular
b) R2 Circular
c) R2 Emission
d) CO
J = 2 - 1
V = 0
Telluric Interference
Telluric Interference
Telluric Interference
Flux (arbitrary units)
T_A (°K)
V_{LSR} (km s^{-1})
1.5
1
0.5
0
3
2
1
0
1.5
1
0.5
0
15
10
5
0
-100
-50
0
50

FIGURE 5.3

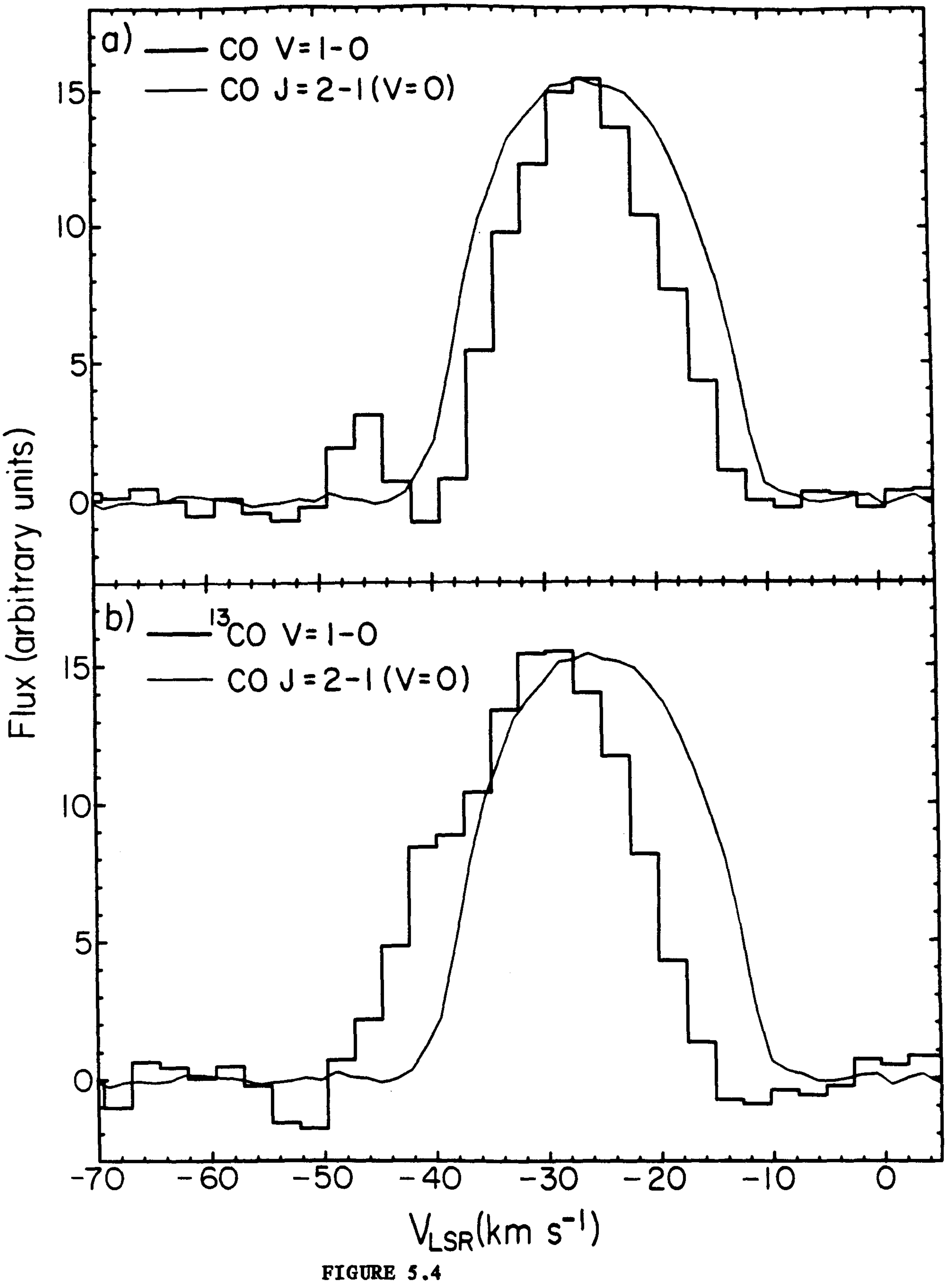
a)
CO V=1-0
CO J=2-1(V=0)
b)
^{13}CO V=1-0
CO J=2-1 (V=0)
Flux (arbitrary units)
15
10
5
0
-70
-60
-50
-40
-30
-20
-10
0
V_{LSR}(km s^{-1})

FIGURE 5.4

CHAPTER 6

INTERPRETATION OF 4.6 MICRON CO EMISSION LINES FROM IRC +10216

6.1. INTRODUCTION

Until recently, no attempt has been made to model vibration-rotation line profiles, mainly because the general calculation of radiative transfer in spherical geometry, incorporating the various physical mechanisms for the excitation of these lines, is very difficult. Keady, Hall, and Ridgway (1984) have presented results from a numerical code using the comoving frame formulation of the radiative transfer problem. However, there is clearly a need for a simple analytical solution which displays the dependence of the emission profiles on the underlying physical conditions.

For the circumstellar shell of IRC +10216, which is characterized by high densities and line opacities in the regions where the lines are produced, simplifying assumptions are possible, which permit an analytic solution. In this chapter, we present an analytical calculation of the emission line profiles, whose observations were given in the previous chapter. Simple formulae for the dependence of the emission intensities on the dust temperature, gas temperature, and velocity are derived. By fitting the predicted line intensities and shapes to observations, we derive a gas temperature characterising the region where the emission is produced. We show that scattering in the earth's atmosphere, and guiding errors, which result in a 'seeing disk,' have to be taken into account while interpreting the observations.

The following physical structure is adopted for the circumstellar shell - a) a constant mass loss rate, b) a constant expansion velocity, and c) a gas kinetic temperature variation with radius parametrized by

$$T_k(r) = T_0 \; [350(\; 2 \times 10^{15}/r^{0.7})] \; K \; . \qquad (6.1)$$

The functional form inside the square brackets has been taken from Kwok et al. (1980) , and represents an empirical fit to the temperature variation derived by Kwan and Hill (1977) (hereafter KH) from consideration of heating and cooling mechanisms in the IRC +10216 shell. The dimensionless constant T_0 in front is used to scale the temperature profile, when fitting our model to the observations.

6.2. EQUATIONS OF RADIATIVE TRANSFER AND STATISTICAL EQUILIBRIUM

The large expansion velocities of circumstellar envelopes (10 to 20 km s^{-1}) compared to the intrinsic line-widths (typically 1 km s^{-1} due to thermal and microturbulent motions in the gas) allows the use of the simplifying Sobolev escape probability method in treating the radiative transfer. This formulation has been extended by Castor (1970) and Lucy (1971) , and Elitzur, Goldreich and Scoville (1976 , hereafter EGS) used the method to model the OH maser lines from circumstellar envelopes. Here we adapt the equations given in EGS to the physical conditions appropriate to the carbon-rich IRC +10216 circumstellar shell. The rotational level populations of the V = 1 vibrational state are calculated in order to determine the emission line profiles.

The equations of statistical equilbrium (Eqn. 11 of EGS) governing n_k, the number density per sublevel of CO molecules in the V,J = 1,k level, may be written as

$$dn_k/dt =$$

$$\sum_{j>k} (g_j/g_k)\, A_{jk}\Big[\, \beta_{jk}[\, n_j - (n_k-n_j)/(e^{h\nu/kT_B}-1)] - D_{jk}(n_k-n_j)\Big]$$

$$+\ C\, g_j[\, n_j - n_k e^{-h\nu/kT_k}]$$

$$-\sum_{j<k} A_{kj}\Big[\, \beta_{kj}[\, n_k - (n_j-n_k)/(e^{h\nu/kT_B}-1)] - D_{kj}(n_j-n_k)\Big]$$

$$+\ C\, g_j[\, n_k - n_j e^{-h\nu/kT_k}] \qquad (6.2)$$

with T_k being the gas kinetic temperature, and T_B being the temperature of the background continuum. The summations are taken over the rotational levels of only the V = 0 and 1 states. The population in higher vibrational levels is negligible, at the temperatures ($\lesssim$300 K) characterising the circumstellar region of interest.

The β's are photon escape probabilities defined by

$$\beta_{ij}(r) = 1/4\pi \int d\Omega\ \beta_{ij}(r,\mu)$$

$$= 1/4\pi \int d\Omega\{\, 1 - \exp[-\tau_{ij}(r,\mu)]\}/\ \tau_{ij}(r,\mu)\ , \qquad (6.3)$$

where $\tau_{ij}(r,\mu) = \tau^{0}_{ij}\ /\ (1 + \mu^2\sigma)$ is the optical depth at an angle $\phi = \cos^{-1}\mu$ to the radius vector. The optical depth is parametrized by the opacity in the direction perpendicular to the radius vector,

$$\tau^{o}_{ij} = (hcr/4\pi V)\ B_{ij}g_{i}(n_{j}-n_{i}),$$

where g_k is the level degeneracy, and B_{ij} is the Einstein B coefficient. The parameter

$\sigma = \left[d(\ln V)/d(\ln r) - 1\right]$, where V is the radial expansion velocity. The D_{ij} terms, described later, are associated with continuum emission from dust grains.

The mean 4.6 μm infrared intensity which excites each vibration-rotation line is produced by thermal emission from warm dust and trapped line photons. The dust emission, as measured by Toombs et al. (1972), can be characterised by a hot, approximately 600 K compact central continuum source of diameter 0.2", and a cooler, extended, optically thin dust shell of diameter 1.0" (Figure 6.1) with a characteristic temperature of 375 K and inverse-square dependence of density on radius. The radial optical depth of this shell at 10 μm is 0.2. Though, in reality the infrared flux is produced by a dust shell with a continously varying temperature and density (and therefore optical depth), the above approximation reproduces reasonably well the lunar occultation data from 2 to 10 μm, and is expected to be adequate in calculating the mean intensities at the frequencies of the vibration-rotation lines. We justify this later (see Appendix) using a more realistic model of the dust source, and showing that it yields the same results.

The contribution to the radiative transition rate associated with photons emitted by the warm dust grains is given by $g_iA_{ij}D_{ij}(n_j-n_i)$. The quantity D_{ij} is the product of $c^2/2h\nu^3$ and the mean intensity in the ij line averaged over the line profile, and may be broken up into two parts: D_s, the contribution from the optically thin shell, and D_c, the contribution from the optically thick core source (see Fig. 6.1). Thus,

$$D_{ij}(r) = D_s(r) + D_c(r), \text{ where}$$

$$D_s(r) = 1/2 \int_{-\mu_s}^{\mu c} d\mu [\, \beta_{ij}(r,\mu) \times \int_{-\mu r}^{\infty} dz' \, \sigma_d(\nu) n_d(r')/(\, e^{h\nu/kT_d} -1)] \qquad (6.4a)$$

and

$$D_c(r) = c^2/2h\nu^3 \left[\, 1/2 \; B_\nu(T_c) \int_{\mu_c}^{1} d\mu \; \beta_{ij}(r,\mu) \,\right] \qquad (6.4b)$$

with $B_\nu(T_c)$ equal to the Planck temperature at T_c, the core temperature. In the above equations, we have ignored the emission from dust in front of the core in view of its low temperature and opacity relative to the core source. The absorption cross section $\sigma_d(\nu)$ is taken to vary inversely as the square of the wavelength near 4.6 μm (Mitchell and Robinson 1980) .

To calculate the dust emission terms, we first evaluate

$$I_1 = \int_{-\mu r}^{\infty} dz' \; \sigma_d(\nu) n_d(r') / (e^{h\nu/kT_d} -1),$$

in order to determine D_s. Integrating along the ray z', the upper and lower limits on z' become z_s and $-z_s$ (Figure 6.1), and we obtain

$$I_1 = r\sigma_d(\nu) n_d(r) \; / \; (e^{h\nu/kT_d} -1)\xi(\mu) \tag{6.5}$$

where

$$\xi(\mu) = 2 \; \tan^{-1}[\; z_s(\mu) \; / \; p(\mu) \;] \; / \; (1-\mu^2)^{1/2} \; .$$

Then

$$D_s(r) = [\; r\sigma_d(\nu) n_d(r) / (e^{h\nu/kT_d} -1)] \; [X(r,\sigma)/\tau^o_{ij}], \tag{6.6}$$

where

$$X(r,\sigma) = 1/2 \; \tau^o_{ij} \int_{-\mu_s}^{\mu c} d\mu \; \beta_{ij}(r,\mu) \; \xi(\mu).$$

The contribution from the core is

$$D_c = [(2 - 3\mu_c + \mu_c^3)/(e^{h\nu/kT_c} -1)] \; / \; 3\tau^o_{ij} \; . \tag{6.7}$$

The above is derived making the approximation that the escape probability $\beta_{ij} = (1 + \mu^2\sigma)/\tau^o_{ij}$ when $\tau^o_{ij} >> 1$. The latter is true for the vibration-rotation lines of CO in IRC +10216 at least out to radii corresponding to a few arcseconds.

Evaluating $D_s(r)$ and $D_c(r)$ from the above expressions, we find that D_c, the contribution to the mean intensity from the 600 K core, is small compared to D_s, the contribution of the 375 K shell. This is because of two factors: first, the solid angle subtended by the 375 K shell is about 20 times larger than that by the 600 K core. Second, and more important, is that $\beta_{ij}(r,\mu)$, the escape probability in the direction of the core, becomes small, if the outflow approaches terminal velocity ($\sigma = -1$). Therefore the radiation from the 600 K core, whose extent is confined to a range of μ very close to 1, is much more severely attenuated than the radiation from the more extended 375 K shell.

The following table shows the D_s to D_c ratio as a function of radius. The effect of finite optical depth has been included in the calculations for this table. For r much larger than the 375 K shell radius, this ratio becomes constant - which is what we expect because then the ratio is proportional to the ratio of the Planck intensity at the Shell temperature to that at the Core temperature, multiplied by the ratio of the solid angles subtended by the shell to that subtended by the core at the radius r. Quantitatively, D_c is always less than 15 % of D_s, and, in the following analytical treatment, we will ignore the contribution of the 600 K core relative to the contribution of the 375 K shell.

r(")	D_s/D_c
1.2	7.9
1.5	7.2
2.0	6.8
2.4	6.6
3.0	6.5
4.0	6.5
5.0	6.4
10.0	6.4
50.0	6.4

The shell contribution, D_s can be written as a product of a radial function

$$D^o(r) = rn_d(r)X(r,\sigma)/G(\sigma), \text{ and a}$$

frequency-dependent function, $E(\nu)G(\sigma)$, where

$$E(\nu) = \sigma_d(\nu)/[\,e^{h\nu/kT_d}-1], \text{ and } G(\sigma) = (1+\sigma/3).$$

Making the substitution $\sigma = -1$, we find that for $r \geq 1.5''$, the function $X(r,-1)$ varies like r^{-3}. The shell contribution decreases with radius as r^{-4} to within 10 % over a factor of 50 in radius. This variation is shown in the table below, which lists $D^o(r)$ (normalised to its value at 2.4") versus $(r/2.4'')^{-4}$.

$(r/2.4'')^{-4}$	$D^{\circ}(r)/D^{\circ}(2.4'')$
16.1	19.2
6.67	7.14
2.08	2.13
1.00	1.00
0.410	0.403
0.129	0.126
5.31×10^{-2}	5.07×10^{-2}
3.32×10^{-3}	3.18×10^{-3}
5.32×10^{-6}	5.07×10^{-6}

6.3. AN APPROXIMATE SOLUTION

The sublevel population n_k is governed simply by the balance between the infrared pump rate from the connected ground state rotational levels, and the spontaneous decay rate from V = 1 back to V = 0. This is because the spontaneous decay rates out of the V = 1 rotational levels are much larger than those for rotational transitions, as well as the collision rates from and to these levels. For example, the Einstein A for the R(0) line is 11.5 s^{-1}, whereas the collision rate for rotational transitions, at a gas density of 10^6 cm^{-3} is typically 10^{-4} s^{-1}. If the vibration-rotation lines are optically thick, the effective radiative decay rate is greatly reduced from the spontaneous rate because of trapping of line photons. A given spontaneous decay photon may be reabsorbed and reemitted many times before it escapes and the net decay rate given by $A_{ij}\beta_{ij}$ varies as $1/\tau^q_{ij}$ for large optical depths. Optical depths of roughly 10^5 would be required to make the effective radiative decay rates as small as the collisional rates for rotational transitions. Since the actual optical depths at densities of 10^6 cm^{-3} are always less than 50, we can therefore neglect the thermalization of vibration-rotation line photons.

In view of the above, the rate equation (Eqn. 6.2) simplifies to

$$dn_k/dt = A_{k+}(\ \beta_{k+}n_k - D_{k+}n'_{k+1}) - A_{k-}(\ \beta_{k-}n_k - D_{k-}n'_{k-1}) \quad (6.8)$$

where $A_{k-}\beta_{k-}$ is the effective radiative decay rate and D_{k-} is the quantity D_{ij}, evaluated for the transition connecting V, J = 0, k-1 to V, J = 1, k [referred to as R(k-1)]; the sublevel population of the former level being given by n'_{k-1}. The terms with + subscripts refer to the transition from V, J = 0, k+1 to V, J = 1, k [referred to as P(k+1)].

Setting $dn_k/dt = 0$, we get

$$n_k = \frac{A_{k+}\ D_{k+}\ n'_{k+1} + A_{k-}\ D_{k-}\ n'_{k-1}}{A_{k+}\ \beta_{k+} + A_{k-}\ \beta_{k-}} \quad (6.9)$$

Substituting the expressions derived for the dust emission terms,

$$A_{k+}D_{k+}n'_{k+1} = G(\sigma)D^{o}(r)E(\nu_{k+})\ A_{k+}n'_{k+1}/[\ (hcr/4\pi V)B_{k+}g_{k}n'_{k+1}].$$

Since $B_{k+} = A_{k+}c^{2}/(2h\nu^{3})$, the above equation simplifies to

$$A_{k+}D_{k+}n'_{k+1} = D^{o}(r)E(\nu_{k+})G(\sigma)g_{k}8\pi V\ \nu_{k+}{}^{3}/(rc^{3}).$$

Similarly

$$A_{k-}D_{k-}n'_{k-1} = D^{o}(r)E(\nu_{k-})G(\sigma)\ g_{k}8\pi V\ \nu_{k-}{}^{3}/(rc^{3}).$$

Since the escape probability $\beta_{k+} = G(\sigma)/[\ (hcr/4\pi V)B_{k+}g_{k}n'_{k+1}]$,

$$A_{k+}\beta_{k+} = G(\sigma)n'_{k+1}g_{k}8\pi V\ \nu_{k+}{}^{3}/(rc^{3}),$$

$$A_{k-}\beta_{k-} = G(\sigma)n'_{k-1}g_{k}8\pi V\ \nu_{k-}{}^{3}/(rc^{3}).$$

Substituting the above in equation (6.9), we get

$$n_{k} = D^{o}(r)\left[E(\nu_{k+}) + E(\nu_{k-})\gamma^{3}\right]\left[\frac{n'_{k-1}\ n'_{k+1}}{n'_{k-1} + n'_{k+1}\gamma^{3}}\right] \qquad (6.10)$$

where $\gamma = \nu_{k-}/\nu_{k+}$. The quantities $E(\nu_{k+})$ and $E(\nu_{k-})$ are found by calculating $E(\nu)$ at the frequencies of the P(k+1) and R(k-1) lines, respectively. In our expression for n_{k} (Eqn. 6.10) the molecular line opacity τ_{ij} has cancelled out. This occurs because, as the opacity goes up and the pump rate from V = 0 to V = 1 decreases (because fewer photons from the infrared source can reach the CO molecules at any radius), the net decay rate also decreases by the same factor due to the increased line trapping.

6.4. THE EMISSION LINE PROFILE

We now make the assumption that the rotational level populations in the ground vibrational state are in L.T.E. at the gas kinetic temperature T_k. The assumption of L.T.E. is good if the collisional rates amongst the V = 0 rotational levels are large compared to radiative excitation and de-excitation rates for these levels. Rates for radiative transitions amongst the rotational levels are considerably smaller than collisional rates for CO for a wide range of gas densities because of its anomalously small dipole moment. The collisional rates are also much larger than the radiative excitation rates due to infrared absorption.

The source functions for these lines can be calculated from equation (6.10):

$$S_{k+}(r) = (8\pi h\nu_{k+}^{3}/c^{3})\; D^{\circ}(r)\left[\frac{E(\nu_{k+}) + E(\nu_{k-})\gamma^{3}}{1 + H(k)\gamma^{3}}\right] , \qquad (6.11a)$$

$$S_{k-}(r) = (8\pi h\nu_{k-}^{3}/c^{3})\; D^{\circ}(r)\left[\frac{E(\nu_{k+}) + E(\nu_{k-})\gamma^{3}}{1/H(k) + \gamma^{3}}\right] , \qquad (6.11b)$$

where $H(k) = \exp\{ - \frac{2hB}{kT_k(r)}(2k+1)\}$ and B is the rotational constant of the ground vibrational state.

The emergent intensity $I(v_p,p)$ towards the observer, which is a function of v_p, the velocity w.r.t. the stellar velocity, and p, the impact parameter (Figure 6.1), is related to the source function S(r), through the equation

$$I(v_p,p) = (c/4\pi)\ S(r)\ \left[1 - e^{-\tau(v_p,p)}\right] \tag{6.12}$$

where $r = p\ /\ (1 - \{v_p/V\}^2)^{1/2}$. We have assumed that the large velocity gradient present in the tangential direction allows the line photons to escape after traversing a small length

$$\delta z = p\ \Delta V\ /\ [V\ (\ 1 - \{v_p/V\}^2)^{3/2}]\ ,$$

where ΔV is the intrinsic line-width.

The source function S(r) can be assumed to be constant over this length. For large tangential optical depths, i.e., $\tau^{o}_{ij} >> 1$, the exponential term in the equation (6.12) for I can be neglected.

Writing $D^{o}(r) = Ar^{-4}$ where A is a constant, we get

$$I_{k+}(v_p, p) = (A/p^4)\ (2h\nu_{k+}{}^3/c^2)\ (1 - \{v_p/V\}^2)^2$$

$$\times \left[\frac{\sigma_d(\nu_{k+})/\{e^{h\nu_{k+}/kT_d} - 1\} + \gamma^3 \sigma_d(\nu_{k-})/\{e^{h\nu_{k-}/kT_d} - 1\}}{1 + \gamma^3 \exp\{ - \frac{2hB}{kT_k(r)}(2k+1)\}} \right] \qquad (6.13a)$$

$$I_{k-}(v_p, p) = (A/p^4)\ (2h\nu_{k-}{}^3/c^2)\ (1 - \{v_p/V\}^2)^2$$

$$\times \left[\frac{\sigma_d(\nu_{k+})/\{e^{h\nu_{k+}/kT_d} - 1\} + \gamma^3 \sigma_d(\nu_{k-})/\{e^{h\nu_{k-}/kT_d} - 1\}}{\exp\{ \frac{2hB}{kT_k(r)}(2k+1)\} + \gamma^3} \right] \qquad (6.13b)$$

The above expressions are valid as long as the tangential optical depths in the vibration-rotation lines are much larger than one, and the gas densities remain high enough to maintain rotational L.T.E. in the ground state.

The dominant variation of intensity with velocity v_p is given by the $(1 - \{v_p/V\}^2)^2$ factor, with a weaker variation arising from the dependence of the kinetic temperature on radius (since for a given p, a larger v_p occurs at a larger radius). However, this variation is quite small compared to the latter, because the kinetic temperature falls much more slowly with radius ($\sim r^{-0.7}$) than the mean intensity due to dust emission ($\sim r^{-4}$).

The ratio of the emergent intensity of the R(k-1) line to the P(k+1) line is given by

$$\gamma^3 \, H(k) = (\nu_{k-}/\nu_{k+})^3 \exp\{ - \frac{2hB}{kT_k(r)}(2k+1)\} \quad . \qquad (6.14)$$

The above result is actually quite general, and holds as long as n_k is small compared to n'_{k+1} and n'_{k-1}, and the tangential optical depths remain larger than 1. This is shown in the following derivation:

$$S_{k-}(r) = (8\pi h\nu_{k-}^3/c^3) \; n_k/(n'_{k-1} - n_k)$$

$$S_{k+}(r) = (8\pi h\nu_{k+}^3/c^3) \; n_k/(n'_{k+1} - n_k) \; .$$

Neglecting n_k in comparison to n'_{k-1} and n'_{k+1}, and substituting the above expressions in the equation for the emergent intensity (6.12), with τ set >>1, we obtain

$$I_{k-}/I_{k+} = (\nu_{k-}/\nu_{k+})^3 \; (n'_{k-1}/n'_{k+1}) \; ,$$

which is identical to equation (6.14). Thus the relative intensities of P and R lines with the same upper level are a model-independent measure of the gas temperature despite the fact that the lines are excited by the dust continuum.

The line intensity increases with J along the P branch and decreases with J along the R branch. The variation is a sensitive measure of the kinetic temperature as can be seen from a plot of the logarithmic intensity versus J for temperatures of 100, 200 and equations 6.13a and 6.13b, with the $\left[1 - e^{-\tau(v_p,p)}\right]$ factor set equal to 1). The features of this plot are simply explained if we assume that the V = 1 rotational level populations are characterised by the same rotational temperature T_k as the V = 0 levels (shown later). The ratio of P(J) to R(J) intensity is given by

$$\frac{I_{P(J)}}{I_{R(J)}} = \frac{S_{P(J)}}{S_{R(J)}} = (\nu_P/\nu_R)^3 \; \frac{n_{J-1}/n'_J}{n_{J+1}/n'_J}$$

$$= (\nu_P/\nu_R)^3 \; \exp\{\frac{2hb}{kT_k(r)}(2J+1)\}$$

where b is the rotational constant of the V = 1 levels. Thus, a) for a constant T_k, as J increases, the P(J) to R(J) ratio gets larger, and b) for a given J, as T_k increases, the P(J) to R(J) ratio gets smaller, as shown in the figure. The P(J+1)/P(J) intensity ratio is given by

$$(\nu_{P(J+1)}/\nu_{P(J)})^3 \; \frac{n_J/n'_{J+1}}{n_{J-1}/n'_J} = (\nu_{P(J+1)}/\nu_{P(J)})^3 \; \exp\{\frac{2hB}{kT_k(r)}\},$$

where we have assumed b = B. Similarly, the R(J+1)/R(J) ratio is given by

$$(\nu_{R(J+1)}/\nu_{R(J)})^3 \; \exp\{-\frac{2hB}{kT_k(r)}\} .$$

These expressions explain the increase of intensity with J along the P branch, and decrease with J along the R branch.

For the special case k = 0, there is only one vibration-rotation transition possible i.e., P(1); therefore, the equations for n_0, S_0 and $I_0(v_p,p)$ simplify to

$$n_0 = D^{\bullet}(r)\ [\ \sigma_d(\nu_0)/\{e^{h\nu_0/kT_d}-1\}\ ]\ n'_1, \qquad (6.15a)$$

$$S_0(r) = (8\pi h\nu_0{}^3/c^3)\ D^{\bullet}(r)\ [\ \sigma_d(\nu_0)/\{e^{h\nu_0/kT_d}-1\}\ ], \qquad (6.15b)$$

and

$$I_0(v_p,p) = (A/p^4)\ (2h\nu_0{}^3/c^2)\ (1 - \{v_p/V\}^2)^2$$
$$\times\ [\ \sigma_d(\nu_0)/\{e^{h\nu_0/kT_d}-1\}\ ] \qquad (6.15c)$$

where ν_0 is the frequency of the P(1) line.

This is a very interesting result because it shows that the observed intensity of the P(1) line is directly related to the dust temperature and density and is independent of the gas temperature. Since the V,J = 1,0 level is connected only to the the V,J = 0,1 level, its population is proportional to that of the latter. Therefore, changes in the kinetic temperature do not affect the ratio of the populations in these two levels. Hence the excitation temperature, source function and emergent intensity of the P(1) line are all independent of changes in the gas temperature.

Using the equation for n_k, we calculate the excitation temperature(s) for the V = 1 rotational levels. Figure 6.3 displays these as a function of radius in the circumstellar shell for 2 values of T_0, a) T_0 = 1, and b) T_0 = 2, characterizing the kinetic temperature which is also plotted. It can be seen that the $V = 1$ rotational ladder is nearly thermalised at the same temperature as the $V = 0$ ladder, except for the $J = 1-0$ transition, whose excitation temperature is higher than T_k for $T_k < \sim 350$ K, and less than T_k for $T_k > \sim 350$ K. This result has important consequences for the detailed model of Keady, Hall, and Ridgway (1984), who have assumed rotational L.T.E. in the $V = 0$, 1 and 2 vibrational levels.

The emergent intensity falls very quickly as the line of sight moves away from the central infrared source. Figure 6.4 shows the variation of the predicted intensity of selected P and R branch lines with radius. The intensity points fall on or near the straight line, which represents a r^{-4} variation. Deviations from the straight line occur at larger radii because of the dependence of the function H (equation 6.13) on temperature, which also decreases with radius. The intensity variation for $T_0 = 1$ (Figure 6.4a) and $T_0 = 2$ (Figure 6.4b) shows that, for the latter, the deviation from the straight line is smaller as expected, because the variation in H is smaller at higher temperatures.

6.5. CONVOLUTION WITH 'SEEING' FUNCTION

The analysis described above allows us to calculate the emergent line profiles from the circumstellar shell at a given angular distance from the center of the star. However, one cannot compare these directly with the observations, because scattering, due to the earth's atmosphere, and guiding errors allow some emission from regions outside the observing annulus area to get through the annulus and be detected. The observed emission line intensity is therefore a convolution of the emission line intensity as a function of radius, with an 'effective' seeing disk due to the atmosphere, and guiding errors.

To estimate how significant the above effect is, we calculate the relative contribution to the total flux passing through our annulus from 'illuminating' circles of different radii concentric with the observing annulus, in the presence of a Gaussian seeing disk. The total flux emitted by each circle is taken to be proportional to its length $2\pi r$ times the brightness, which varies as r^{-4}, in accordance with the results derived in the previous section.

Figure 6.5 shows the relative contribution of different radii to the flux observed in the annulus (inner radius 2″, outer radius 3.45″) with various seeing conditions. For a 1″ seeing disk at 4.6 μm, the observed emission is weighted strongest by gas at 2″, though there is significant contribution from radii as small as 1.4″. A slightly worse seeing (1.3″) results in a much larger contribution to the observed light by emission from gas quite close to the star. With a 1.5″ seeing, the observed emission is dominated by gas less than 0.5″ away from the centre. Taking a $\lambda^{-0.2}$ dependence of seeing disk size (Woolf 1982, Boyd 1978), a 1″ seeing in the visual (0.5μm) corresponds to 0.64″ seeing at 4.6 μm. Therefore, only for visual seeing better than 2″ is there significant contribution to the emission from an envelope radius of 2″. For a visual seeing of 2.5″, the observed emission is dominated by gas very close to the star, and an annular aperture is useless in masking out the central infrared source.

In order to calculate the emission line intensities in the presence of atmospheric scattering, we have calculated the falloff of emission line intensity with radius, and then convolved it with a Gaussian seeing profile, whose size is dictated by our estimates of the seeing during the observing period. The convolution of model emission line brightness distribution with the seeing disk, followed by an integration over the area of the annulus, then yields emission line intensities which can be compared with the observations. The above procedure is carried out for several values of T_0 until a 'best fit' value is obtained.

6.6. MODEL FITS

The predictions (for different values of T_0) and the data (Nov 11) are shown together in Figure 6.6. We have taken a mass loss rate of 9 x 10^{-5} $M_{\odot}$ yr^{-1} (Kwan and Linke 1982) for our adopted distance of 300 pc (Herbig and Zappala 1970) to IRC +10216. Figures 6.6a and 6.6b display the results for seeing disks at 4.6 μm of 1" and 1.3", equivalent to visual seeing disks of 1.6" and 2.0", respectively. The curves of relative line intensities for different values of T_0 are labelled by the kinetic temperature at a radial distance of 2". The P(1) point, which is independent of the kinetic temperature, coincides for different models. The data are scaled by a constant multiple, in order to make the P(1) data point coincide with the models. A weighted average of the residuals for all the data points is computed, and the value of T_0 which minimizes this is taken as the 'best fit' value.

Figure 6.6 shows that T_0 = 1, which represents the KH temperature profile, is significantly lower than that required by the data. T_0 = 3 is too high, and a value near 2 seems appropriate. The data from the Nov 12 scans are scantier and more noisy, but are consistent with a value of 2 for T_0. The KH model assumes a distance of 200 pc to IRC +10216; however their calculations show that the temperature distribution as a function of angular displacement does not vary significantly for moderate variations in the assumed distance. The [CO]/[H_2] abundance ratio (hereafter referred to as 'f') adopted in the above model was 3 x

10^{-4}, lower than the Kwan and Linke (1982) value of 6×10^{-4} (uncertain by 30 %). However, our data are better fitted with the lower value of the abundance ratio; the residual after subtracting the data from the model fit for $f = 6 \times 10^{-4}$ is 1.5 times larger than that for the lower value. In any case, the average slope of the model curve does not change significantly for variations in the abundance ratio between the two values mentioned above, and the value of T_0 we have obtained is fairly insensitive to the abundance ratio. Therefore, we conclude that the temperature derived from our observations is definitely higher than the extrapolation of the KH temperature curve.

For the adopted mass loss rate of 9×10^{-5} $M_{\odot}$ yr^{-1}, and $[CO]/[H_2]$ ratio of 3×10^{-4}, the lines remain quite optically thick until J values of about 10. Except for the R(14) line we do not have data for high J lines. Therefore, our analysis is not very sensitive to increases in the mass loss rate. Figure 6.7 shows models with three different values of the mass loss rate (with $T_0 = 2$, and 4.6 μm seeing of 1.0"). The fits for rates of 6.7×10^{-5} and 11.2×10^{-5} $M_{\odot}$ yr^{-1} (0.75 and 1.25 times the nominal rate of 9×10^{-5} $M_{\odot}$ yr^{-1}) are equally good, and only marginally worse than that for 9×10^{-5} $M_{\odot}$ yr^{-1} (Figure 6.6a); however, the fit for 4.5×10^{-5} $M_{\odot}$ yr^{-1} is significantly poorer. In this model the tangential optical depths τ^{o} for the P(1) and R(0) line, at radii $\gtrsim$ ~ 2", are ~ 1.5 or lower, whereas the higher J lines still have τ^{o} ~ 3.0 or larger, resulting in relatively large changes in the predicted intensity from P(1) to $P(J \geq 2)$, and from R(0) to $R(J \geq 1)$, as compared to the data. Models with 1.3″ seeing yield similar results. We set a firm lower limit of 5.8×10^{-5} ($3 \times 10^{-4}/f$) $M_{\odot}$ yr^{-1} to the mass loss rate.

6.7. DISCUSSION

In solving the energy balance equation to derive $T_k(r)$, KH assume an initial gas temperature of 350 K at 2×10^{15} cm. In their model the gas temperature in the (>10″) outer parts of the envelope, where most of the millimeter line emission occurs, is insensitive to the initial temperature assumed at 2×10^{15} cm (0.7″). For example, two models with initial kinetic temperatures which differed by 40 % resulted in temperatures in the outer envelope differing by less than 4 % (Kwan 1984, private communication). This is because cooling due to CO rotational emission becomes effective only at the low temperatures in the outer envelope. Theoretically, one could start the model calculations at radii corresponding to angular scales less than 2″; however, the level of uncertainty in the model parameters increases significantly. The parameter Q, which is the momentum transfer efficiency factor averaged over the spectral energy distribution of the continuum, is taken to be constant with radius. However, Q depends on radius, since the dust grains constantly modify the emergent energy distribution, and may vary significantly in the inner regions of the envelope.

APPENDIX

CALCULATING THE MEAN INTENSITY IN A DUST ENVELOPE IN THE PRESENCE OF MOLECULAR LINE OPACITY

In Chapter 6 we assumed a very simplified model of the dust envelope in IRC +10216 for calculating the mean (angle-averaged, velocity averaged) continuum intensity due to dust in the presence of molecular line opacity. The important results from this model were i) the mean intensity decreased as the fourth power of the radius in the envelope and ii) a single dust temperature of 375 K described the frequency dependence of the mean intensity. Here we assume a dust envelope with a continuously varying temperature and density, and derive the same result. The temperature in the dust shell is taken to be $T_d(r)$ = constant x $r^{-0.4}$ (EGS), and the dust number density $n_d(r)$ = constant x r^{-2}. The contribution to the radiative transition rate between levels i and j due to photons emitted by the warm dust grains is given by $g_i A_{ij} D_{ij} (n_j - n_i)$, with

$$D_{ij}(r) = 1/2 \int_{-1}^{1} d\mu \left[\beta_{ij}(r,\mu) \int_{-\mu r}^{\infty} D(r',\nu) dz' \right]$$

$$D(r',\nu) = \left[\sigma_d(\nu) n_d(r') \;/\; (e^{h\nu/kT_d(r)} - 1) \right] \exp\{-\tau(z')\}$$

where

$$\tau(z') = \int_{-\mu r}^{z'} \sigma d(\nu) n d(r'') dz''$$

is the dust optical depth from the point (r',z') to (r,z). The dust density $n_d(r)$ is taken equal to $K_d r^{-2}$, where K_d is evaluated by taking the total radial optical depth at 4.6 μm from infinity into $3R_*$ to be 2.3 (Keady 1982). To evaluate

$$I_1(r,\mu) = \int_{-\mu r}^{\infty} D(r',\nu)\,dz'$$

we make the substitutions

$$y = z'/r,$$

$$\eta = p/r = (1-\mu^2)^{1/2},$$

$$f(y) = (y^2 + \eta^2)^{0.4}, \text{ and}$$

$$g(y) = \exp\{-\tau(z')\} \;/\; (y^2 + \eta^2). \text{ Then}$$

$$I_1(r,\mu) = [\sigma_d(\nu)K_d(r)/r] \int_{-\mu}^{\infty} dy\; g(y)\; \exp\{-A\; f(y)\},$$

where $A = h\nu/kT_d(r)$. Since $h\nu/k \sim 3100$ K at a wavelength of 4.6 μm, and $T_d(r)$ is typically a few hundred degrees, $A \gg 1$. Therefore, we can evaluate $I_1(r,\mu)$ using the method of steepest descent, obtaining

$$I_1(r,\mu) = [\sigma_d(\nu)K_d(r)/p]\; \exp\{-\; A(p)\}\; \{5\pi/A(p)\}^{1/2}$$

$$\times\; \exp\{\; -\; [\sigma_d(\nu)K_d(r)/p]\; \sin^{-1}\mu\}.$$

This expression is physically reasonable because it says that the dominant contribution to the intensity at the point r from dust comes from the regions closest to the star, where the dust is hottest, which is expected because of the exponential dependence of the Planck intensity on temperature. The above expression is valid for μ greater than zero. Since the dominant contribution to $D_{ij}(r)$ comes from directions towards the star, we can ignore the contribution from directions where $\mu < 0$. Writing

$$D_{ij}(r) = 1/2 \int_0^1 d\mu \, [\, \beta_{ij}(r,\mu) \, I_1(r,\mu)$$

and substituting the expression for I_1 (with ν = 2150 cm^{-1}), we integrate the above integral numerically. The results of this calculation are presented in the following table, with the dust continuum intensity at r (normalised to that at 1") Column 2, and r^{-4} in Column 3.

r(")	D(r)/D(1")	r^{-4}
0.08	6.74×10^3	2.44×10^4
0.10	3.79×10^3	1.00×10^4
0.20	4.93×10^2	6.25×10^2
0.30	1.22×10^2	1.23×10^2
0.40	42.0	29.1
0.50	17.5	16.0
0.60	8.43	7.72
0.80	2.56	2.44
1.0	1.0	1.0
1.2	4.65×10^{-1}	4.82×10^{-1}
1.5	1.82×10^{-1}	1.97×10^{-1}
1.75	9.59×10^{-2}	1.06×10^{-1}
2.0	5.51×10^{-2}	6.25×10^{-2}
2.5	2.20×10^{-2}	2.56×10^{-2}
3.0	1.05×10^{-2}	1.23×10^{-2}
3.5	5.61×10^{-3}	6.66×10^{-3}
4.0	3.27×10^{-3}	3.91×10^{-3}
5.0	1.33×10^{-3}	1.60×10^{-3}

The good agreement between the values in Column 2 and Column 3 shows that the continuum intensity due to dust emission decreases inversely as the fourth power of the radius. For $r < 0.2''$ the intensity varies less steeply than r^{-4}, in accord with the continuum optical depth exceeding unity at these radii. The latter agrees with Toombs' representation, which includes a 600 K optically thick core of radius 0.22" in the IRC +10216 infrared source.

Next we evaluate $D_{ij}(r)$ at three different frequencies 2100 (D_{2100}), 2150 (D_{2150}) and 2200 cm^{-1} (D_{2200}).

r(")	D_{2100}/D_{2150}	D_{2200}/D_{2150}
0.2	1.171	0.854
0.3	1.195	0.838
0.4	1.211	0.827
0.5	1.221	0.822
1.0	1.245	0.809
1.5	1.246	0.806
2.0	1.245	0.807
2.5	1.242	0.807
3.0	1.242	0.808
3.5	1.241	0.809
4.0	1.241	0.809

In the simple model the dependence of the dust emission on the frequency ν is given by $E(\nu) = \sigma_d(\nu)/[e^{h\nu/kT_d}-1]$ with a constant (with radius) $T_d = 375$ K. Defining E_{2100}, E_{2150} and E_{2200} as the values of $E(\nu)$ at 2100, 2150 and 2200 cm^{-1}, we obtain $E_{2100}/E_{2150} = 1.16$ and $E_{2200}/E_{2150} = 0.86$, in reasonable agreement with the values of 1.24 and 0.81 for D_{2100}/D_{2150} and D_{2200}/D_{2150}, respectively. Thus we conclude that the simple Toombs' representation of the infrared source, adopted in our analysis, gives an adequate representation of both the radial and the frequency dependence of the continuum intensity due to thermal dust emission.

FIGURE CAPTIONS

Figure 6.1. The adopted infrared source structure of IRC +10216.

Figure 6.2. The variation of model emergent intensity of CO vibration-rotation lines as a function of J, the angular momentum of the lower state, for three values of the kinetic temperature.

Figure 6.3. The variation of the model excitation temperature in the V = 1 rotational ladder as a function of radius in the IRC +10216 envelope, for kinetic temperature characterised by a) $T_0 = 1$, and b) $T_0 = 2$. The adopted variation of the kinetic temperature is also plotted. The excitation temperature of the J = 1-0 transition (filled circles) is significantly different from the excitation temperature of the higher transitions.

Figure 6.4. The variation of model emergent intensity of CO vibration-rotation lines as a function of radius in the IRC +10216 envelope, for kinetic temperature characterised by a) $T_0 = 1$, and b) $T_0 = 2$. The straight line represents a r^{-4} variation.

Figure 6.5. The relative flux in an annulus of inner radius 2″, outer radius 3.45″, from different radii for a r^{-4} brightness distribution for seeing disks (at 4.6 μm) of 1.0, 1.3 and 1.5″. The maximum flux in each curve is normalised to unity.

Figure 6.6. The model emergent intensities of CO vibration-rotation lines (P and R branches), and the observations are shown as a function of J, for three different radial kinetic temperature curves. Different models are labelled by the kinetic temperature at 2″, and have been scaled to make the predicted P(1) intensity equal to the observed. Model fits are shown for two seeing disk sizes (at 4.6 μm), namely a) 1.0″ and, b) 1.3″.

Figure 6.7. The model emergent intensities of CO vibration-rotation lines (P and R branches), and the observations are shown as a function of J, for three different mass loss rates. $T_0 = 2$ for the radial kinetic temperature variation, and the 4.6 μm seeing is 1.0″. Models have been scaled to make the predicted P(1) intensity equal to the observed.

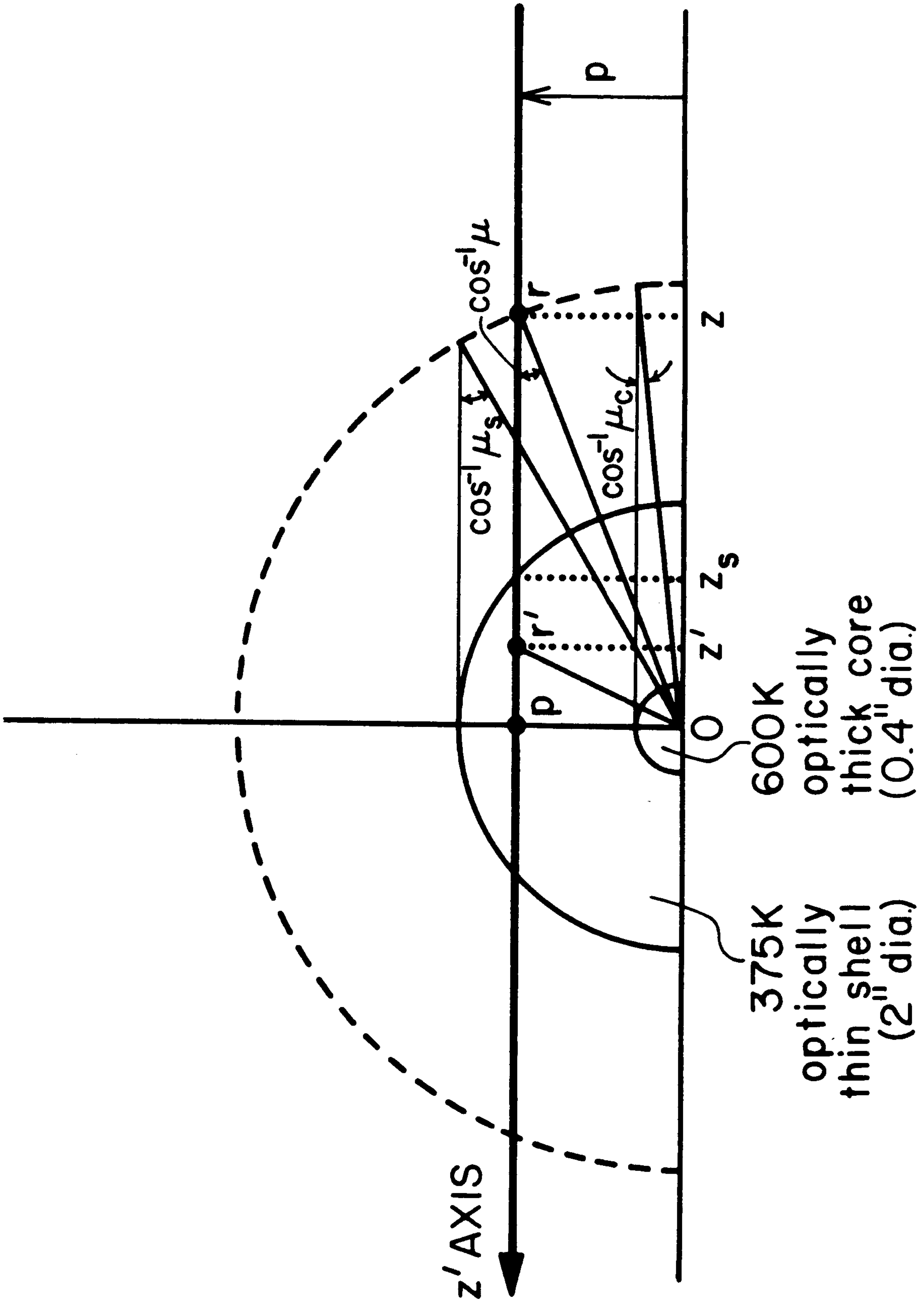
p
cos$^{-1}\mu$
r
z
cos$^{-1}\mu_s$
cos$^{-1}\mu_c$
z$_s$
r'
z'
p
O
600K optically thick core (0.4" dia.)
375K optically thin shell (2" dia.)
z' AXIS

FIGURE 6.1

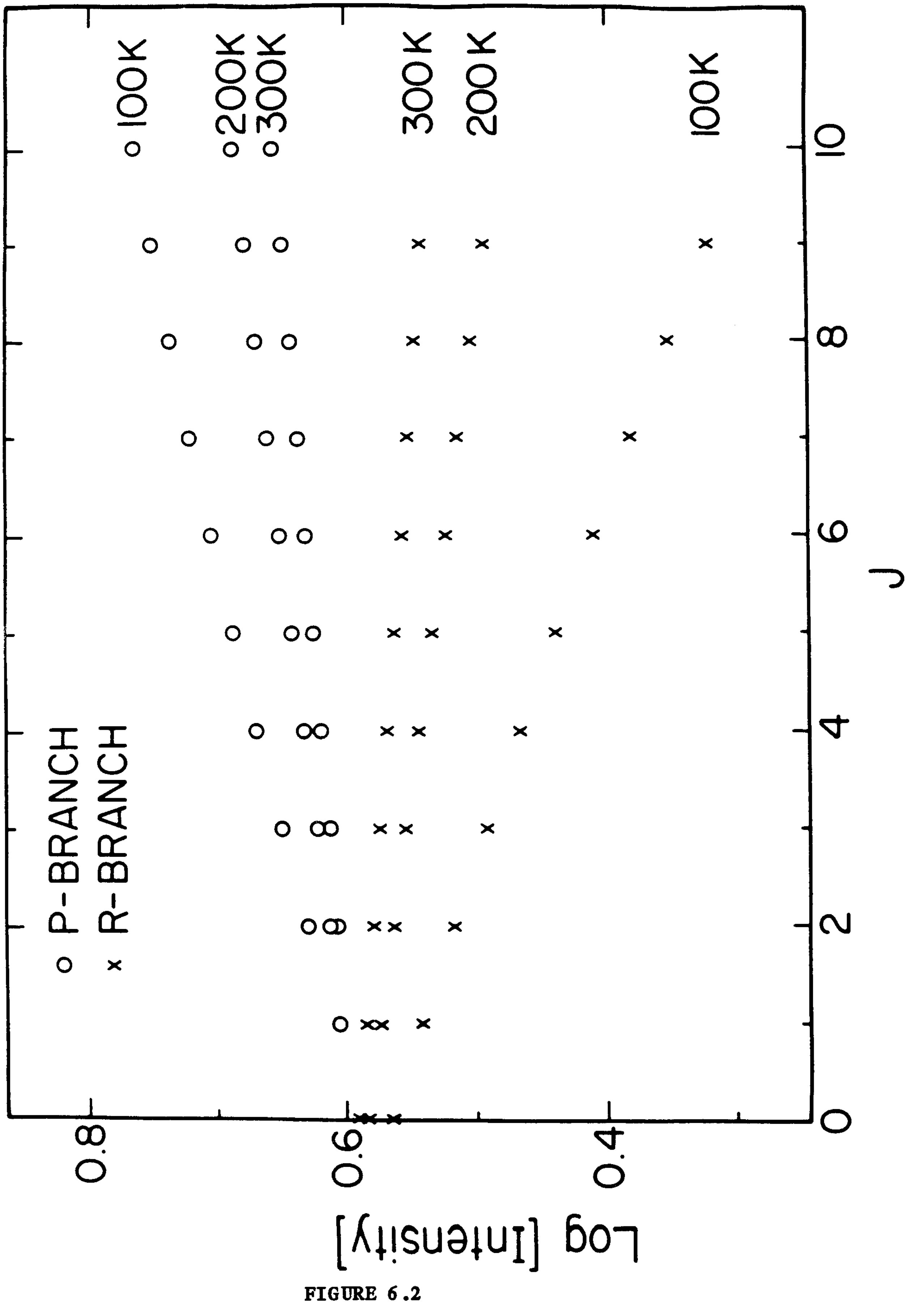
○ P-BRANCH
× R-BRANCH
100K
200K
300K
300K
200K
100K
0.8
0.6
0.4
0
2
4
6
8
10
J
Log [Intensity]

FIGURE 6.2

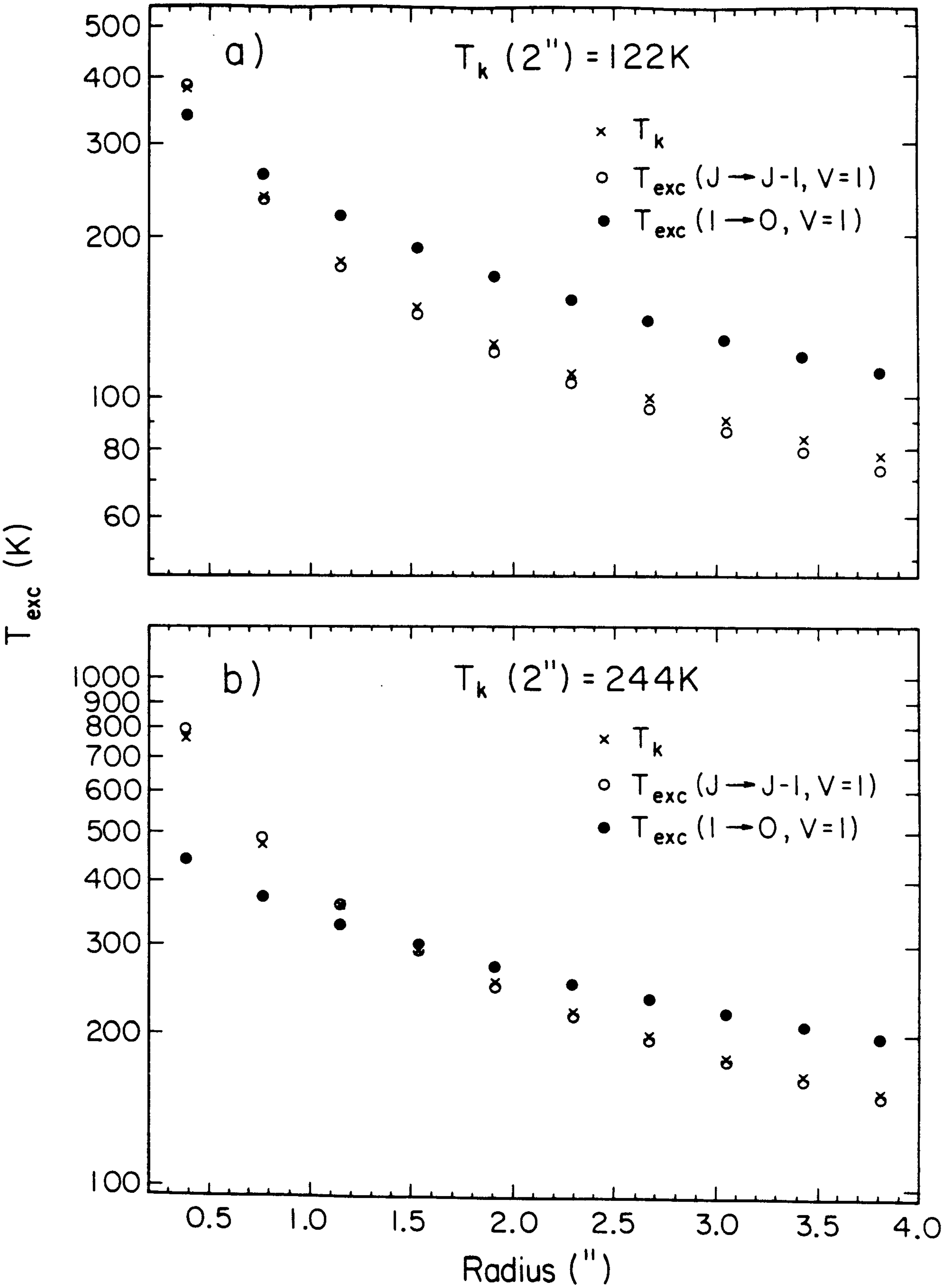
a)
T_k (2") = 122K
× T_k
○ T_{exc} (J → J-1, V=1)
● T_{exc} (1 → 0, V=1)
500
400
300
200
100
80
60
b)
T_k (2") = 244K
× T_k
○ T_{exc} (J → J-1, V=1)
● T_{exc} (1 → 0, V=1)
1000
900
800
700
600
500
400
300
200
100
T_{exc} (K)
0.5
1.0
1.5
2.0
2.5
3.0
3.5
4.0
Radius (")

FIGURE 6.3

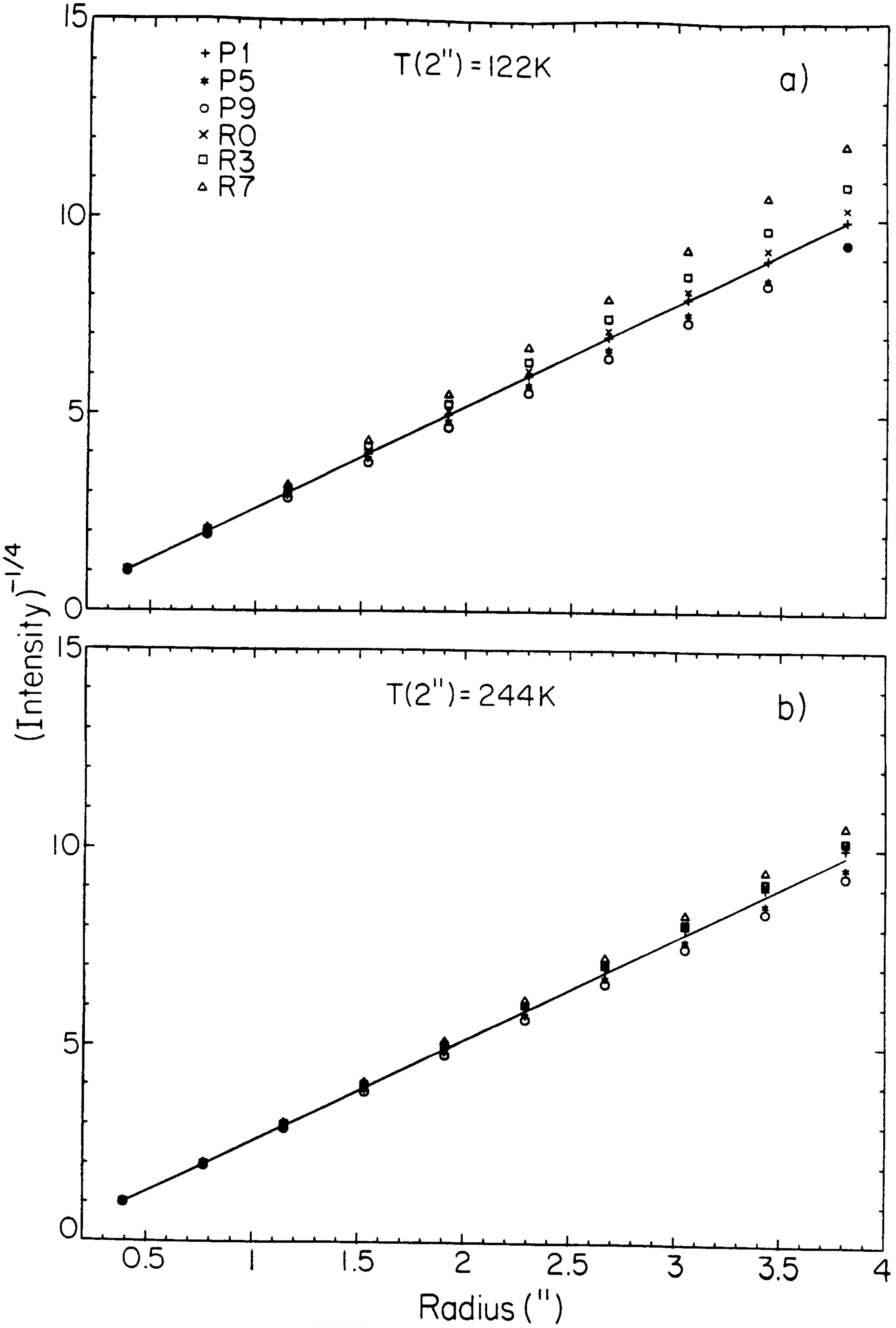
+ P1
* P5
○ P9
× R0
□ R3
△ R7
T(2") = 122K
a)
T(2") = 244K
b)
(Intensity)$^{-1/4}$
0
5
10
15
Radius (")
0.5
1
1.5
2
2.5
3
3.5
4

FIGURE 6.4

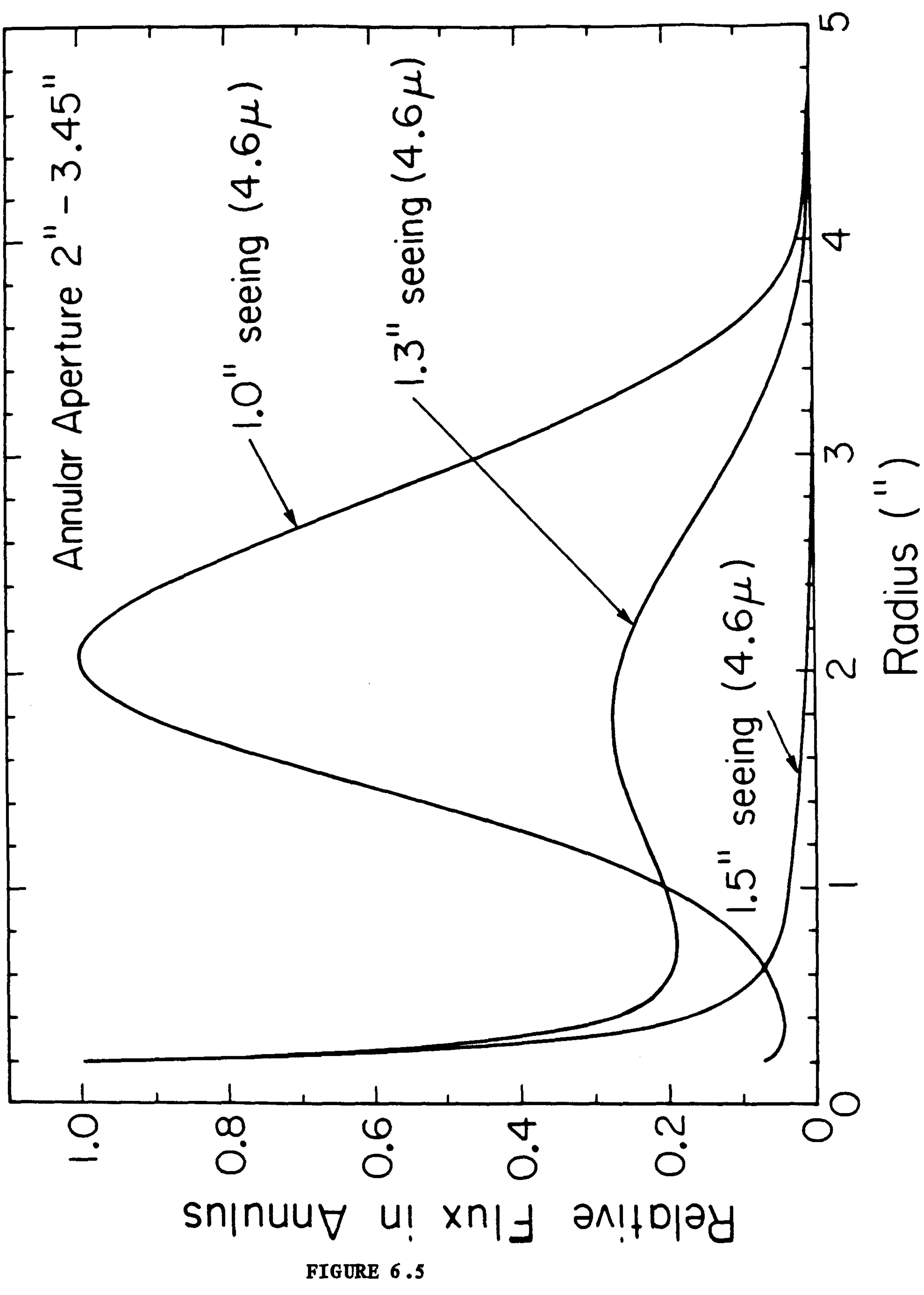
Annular Aperture 2" - 3.45"
1.0" seeing (4.6μ)
1.3" seeing (4.6μ)
1.5" seeing (4.6μ)
Relative Flux in Annulus
Radius (")
0
0.2
0.4
0.6
0.8
1.0
0
1
2
3
4
5

FIGURE 6.5

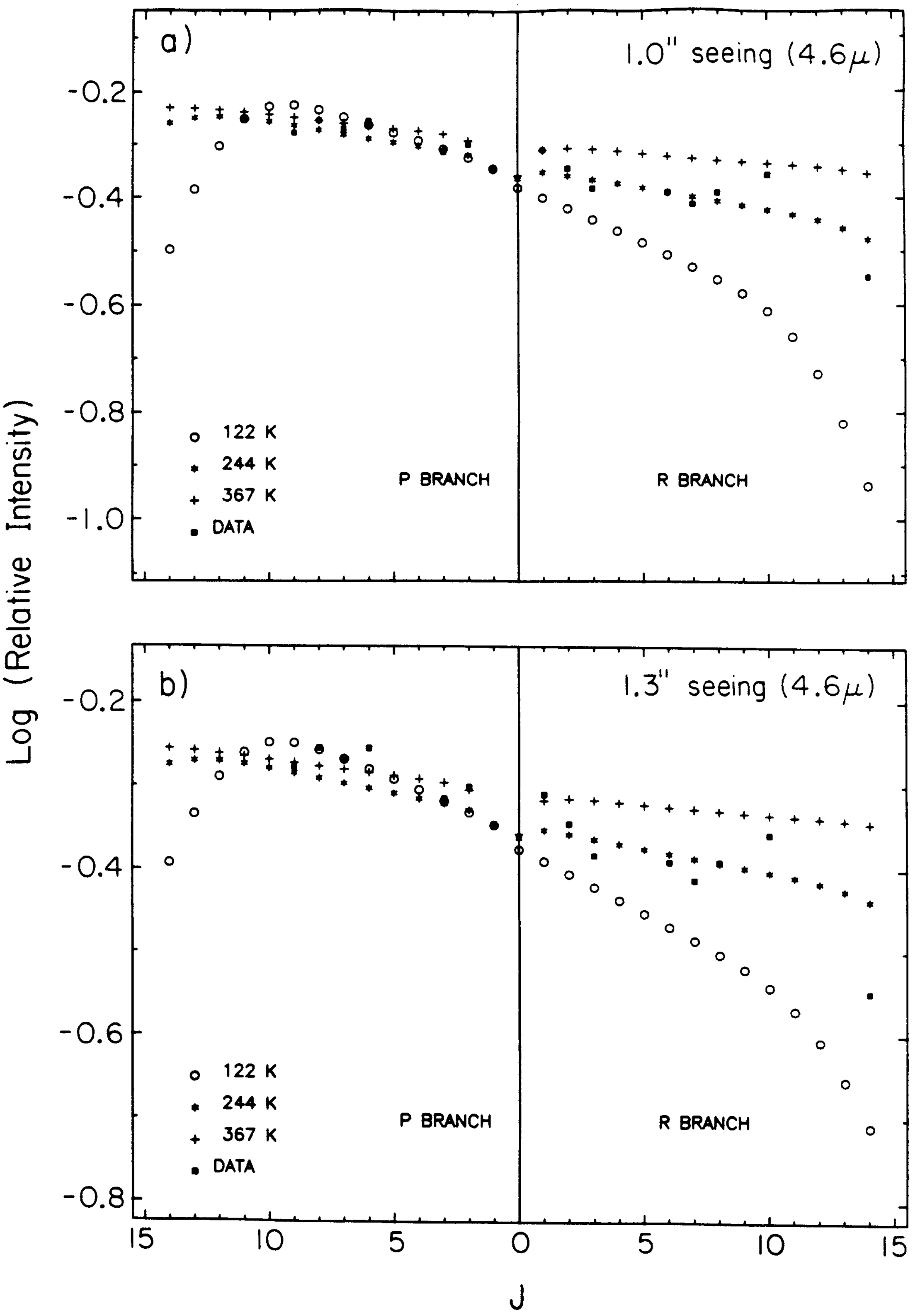

a)
1.0" seeing (4.6μ)
-0.2
-0.4
-0.6
-0.8
-1.0
122 K
244 K
367 K
DATA
P BRANCH
R BRANCH
b)
1.3" seeing (4.6μ)
-0.2
-0.4
-0.6
-0.8
122 K
244 K
367 K
DATA
P BRANCH
R BRANCH
Log (Relative Intensity)
15
10
5
0
5
10
15
J

FIGURE 6.6

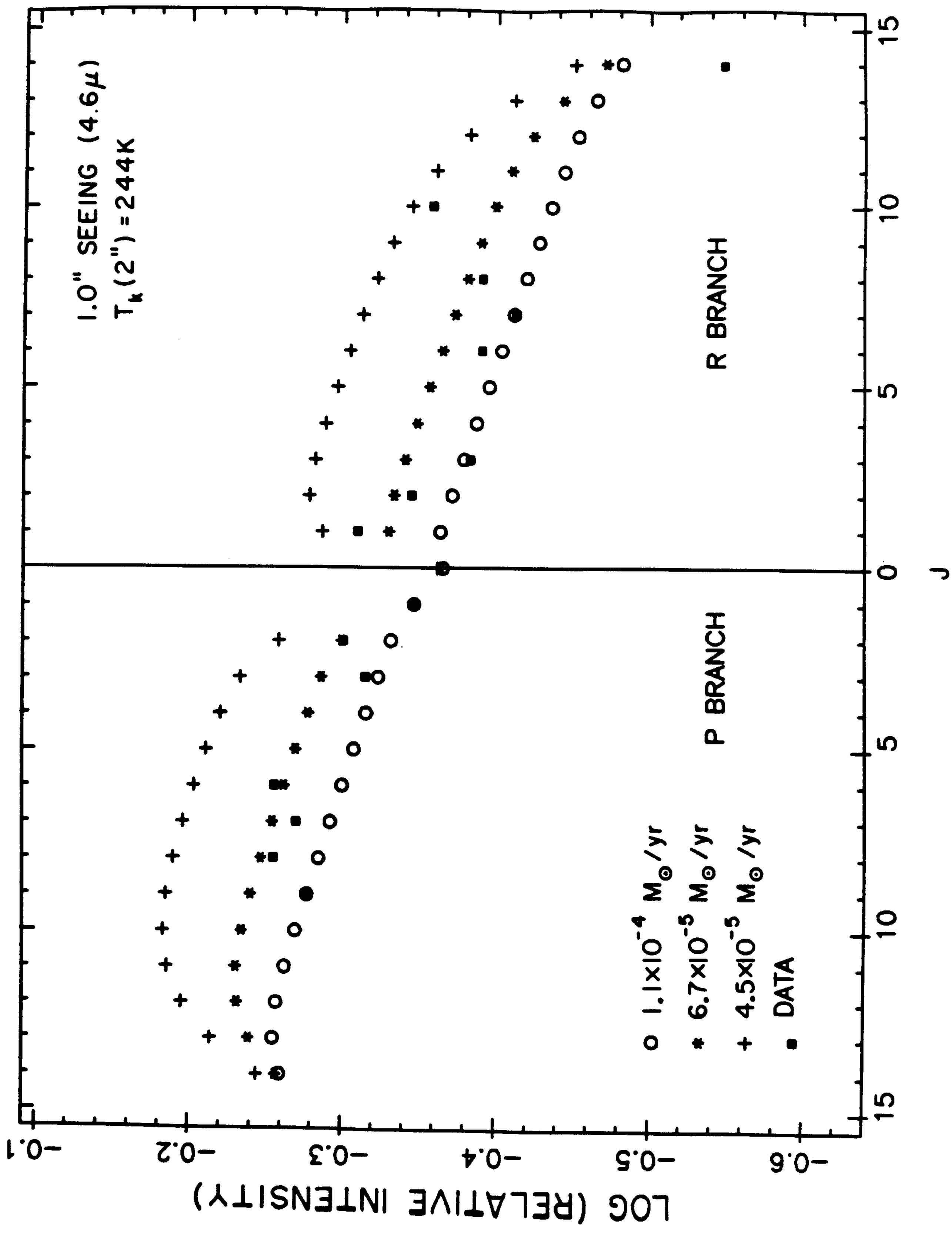
1.0" SEEING (4.6μ)
T_k(2") = 244K
P BRANCH
R BRANCH
○ 1.1×10^-4 M⊙/yr
✱ 6.7×10^-5 M⊙/yr
+ 4.5×10^-5 M⊙/yr
■ DATA
LOG (RELATIVE INTENSITY)
-0.1
-0.2
-0.3
-0.4
-0.5
-0.6
J
15
10
5
0
5
10
15

FIGURE 6.7

BIBLIOGRAPHY

Atkins, R. M., and Timms, P. C. 1977, Spectrochim. Acta., 33A, 853.

Bernat, A. P. 1981, Ap. J., 246, 184.

Bernat, A. P. 1977, Ap. J., 213, 756.

Boyd, R. W. 1978, J. Opt. Soc. Am., 68, 877.

Castor, J. I. 1970, M. N. R. A. S., 149, 111.

Clegg, R. E. S., van IJzendoorn, L. J., and Allamandola, L. J. 1983, M.N.R.A.S., 203, 125.

Deutsch, A. J. 1956, Ap. J. 123, 210.

Dickinson, D. F., and Rodriguez-Kuiper, E. 1981, Ap. J., 247, 112.

Dinerstein, H. L. 1982, in I.A.U. Symposium No. 103, Planetary Nebulae, ed. D. R. Flower (Dordrecht: Reidel), p. 79.

Donn, B., Wickramasinghe, N. C., Hudson, J. P., and Stecher, T. P. 1968, Ap. J., 153, 451.

Elitzur, M., Goldreich, P., and Scoville, N. 1976, Ap. J. 205, 384.

Erickson, N. R. 1981, IEEE Trans. Microwave Theory Tech., 29, 557.

Gehrz, R. D., and Woolf, N. J. 1971, Ap. J., 165, 285.

Gilman, R. L. 1969, Ap. J. (Letters), 155, L185.

Goldreich, P., and Kwan, J. 1974, Ap. J., 190, 27.

Goldreich, P., and Scoville, N. 1976, Ap. J., 205, 144.

Grasshoff, M., Tiemann, E., and Henkel, C. 1981, Astr. Ap., 101, 238.

Green, S., and Chapman, S. 1978, Ap. J. Suppl., 37, 169.

Green, S., and Thaddeus, P. 1976, Ap. J., 205, 766.

Hagen, W. 1978, Ap. J. Suppl., 38, 1.

Hall, D. N. B., Ridgway, S., Bell, E. A., Yarborough, J. M., 1979, SPIE

Vol. 172, Instrumentation in Astronomy III, pp. 121-129.

Harrington, J. P., and Marionni, P. A. 1981, in The Universe at Ultraviolet Wavelengths, ed. R. D. Chapman, Nasa Conf. Publ., NASA CP2171, p. 263.

Harris. S. M., Gottscho, R. A., Field. R. W. and Barrow. R. F. 1982, J. Molec. Spectrosc. 91, 35.

Henkel, C., Matthews, H., and Morris, M. 1983, Ap. J., 267, 184 (HMM).

Herbig, G. H., and Zappala, R. R. 1970, Ap. J., 209, 509.

Hinkle, H. H. 1984, private communication.

Hinkle, H. H. 1978, Ap. J., 220, 210.

Hinkle, H. H. and Barnes. T. G. 1979, Ap. J., 227, 923.

Huber, K. P., and Herzberg, G. 1979, in Molecular Spectra and Molecular Structure, Vol. 4, Constants of Diatomic Molecules (New York: Van Nostrand Reinhold), pp. 608-609.

Huggins, P. J., and Glassgold, A. E. 1982, Ap. J., 252, 201.

Huggins, P. J., Glassgold, A. E., and Morris, M., 1984, Ap. J., (submitted).

Johansson, L. E. B., Andersson, C., Ellder, J., Friberg, P., Hjalmarson, Å., Hoglund, B., Irvine, W. M., Olofsson, H., and Rydbeck, G. 1983, preprint.

Jura, M. 1983, Ap. J., 275, 683.

Keady, J. J., 1982, Ph. D. thesis.

Keady, J. J., Hall, D. N. B., and Ridgway, S. T. 1984, Ap. J. (submitted).

Knapp, G. R. 1983, in IAU Colloquium 76, The Nearby Stars and the Stellar Luminosity Function, ed. A. G. Davis Philip and Arthur R.

Upgren (Schenectady, New York: L. Davis press), p. 113.

Knapp, G. R., and Morris, M. 1984, Ap. J., submitted.

Knapp, G. R., Phillips, T. G., Leighton, R. B., Lo, K. Y., Wannier, P. G., Wootten, H. A., and Huggins, P. J. 1982, Ap. J., 252, 616.

Kuiper, T. B. H., Knapp, G. R., Knapp, S. L., and Brown, R. L. 1976, Ap. J., 204, 408.

Kutner, M. L., and Ulich, B. L. 1981, Ap. J., 250, 341.

Kwan, J., and Hill, F. 1977, Ap. J., 215, 781.

Kwan, J., and Linke, R. 1982, Ap. J., 254, 587.

Kwok, S. 1980, J. Roy. Astron. Soc. Can. 74, 216.

Kwok, S., Bell, M. B., and Feldman, P. A. 1980, Ap. J., 247, 125.

Lafont, S., Lucas, R., and Omont, A., 1982, Astr. Ap., 106, 201.

Lambert, D. L., and Clegg, R. E. S. 1980, M.N.R.A.S., 191, 367.

Lattimer, J. M., and Grossman, L. 1978, The Moon and the Planets, 19, 169.

Lucy, L. B. 1971, Ap. J., 163, 95.

Masson, C. R. 1980, Proc. Soc. Photo-Opt. Instrum. Eng., 231, 291.

McCabe, E. M, Smith, R. C., and Clegg, R. E. S. 1979, Nature, 281, 263.

McCarthy, D. W., and Low, F. J. 1975, Ap. J. (Letters), 202, L37.

McCarthy, D. W., Howell, R., and Low, F. J. 1980, Ap. J. (Letters), 235, L27.

Merrill, M. K. 1983, private communication.

Mitchell, R. M., and Robinson, G. 1980, M.N.R.A.S., 190, 669.

Morris, M. 1975, Ap. J., 197, 603.

Morris, M. 1980, Ap. J., 236, 823.

Morris, M., and Alcock, C. A. 1977, Ap. J., 218, 687.

Morris, M., Gilmore, W., Palmer, P., Turner, B. E., and Zuckerman, B. 1975, Ap. J. (Letters), 199, L47.

Nguyen-Q-Rieu, Bujarrabal, V., Olofsson, H., Johansson, L. E. B., and Turner, B. E. 1984, Ap. J., to be published.

Oloffson, H. 1984, Poster Paper presented at the UCLA Meeting on "Mass Loss From Red Giants" held June 20 and 21, 1984.

Olofsson, H., Johansson, L.E.B., Hjalmarson, A., and Nguyen-Quang-Rieu 1982, Astr. Ap., 107, 128.

Osterbrock, D. E. 1974, Astrophysics of Gaseous Nebulae, W. H. Freeman and Co., San Francisco, p. 228.

Palmer, K. F., Mickelson, M. E., and Rao, K. N. 1972, J. Molec. Spectrosc., 44, 131.

Phillips, T. G., Woody, D. P., Dolan, T. J., Miller, R. E., and Linke, R. A. 1981, IEEE Trans. Magnetics, 17, 684.

Prasad, S. S., and Huntress, W. T., Jr., 1980, Ap. J. Suppl., 43, 1.

Ridgway, S. T., 1984, private communication.

Ridgway, S. T., Carbon, D. F., and Hall, D. N. B. 1978, Ap. J., 225, 138.

Sahai, R., and Claussen, M. J. 1984, in preparation.

Sahai, R., 1984, in preparation.

Scalo, J. M., and Slavsky, D. B. 1980, Ap. J. (Letters), 239, L73.

Sobolev, V. V. 1958, Theoretical Astrophysics, ed. V. A. Ambartsumyan, Pergamon Press ltd., London, Chapter 29.

Sobolev, V. V. 1960, Moving Envelopes of Stars, Harvard University Press.

Timms, P. C. 1982, private communication.

Toombs, R. I., Becklin, E. E., Frogel, J. A., Low, S. K., Porter, F. C., and Westphal, J. A. 1972, Ap. J. (Letters), 173, L71.

Treffers, R. and Cohen, M. 1974, Ap. J., 188, 545.

Tsuji, T. 1973, Astr. Ap., 23, 411.

Tsuji, T. 1964, Ann. Tokyo Astron. Obs., 2nd ser., 9, 1.

Turner, B. E., Zuckerman, B., Palmer, P. and Morris, M. 1973, Ap. J., 186, 123.

van Dishoeck, E. F., and Black, J. H. 1982, Ap. J., 258, 533.

Wannier, P. G., Leighton, R. B., Knapp, G. R., Redman, R. O., Phillips, T. G., and Huggins, P. J. 1979, Ap. J., 230, 149.

Wannier, P. G., and Linke, R. A. 1978, Ap. J., 225, 130.

Witteborn, F. C., Strecker, D. W., Erickson, E. F., Smith, S. M., Goebel, J. H., and Taylor, B. J. 1980, Ap. J., 238, 577.

Woolf, N. J. 1982, Ann. Rev. Astron. Astrophys., 20, 367.

Woolf, N. J. 1973, in Interstellar Dust and Related Topics, I.A.U. Symposium No. 52, ed. J. M. Greenberg and H. C. Van de Hulst, (Dordrecht: Reidel), p. 485.

Woolf, N. J., and Ney, E. P. 1969, Ap. J. (Letters), 155, L181.

Wootten, A. 1983, unpublished data.

Wootten, A., Lichten, S. M., Sahai, R., and Wannier, P. G. 1982, Ap. J., 257, 151.

Yin, P. K. L., and Rao, N. 1972, J. Molec. Spectrosc., 42, 385.